Epitaxial thin film growth and properties of unconventional oxide superconductors: cuprates and cobaltates

vom Fachbereich
Material- und Geowissenschaften
der Technischen Universität Darmstadt

genehmigte
Dissertation

zur Erlangung des akademischen Grades
eines Doktors der Naturwissenschaften (Dr. rer. nat.)

von
Dipl. Phys. Yoshiharu Krockenberger
aus Stuttgart

Darmstadt 2006

D17

Referent: Prof. Dr. L. Alff
Korreferent: Prof. Dr. H. Fuess
Korreferent: Prof. Dr. H.-U. Habermeier

Tag der Einreichung: 19. Oktober 2006
Tag der Disputation: 05. Dezember 2006

The only consensus is, that there is absolutely no consensus on the theory of high-T_c cuprates.
P.W. Anderson

Contents

Acknowledgements

I owe much gratitude towards my supervisor Prof. Dr. Lambert Alff. His copious ken avail myself of tremendously. He found time with me for discussions on large scale even on busy schedules. It is his meritoriousness giving me the chance collecting experience at NTT Basic Research Laboratories (Japan), Max Planck Institute for solid state research (Germany) and Paul Scherrer Institute (Switzerland). His cooperativeness providing any help I need was indefatigable.
At NTT Basic Research Laboratories, Prof. Dr. Michio Naito aroused my interest on being belligerent on facing obnoxious conditions. It is my great pleasure to unduly acknowledge him.
In great extend I am indebted to Prof. Hanns-Ulrich Habermeier. For his flexibility and understanding I am forever indebted. I also would like to thank Prof. Bernhard Keimer for his valuable advise and constant encouragement during the course of my research work. Moreover, I am also thankful for the funding in Max Planck Institute for solid state research. I am also grateful to Prof. Christian Bernhard introducing me to the advantages of far infrared ellipsometry. His keenness for optical investigations was enlightening for me. I also convey my thankfulness to Prof. Peter Lemmens for prolific discussions in the field of Raman spectroscopy. Dr. Dirk Manske became a real companion through all ups and downs during the preparation of my thesis. Hence, he enabled me to participate from his pre-eminent knowledge. My full thankfulness is conveyed to him. I am also thankful to Dr. Alexander Boris for his helpful assistance and fruitful advice in optical problems.
I would like to extend my deep gratitude to Dr. Hideki Yamamoto, Dr. Shin-ichi Karimoto, Dr. Akio Tsukada, Dr. Hiroyuki Shibata, Dr. Kenji

Ueda and Dr. Jose Kurian whom I met again at Darmstadt University of Technology.
The world of double perovskite chemistry became accessible by the stunning succor of Prof. Martin Jansen. For this valuable support I express my thankfulness to him. Moreover, I am thankful to Dr. Kailash Mogare for his sedulous fortification in synthesizing compounds.
Neutron scattering would have been never triumphant devoid of the meticulous elaborations of Dr. Manfred Reehuis and I would like to convey my thankfulness to him. I would like to acknowledge Dr. Clemens Ulrich for spending plethora of his valuable hours for prolific discussions on solid state physics.
My acknowledgement is extended to Georg Christiani and Petar Yordanov for their friendship and feisty endorsement.
I would like to thank Prof. Hans-Henning Klauss from the TU Braunschweig for introducing me to the world of low energy muons and making me realize the power of this probing tool in understanding the fundamental underlying physics. I take this opportunity to extend my gratitude to Dr. Hubertus Luetkens and Dr. Andreas Suter from the Paul Scherrer Institute (Switzerland).
It is with great pleasure I thank my colleagues Andreas Winkler, Dr. Philipp Komissinskij, Jürgen Schreek, Dr. Soltan Soltan, Stephan Schmid, Benjamin Stuhlhofer, Ingo Fritsch and Gülgün Aydogdu-Kuru. I also acknowledge the help of Dr. Mitsuharu Konuma, Heinrich Klann, Gabi Götz and Eva Brücher.
I would like to thank Marion Bracke and Claudia Hagemann for sorting out administrative intricatenesses.
I express my deep sense of gratitude for the financial support from the Max Planck Society.
Thankfulness with mellowness is conveyed to Sabine Lacher. Her abilities in synthesizing not only crystals but also Octopus dishes are unbeatable. In addition, the chocolate corner in Max Planck Institute was her invention where I could never overcome these temptations.
My thankfulness is also with Prof. Hans-Joachim Queisser for valuable information on connections to Japan.
Above all, I thank the Almighty God for his Grace and Blessings.

Yoshiharu Krockenberger

1

Introduction

Unconventional superconductors are still among the most fascinating materials in modern solid state physics and materials science. While high-temperature superconductors [1] are at the brink of entering the huge market of wires, tapes, and cables, the mechanism of high-temperature superconductivity still has not been fully understood. Recently, also new unconventional superconductors based on transition metal oxides have been found with outstanding novel properties: Sr_2RuO_4, an iso-structural material to the high-temperature cuprates, is the first solid state equivalent to superfluid ^{3}He [2]. Another novel superconductor is $Na_xCoO_2 \cdot yH_2O$ [3], a material in which the Co ions sit on a triangular CoO_2-lattice forming a frustrated antiferromagnetic ground-state. In this material an even more exotic superconducting state as compared to the cuprate or ruthenate superconductors might be realized [4]. Applications of such superconductors are for example discussed in the field of quantum computation.

The discovery of high-temperature superconductors has strongly driven the development of suited thin film fabrication methods of complex oxides. One way is the adaptation of molecular beam epitaxy (MBE) for the growth of oxide materials. Another approach is the use of pulsed laser deposition (PLD) which has the advantage of good stoichiometry transfer from target to the substrate. Both techniques are used within this thesis. Epitaxial thin films of new materials are of course needed for future applications. In addition, the controlled synthesis of thin film matter which can be formed far away from thermal equilibrium allows for the investigation of fundamental physical materials properties.

This thesis focusses on two types of novel oxides superconductors. The first

superconducting material belongs to the group of cuprates high-temperature superconductors. While the by far biggest part of research in this field is done on hole doped cuprates, here, electron doped high-temperature superconductors are investigated. These materials are of high interest, as the comparison of hole and electron doping in cuprates is expected to give clues for the mechanism of high-temperature superconductivity. In particular, the influence of different rare earth ions on the superconducting properties are examined which in the end leads to a new phase diagram of electron doped cuprates. Another important topic is the search for a cuprate material in which electron and hole doping is possible without changing other degrees of freedom. Such an approach has been undertaken in this thesis to obtain such novel materials.

After the discovery of superconductivity in $Na_xCoO_2 \cdot yH_2O$, a lot of research efforts have been initiated in this field. These efforts were hampered by the fact that it is difficult to obtain phase pure bulk material and clean surfaces. Using epitaxial thin films, these problems can be overcome. Within this thesis (to the best of my knowledge) the first fabrication of epitaxial Na_xCoO_2 thin films, and also superconducting $Na_xCoO_2 \cdot yH_2O$ thin films are reported. While the superconducting material is difficult to handle in real applications, dry Na_xCoO_2 is of high interest for thermoelectricity.

This thesis is organized in two parts, one dealing with the electron doped cuprates superconductors, the second with superconducting sodium cobaltate. After this short introduction, **Part I** of the thesis starts with a brief survey on superconductivity and in particular on high-temperature superconductivity in **Chapter 2**. In **Chapter 3**, the thin film growth of electron doped cuprates is described in detail. Due to the importance of the reduction process, which is essential to electron doped cuprates, this topic has its own chapter (**Chapter 4**). In **Chapter 5** the properties of the epitaxial thin films are described and discussed in detail with particular emphasis on low energy muon spectroscopy, probably the only tool allowing the determination of magnetic phases in thin films. **Chapter 6** presents a new method to synthesize undoped La based electron doped cuprates which have not been fabricated successfully so far. These materials are highly important with respect to the comparison of hole and electron doped cuprates.

In **Part II** the synthesis of superconducting sodium cobaltates are described. This part starts with a short general introduction into this bronze given in **Chapter 7**. **Chapter 8** comprises a very short introduction into pulsed

laser deposition and in more detail the application of this thin film fabrication method for Na_xCoO_2 and $Na_xCoO_2 \cdot yH_2O$. In **Chapter 9** the electronic, magnetic, and superconducting properties of the synthesized epitaxial thin films are presented.
In the concluding **Chapter 10**, a short summary with an outlook on the ongoing research in epitaxial thin films of unconventional superconductors is given.

学位論文の概要

従来とは異なる（これまでのＢＣＳ理論では説明の難しい）超伝導体は現代の固体物理や材料科学の分野で依然として魅惑的な材料である。高温超伝導体は、今、当に、線材やテープの巨大な経済市場に参入しようという間際にあるにもかかわらず、高温超伝導の機構は依然として真には解明されていない。近年、遷移金属酸化物をベースにした新しい従来とは異なる超伝導体が再び見出された。この物質、Sr_2RuO_4は、高超伝導臨界温度銅酸化物と同じ結晶構造を示し、初めて見出された超流動^{3}Heと固体等価な物質であるという顕著な新しい特性を有する。もう一つの新しい超伝導体は$Na_xCoO_2 \cdot yH_2O$で、この物質中では、Coイオンが減衰反強磁性基底状態を形作るCoO_2でできた三角形の上に位置している。この材料を使えば、更にエキゾティックな超伝導体や銅酸化物、ルテニウム酸化物との比較が可能となろう。このような超伝導体の応用は量子素子の分野で議論の対象となっている。
高温超伝導体の発見は、このような複雑な系の酸化物に適した薄膜生成法の開発を促進してきた。その一つは、分子線エピタキシー（MBE）を酸化物材料の成長に合わせて改良することである。パルスレーザー堆積法（PLD）を応用するのは、もう一つのアプローチである。PLDはターゲットの化学組成（ストイキオメトリー）がほぼそのまま基盤の上に転写される利点を持っている。本論文ではこの両技術が使われている。将来の超伝導応用には新しい物質のエピタキシー薄膜が必要になろう。更には、熱平衡から大きく離れた状態で形成されうる薄膜物質の良く制御された合成手法の開発は、物質の基礎的な物理的性質の観察を可能にするであろう。

この論文は新しい二つの型の酸化物超伝導体に焦点を置いている。一つ目の超伝導体は銅酸化物高温超伝導体のグループに属する。この分野の大多数の研究は正孔(ホール)ドープ銅酸化物についてなされているが、この学位論文では、電子ドープ高温超伝導体を調べている。この物質は、正孔ドープと比較の上で非常に興味があり、銅酸化物における電子ドープは高温超伝導の機構の解明の糸口を与えるものと期待されている。特に、様々な希土類イオンの超伝導性に及ぼす影響が明らかになれば、最終的には電子ドープ銅酸化物の新しい相図を作ることができるであろう。更に重要なトピックスは、他の自由度、例えば結晶構造、を変えずに電子ドープと正孔ドープが可能な銅酸化物物質を見つけることである。この博士論文では、そのような新しい物質を得る道筋が述べられている。

$Na_xCoO_2 \cdot yH_2O$の超伝導性が発見された後、この分野では沢山の研究が始まった。しかし、純粋な単一相の結晶や清浄な表面の得難いことが研究を推進する上で大きな妨げになっている。エピタキシー薄膜を使うことでこの問題は解決されうる。本論文中では、エピタキシャル成長したNa_xCoO_2薄膜が(自分が知る限りでは)始

めて作成され、また超伝導を示す $Na_xCoO_2 \cdot yH_2O$ 薄膜が報告されている。この超伝導物質は実際の応用では取り扱いが難しいが、ドライ(結晶水を含まない) Na_xCoO_2 は熱電能からも非常に興味のある材料である。

この論文は二つの部分から構成されている。一つ目は電子ドープ銅酸化物超伝導体で二つ目にはナトリウムの超伝導コバルト酸化物を取り扱う。この物質についての短い紹介の後、論文の**第１部**はまず超伝導の概説から始まり、特に**第２章**では高温超伝導について記述する。**第３章**では電子ドープ銅酸化物の薄膜作成について詳しく述べる。電子ドープ銅酸化物では、この物質に固有の化学還元課程が重要なので、このテーマは特に別の１章**第４章**を費やした。**第５章**では、エピタキシャル成長した薄膜の性質が記述されて議論されている。特に重点を置いたのは低エネルギーミュー中間子分光法で、これは多分、薄膜の磁性相を決定できる唯一の手法であろう。**第６章**では、これまで作成に成功したことのない無添加 La ベース電子ドープ銅酸化物の新しい合成法を示す。これらの物質は正孔ドープあるいは電子ドープされた銅酸化物を比較する上で高い重要性を有する。

第２部においては、ナトリウムの超伝導コバルト酸化物について述べる。この第２部はブロンズの短い一般的な緒言について述べた**第７章**に始まる。**第８章**は、パルスレーザー堆積法の非常に簡単な紹介と Na_xCoO_2 や $Na_xCoO_2 \cdot yH_2O$ 薄膜生成への適用についての詳細な記述から構成されている。**第９章**では、作成されたエピタキシャル薄膜の電子的、磁気的性質及び超伝導性が述べられている。最後の**第１０章**ではこの学位論文の短い要旨と従来とは異なる超伝導体のエピタキシャル薄膜に関する現在の研究についてその概略が与えられている。

Part I

ELECTRON DOPED CUPRATE SUPERCONDUCTORS

2

Cuprates - Superconductivity on square CuO_2-planes

2.1 Superconducting cuprates

Superconductivity is an exceptional phenomenon in which at a certain temperature metals can enter a state that conducts electricity with absolutely zero resistance and carries infinitely persistent electrical currents. Superconductivity results not just from the suppression of single particle scattering effects, but instead is a macroscopic manifestation of phase coherent quantum mechanics, as evidenced by the Meissner effect, i.e., the complete expulsion of magnetic field from a superconductor's interior. The effect was first discovered in mercury by H.K. Onnes's group shortly after their successful liquefaction of helium in 1911 [5]. Although phenomenological models of superfluidity and superconductivity were advanced by London, Landau and others [6, 7], a complete description of the phenomenon had to wait until the seminal achievement of Bardeen, Cooper, and Schrieffer with their BCS model [8]. They proposed that a phonon mediated electron-electron interaction caused normally repulsive electrons with opposite momenta to attract each other, such that they formed a bound state called Cooper-pairs. This bound $\vec{k} = 0$ state is a boson and many such bosons, acting in concert in a single $\vec{k} = 0$ state, can exhibit macroscopic quantum phenomena. Bardeen, Cooper, and Schrieffer were able to demonstrate how such a state supports persistent currents, the origin of the Meissner effect, and that the effect has an onset at a well defined critical transition temperature (T_c). Since the discovery of superconductivity in mercury, tremendous efforts have been carried

out in the search for new superconductors and also material with higher T_c and this endeavor is still ongoing. Following the discovery of superconductivity, many elemental materials have been shown to be superconducting. In fact, approximately half the elements in the periodic table are known superconductors; some of them are only superconducting at ultra-low temperatures and/or exceedingly high pressures. The maximum elemental T_c at ambient pressure is 9.25 K in niobium. Compounds based on superconducting elements showed greater promise for raising T_c and advances were made that pushed up transition temperatures by a factor of 2. Although the BCS theory remained (and remains) a poor predictor of transition temperatures or even the existence of superconductivity [9], various empirical rules were set up by materials scientists. Famous Bernd Matthias elucidated the now so-called Matthias rules

1. High-symmetry crystals are best
2. High near-E_F density of states is favorable.
3. Stay away from oxygen.
4. Stay away from magnetism.
5. Stay away from insulators.
6. Stay away from theorists. - This addendum to the original 5 is blamed on S. Girvin [10]. It wasn't one of Matthias's original rules, but it is good advice and not just in making superconductors!

The above proved to be an excellent guide for almost 75 years of superconductivity research, with maximum T_c's steadily rising in a series of niobium based intermetallics culminating in the discovery of 23 K superconductivity in Nb_3Ge in 1976. Theoretically, a weak coupling analysis of the BCS equation by Cohen and Anderson [11] argued that the maximum T_c was constrained within an electron-phonon mechanism by competing effects and that very high electron-phonon coupling typically leads to structural transitions that kill superconductivity. Specifically they argued starting from an equation of the form

$$T_c = \frac{\omega_0}{1.45}\left[\frac{-1.04(1+\lambda)}{\lambda - \mu^\star(1+0.62\lambda)}\right], \tag{2.1}$$

where ω_0 is the Debye energy, λ the effective electron-phonon coupling constant and $\mu^\star$ an effective pseudo-potential. Naively, one would believe that

increasing ω_0 would lead to higher T_c's, however increases made here are compensated by effects elsewhere. A simple relation for the effective pseudopotential $\mu^\star = \mu/[1+\mu\ln(E_F/\omega_0)]$, where μ is the chemical potential, gives that the effects of ionic screening enter in Eq. 2.1 and becomes less effective as the Debye lattice vibration frequency scale increases. For similar reasons the effective electron-phonon coupling parameter $\lambda = \kappa/(M_{ionic}\omega_0)$, where κ is the isotope exponent, decreases as ω_0 increases where M_{ionic} is the ionic mass. One could increase κ, but this is a parameter governed by such particularities as Fermi surface shape and large κ values (due to nesting effects for instance) typically lead to structural instabilities. Cohen and Anderson, argued that for these reasons, T_c's were limited to $\sim 10\,\mathrm{K}$. Although their was only a weak coupling analysis these rough considerations seem borne out by the experimental fact that many materials had been found within a factor of 2 of 10 K, but none much higher.

All this changed in 1986. Bednorz and Müller violated almost all Matthias rules when they were looking for superconductivity in a class of cuprate perovskites with a structural transition in which the CuO_6 octahedra vertically distort (Jahn-Teller distortion). Since this phase transition was driven by a large electron-phonon coupling, it was hoped that these insulators, made metallic by doping, could become superconductors. They discovered 30 K superconductivity in $La_{2-x}Ba_xCuO_4$ [1]. This sparked a flurry of activity, and superconducting T_c's of 90 K or higher soon followed, by Chu and others [12]. Even two decades after the discovery of superconductivity in this material class, still a general understanding of the underlying mechanisms has not been reached yet. Despite being one of the most deeply and widely explored issues in physics of all times, a coherent understanding in the scientific community is still elusive. It is considered by most that the anomalous properties of the metallic normal state and the close proximity to an antiferromagnetic phase hold the key to the high transition temperatures. The more that is learned about these materials in both their normal and superconducting states, the more complex and interesting they have been revealed to be.

2.2 Superconductivity

The phenomena of superconductivity supplies several consequences, that can be utilized in proofing itself. Here, the consequences, as there are perfect dia-

magnetism, penetration depth and coherence lengths and the appearance of a superconducting gap, will be briefly discussed.
In the superconducting state, perfect conduction is not a convenient approximation, it is a real, experimentally verifiable fact. Since all materials have defects and phonons (and to a lesser degree of importance, electron-electron interactions), there is no such ideal thing with zero resistivity ($\rho = 0$). As a result, from basic understanding of metallic conduction ρ must be finite, even at $T = 0\,\mathrm{K}$. However, superconductors show $\rho = 0$. The first superconductor (Hg) was discovered by Onnes in 1911. It becomes superconducting for $T < 4.2\,\mathrm{K}$. Clearly this superconducting state must be fundamentally different from the "normal" metallic state. The superconducting state must be a different phase, separated by a phase transition, from the normal state.

2.2.1 Evidence of a phase transition

Evidence of the phase transition can be seen in the specific heat (see Fig. 2.1). The jump in the superconducting specific heat C_s indicates that there is a phase transition without a latent heat (i.e., the transition is continuous or second order). Furthermore, the activated behavior of C for $T < T_c$

$$C_s \sim e^{-\beta\Delta} \tag{2.2}$$

gives us a clue to the nature of the superconducting state. It is as if excitations require a minimum energy Δ.

2.2.2 Meissner-Ochsenfeld effect

There is another, much more fundamental characteristic which distinguishes the superconductor from a normal, but ideal, conductor. The superconductor expels magnetic flux, i.e., $B = 0$ within the bulk of a superconductor. This is fundamentally different from an ideal conductor, for which $\dot{B} = 0$ since for any closed path

$$0 = I \cdot R = V = \oint \mathcal{E} \cdot dl = \int_S \nabla \times \mathcal{E} \cdot dS = -\frac{1}{c} \int_S \frac{\partial B}{\partial t} \cdot S \tag{2.3}$$

or, since S and C are arbitrary

$$0 = -\frac{1}{c}\dot{B} \cdot S \Rightarrow \dot{B} = 0 \tag{2.4}$$

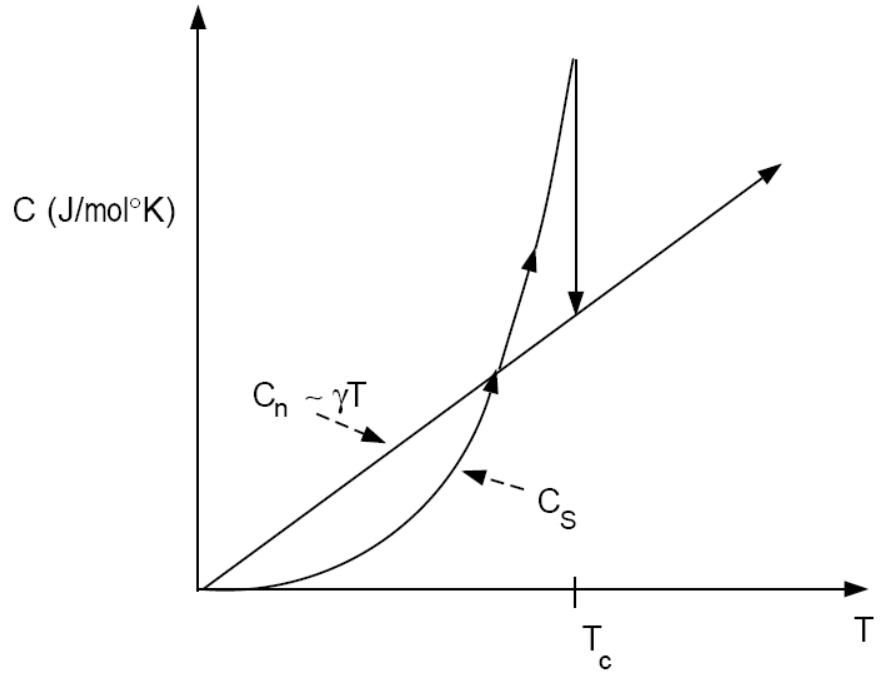

Fig. 2.1: The specific heat of a superconductor C_S and normal metal C_n. Below the transition, the superconductor specific heat shows activated behavior, as if there is a minimum energy for thermal excitations.

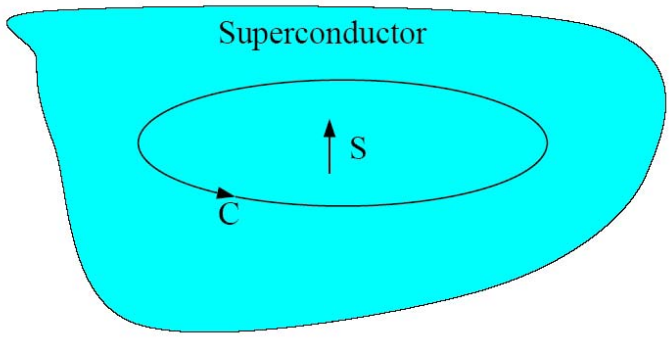

Fig. 2.2: A closed path and the surface it contains within a superconductor.

Thus, for an ideal conductor, it matters if it is field cooled or zero field cooled. Where as for a superconductor, regardless of the external field and its history, if $T < T_c$, then $B = 0$ inside the bulk. This effect, which uniquely distin-

guishes an ideal conductor from a superconductor, is called the Meissner-Ochsenfeld effect. For this reason a superconductor is an ideal diamagnet.

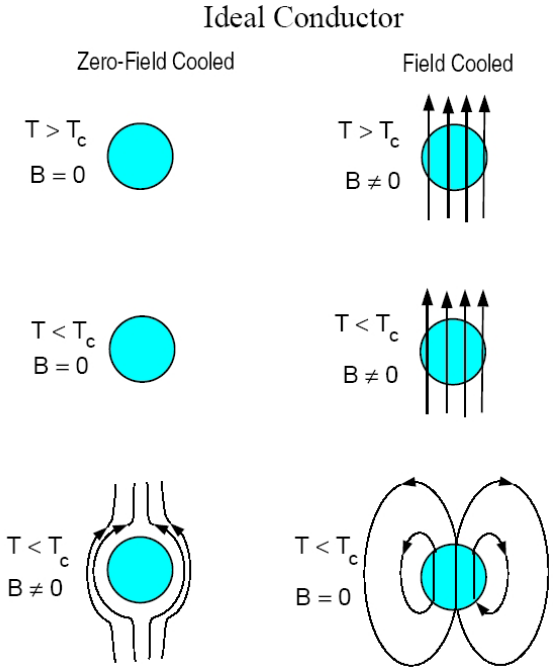

Fig. 2.3: For an ideal conductor, flux penetration in the ground state depends on whether the sample was cooled in a field through the transition.

I.e.

$$\begin{aligned} B = \mu \cdot H = 0 \Rightarrow \mu = 0 \\ M = \chi \cdot H = \tfrac{\mu - 1}{4\pi} H \end{aligned} \tag{2.5}$$

$$\chi_{SC} = -\frac{1}{4\pi} \tag{2.6}$$

The measured χ, Fig. 2.4, in a superconducting material is very large and negative (diamagnetic). This can also be interpreted as the presence of persistent surface currents which maintain a magnetization of

$$M = -\frac{1}{4\pi} H_{ext} \tag{2.7}$$

in the interior of the superconductor in a direction opposite to the applied field. The energy associated with this current increases with H_{ext}. At some point it is then more favorable (ie., a lower free energy is obtained) if the system returns to a normal metallic state and these screening currents abate. Thus there exists an upper critical field H_c.

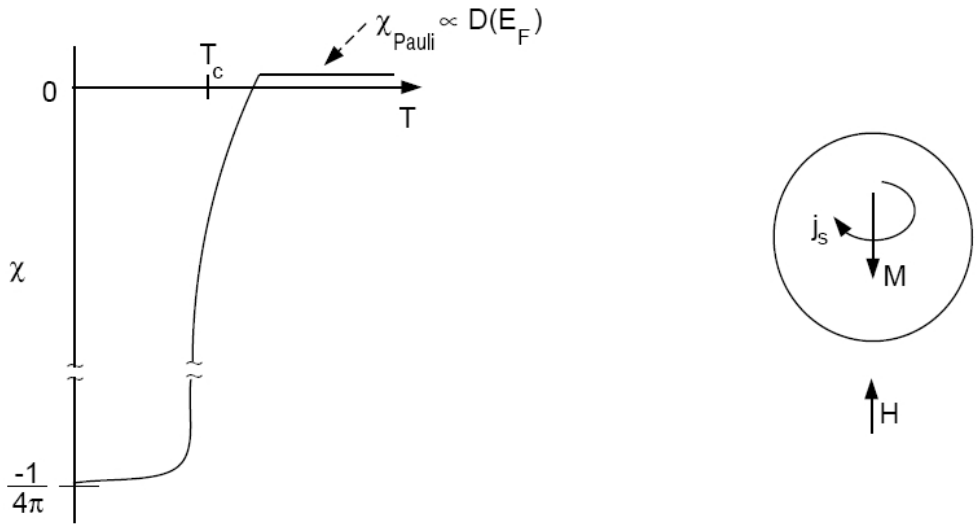

Fig. 2.4: LEFT: A sketch of the magnetic susceptibility versus temperature of a superconductor. RIGHT: Surface currents on a superconductor are induced to expel the external flux. The diamagnetic response of a superconductor is orders of magnitude larger than the Pauli paramagnetic response of the normal metal at $T > T_c$.

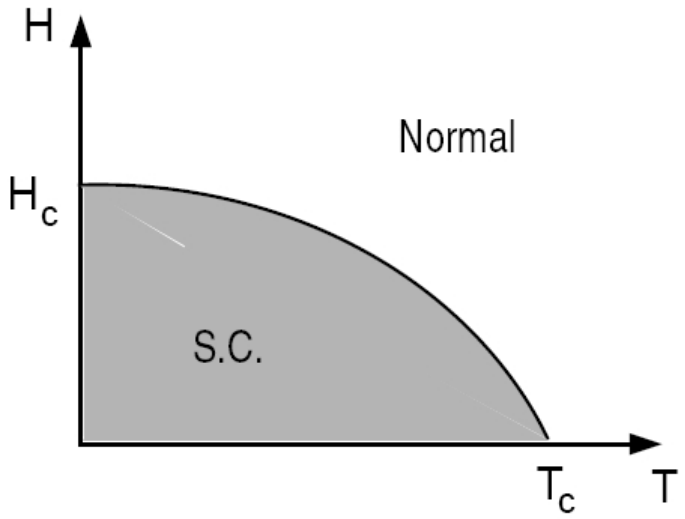

Fig. 2.5: Superconductivity is destroyed by either raising the temperature or by applying a magnetic field.

2.2.3 London Equations

London and London derived a phenomenological theory of superconductivity which correctly describes the Meissner-Ochsenfeld effect. They assumed that

the electrons move in a frictionless state, so that

$$m\dot{v} = -e\mathcal{E} \tag{2.8}$$

or, since $\frac{\partial j}{\partial t} = -e \cdot n_s \cdot \dot{v}$,

$$\frac{\partial j_s}{\partial t} = \frac{e^2 n_s}{m}\mathcal{E} \quad \text{(first LONDON equation)} \tag{2.9}$$

Then, using the Maxwell equation

$$\nabla \times \mathcal{E} = -\frac{1}{c}\frac{\partial B}{\partial t} \Rightarrow \frac{m}{n_s e^2}\nabla \times \frac{\partial j_s}{\partial t} + \frac{1}{c}\frac{\partial B}{\partial t} = 0 \tag{2.10}$$

or

$$\frac{\partial}{\partial t}\left(\frac{m}{n_s e^2}\nabla \times j_s + \frac{1}{c}B\right) = 0 \tag{2.11}$$

This describes the behavior of an ideal conductor (for which $\rho = 0$), but not the Meissner effect. To describe this, the constant of integration must be chosen to be zero. Then

$$\nabla \times j_s = -\frac{n_s e^2}{m \cdot c}B; \quad \text{(second LONDON equation)} \tag{2.12}$$

or defining $\lambda_L = \frac{m}{n_s e^2}$, the London equations become

$$\frac{B}{c} = -\lambda_L \nabla \times j_s; \quad \mathcal{E} = \lambda_L \frac{\partial j_s}{\partial t} \tag{2.13}$$

If we now apply the Maxwell equation $\nabla \times H = \frac{4\pi}{c}j \Rightarrow \nabla \times B = \frac{4\pi}{c}\mu j$ then we get

$$\nabla \times (\nabla \times B) = \frac{4\pi}{c}\mu \nabla \times j = -\frac{4\pi\mu}{c^2\lambda_L}B \tag{2.14}$$

and

$$\nabla \times (\nabla \times j) = -\frac{1}{\lambda_L c}\nabla \times B = -\frac{4\pi\mu}{c^2\lambda_L}j \tag{2.15}$$

or since $\nabla \cdot B = 0$, $\nabla \cdot j = \frac{1}{c}\frac{\partial \rho}{\partial t} = 0$ and $\nabla \times (\nabla \times a) = \nabla(\nabla \cdot a) - \nabla^2 a$ we get

$$\nabla^2 B - \frac{4\pi\mu}{c^2\lambda_L}B = 0; \quad \nabla^2 j - \frac{4\pi\mu}{c^2\lambda_L}j = 0 \tag{2.16}$$

Now consider a superconductor in an external field shown in Fig. 2.6. The field is only in the x-direction, and can vary in space only in the z-direction, then since $\nabla \times B = \frac{4\pi}{c}\mu j$, the current is in the y-direction, so

$$\frac{\partial^2 B_x}{\partial z^2} - \frac{4\pi\mu}{c^2\lambda_L}B_x = 0; \quad \frac{\partial^2 j_{sy}}{\partial z^2} - \frac{4\pi\mu}{c^2\lambda_L}j_{sy} = 0 \tag{2.17}$$

with the solutions

$$B_x = B_x^0 \cdot e^{-\frac{z}{\Lambda_L}}; \quad j_{sy} = j_{sy} \cdot e^{-\frac{z}{\Lambda_L}} \tag{2.18}$$

$\Lambda_L = \sqrt{\frac{c^2\lambda_L}{4\pi\mu}} = \sqrt{\frac{mc^2}{4\pi n e^2 \mu}}$ is the penetration depth.

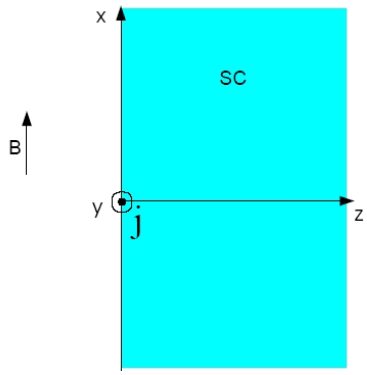

Fig. 2.6: A superconducting slab in an external field. The field penetrates into the slab a distance $\Lambda_L = \sqrt{\frac{mc^2}{4\pi n e^2 \mu}}$.

2.2.4 Cooper pairing

The superconducting state is fundamentally different from any possible normal metallic state (i.e., a perfect metal at $T = 0\,\mathrm{K}$). Thus, the transition from the normal metal state to the superconducting state must be a phase transition. A phase transition is accompanied by an instability of the normal state. Cooper first quantified this instability as due to a small attractive (or repulsive) interaction between two electrons above the Fermi surface.

2.2.5 The retarded pairing potential

The attraction comes from the exchange of phonons[1]. The lattice deforms slowly in the time scale of the electron. It reaches its maximum deformation at a time $\tau \sim \frac{2\pi}{\omega_D} \sim 10^{-13}\,\mathrm{s}$ after the electron has passed. In this time the first electron has traveled $\approx v_F \tau \approx 10^8 \frac{\mathrm{cm}}{\mathrm{s}} \cdot 10^{-13}\,\mathrm{s} \approx 1000\,\text{Å}$. The positive charge of the lattice deformation can then attract another electron without feeling the Coulomb repulsion of the first electron. Due to retardation, the electron-electron Coulomb repulsion may be neglected. The net effect of the phonons is then to create an attractive interaction which tends to pair time-reversed quasiparticle states. They form an antisymmetric spin singlet so that the spatial part of the wave function can be symmetric and nodeless

[1] Note, that this is valid only for special cases of superconducting materials, e. g. pure metals. In the case of high temperature superconductors, other mechanisms cause the instability at the Fermi surface.

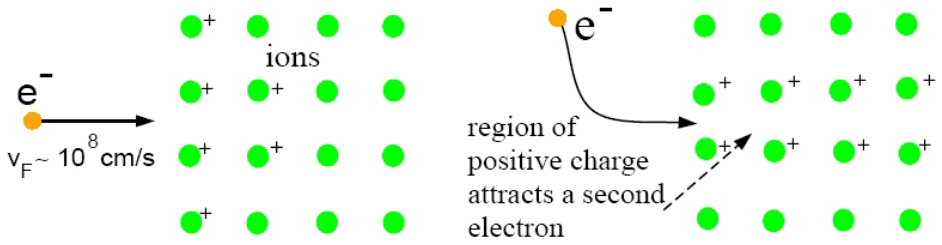

Fig. 2.7: Origin of the retarded attractive potential. Electrons at the Fermi surface travel with a high velocity v_F . As they pass through the lattice (left), the positive ions respond slowly. By the time they have reached their maximum excursion, the first electron is far away, leaving behind a region of positive charge which attracts a second electron.

and so take advantage of the attractive interaction. Furthermore they tend to pair in a zero center of mass (cm) state so that the two electrons can chase each other around the lattice.

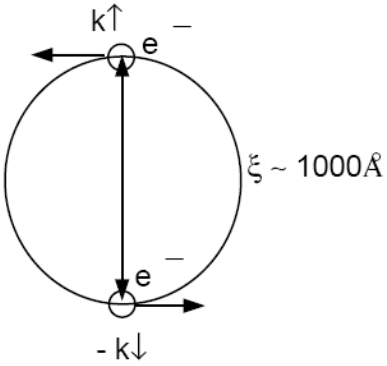

Fig. 2.8: To take full advantage of the attractive potential illustrated in Fig. 2.7, the spatial part of the electronic pair wave function is symmetric and hence nodeless. To obey the Pauli principle, the spin part must then be antisymmetric or a singlet.

2.2.6 Scattering of Cooper Pairs

This latter point may be quantified a bit better by considering two electrons above a filled Fermi sphere. These two electrons are attracted by the exchange of phonons. However, the maximum energy which may be exchanged in this way is $\approx \hbar\omega_D$. Thus the scattering in phase space is restricted to a narrow shell of energy width $\hbar\omega_D$. Furthermore, the momentum in this

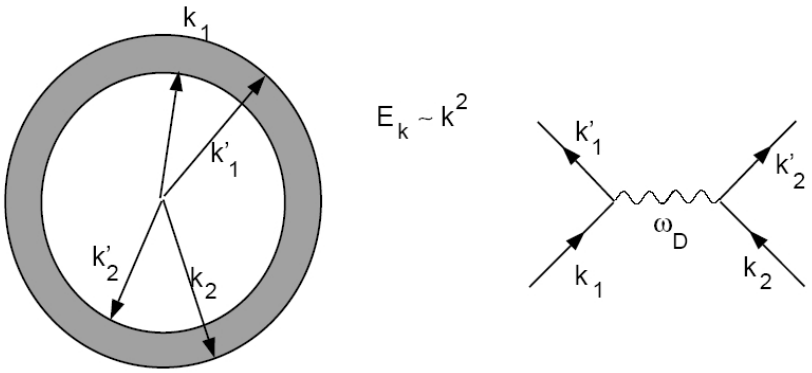

Fig. 2.9: Pair states scattered by the exchange of phonons are restricted to a narrow scattering shell of width $\hbar\omega_D$ around the Fermi surface.

scattering process is also conserved

$$\mathbf{k_1} + \mathbf{k_2} = \mathbf{k'_1} + \mathbf{k'_2} = \mathbf{K} \tag{2.19}$$

Thus the scattering of $\mathbf{k_1}$ and $\mathbf{k_2}$ into $\mathbf{k'_1}$ and $\mathbf{k'_2}$ is restricted to the overlap of the two scattering shells. Clearly this is negligible unless $\mathbf{K} \approx 0$. Thus the interaction is strongest (most likely) if $\mathbf{k_1} = -\mathbf{k_2}$ and $\sigma_1 = -\sigma_2$; i.e., pairing is primarily between time-reversed eigenstates.

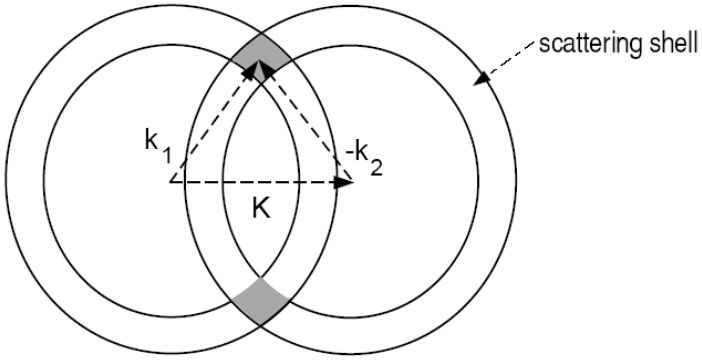

Fig. 2.10: If the pair has a finite center of mass momentum, so that $\mathbf{k_1} + \mathbf{k_2} = \mathbf{K}$, then there are few states which it can scatter into through the exchange of a phonon.

2.2.7 The BCS ground state

In the preceding section, we saw that the weak phonon-mediated attractive interaction was sufficient to destabilize the Fermi sea, and promote the formation of a Cooper pair $(\mathbf{k}\uparrow, -\mathbf{k}\downarrow)$. The scattering

$$(\mathbf{k}\uparrow, -\mathbf{k}\downarrow) \longrightarrow (\mathbf{k}'\uparrow, -\mathbf{k}'\downarrow) \tag{2.20}$$

yields an energy V_0 if $\mathbf{k}$ and $\mathbf{k}'$ are in the scattering shell $E_F < E_k$, $E_{k'} < E_F + \hbar\omega_D$. Many electrons can participate in this process and many Cooper pairs are formed, yielding a new state (phase) of the system. The energy of this new state is not just $\frac{N}{2}\epsilon$ less than that of the old state, since the Fermi surface is renormalized by the formation of each Cooper pair.

2.2.8 The Energy of the BCS Ground State

Of course, to study the thermodynamics of this new phase, it is necessary to determine its energy. It will have both kinetic and potential contributions. Since pairing only occurs for electrons above the Fermi surface [13], the kinetic energy actually increases: if w_k is the probability that a pair state $(\mathbf{k}\uparrow, -\mathbf{k}\downarrow)$ is occupied then

$$E_{kin} = 2\sum_k w_k \xi_k \quad \text{and} \quad \xi_k = \tfrac{\hbar^2 k^2}{2m} - E_F \tag{2.21}$$

The potential energy requires a bit more thought. It may be written in terms of annihilation and creation operators for the pair states labeled by $\mathbf{k}$

$$|1\rangle_k \quad \text{if} \quad (\mathbf{k}\uparrow, -\mathbf{k}\downarrow)\text{occupied} \tag{2.22}$$

$$|0\rangle_k \quad \text{if} \quad (\mathbf{k}\uparrow, -\mathbf{k}\downarrow)\text{unoccupied} \tag{2.23}$$

or

$$|\Psi_k\rangle = u_k|0\rangle_k + v_k|1\rangle_k \tag{2.24}$$

where $v_k^2 = w_k$ and $u_k^2 = 1 - w_k$. Then the BCS state, which is a collection of these pairs, may be written as

$$|\phi_{BCS}\rangle = \simeq \prod_k \left\{u_k|0\rangle_k + v_k|1\rangle_k\right\}. \tag{2.25}$$

We will assume that $u_k,\ v_k \in \mathfrak{R}$. Physically this amounts to taking the phase of the order parameter to be zero (or π), so that it is real. However

the validity of this assumption can only be verified for a more microscopically based theory. By the Pauli principle, the state $(\mathbf{k}\uparrow, -\mathbf{k}\downarrow)$ can be, at most, singly occupied, thus a $(s = \frac{1}{2})$ Pauli representation is possible

$$|1\rangle_k = \begin{pmatrix} 1 \\ 0 \end{pmatrix}_k \quad \text{and} \quad |0\rangle_k = \begin{pmatrix} 0 \\ 1 \end{pmatrix}_k \tag{2.26}$$

where σ_k^+ and σ_k^- describe the creation and annihilation of the state $(\mathbf{k}\uparrow, -\mathbf{k}\downarrow)$

$$\sigma_k^+ = \frac{1}{2}(\sigma_k^1 + i\sigma_k^2) = \begin{pmatrix} 0 & 1 \\ 0 & 0 \end{pmatrix} \tag{2.27}$$

$$\sigma_k^- = \frac{1}{2}(\sigma_k^1 - i\sigma_k^2) = \begin{pmatrix} 0 & 0 \\ 1 & 0 \end{pmatrix} \tag{2.28}$$

The process $(\mathbf{k}\uparrow, -\mathbf{k}\downarrow) \longrightarrow (\mathbf{k}'\uparrow, -\mathbf{k}'\downarrow)$ if allowed, is associated with an energy reduction V_0. In our Pauli matrix representation this process is represented by operators $\sigma_{k'}^+, \sigma_k^-$, so

$$V = -\frac{V_0}{L^3} \sum_{\mathbf{k}\mathbf{k}'} \sigma_{k'}^+, \sigma_k^- \tag{2.29}$$

Thus the reduction of the potential energy is given by $\langle\phi_{BCS}|V|\phi_{BCS}\rangle$

$$\langle\phi_{BCS}|V|\phi_{BCS}\rangle = -\frac{V_0}{L^3}\left\{\prod_p (u_p\langle 0| + v_p\langle 1|) \sum_{\mathbf{k}\mathbf{k}'} \sigma_k^+\sigma_{k'}^- \prod_{p'} (u_{p'}|0\rangle_{p'} + v_{p'}|1\rangle_{p'})\right\} \tag{2.30}$$

Then as ${}_k\langle 1|1\rangle_{k'} = \delta_{kk'}, {}_k\langle 0|0\rangle_{k'} = \delta_{kk'}$ and ${}_k\langle 0|1\rangle_{k'} = 0$

$$\langle\phi_{BCS}|V|\phi_{BCS}\rangle = -\frac{V_0}{L^3} \sum_{kk'} v_k u_{k'} u_k v_{k'} \tag{2.31}$$

Thus, the total energy (kinetic plus potential) of the system of Cooper pairs is

$$\Xi_{BCS} = 2\sum_k v_k^2 \xi_k - \frac{V_0}{L^3} \sum_{kk'} v_k u_{k'} u_k v_{k'} \tag{2.32}$$

As yet v_k and u_k are unknown. They may be treated as variational parameters. Since $w_k = v_k^2$ and $1 - w_k = u_k^2$, we may impose this constraint by choosing

$$v_k = \cos\theta_k \quad u_k = \sin\theta_k \tag{2.33}$$

At $T = 0\,\mathrm{K}$ we require Ξ_{BCS} to be a minimum.

$$\begin{aligned}\Xi_{BCS} &= \sum_k 2\xi_k \cos^2\theta_k - \tfrac{V_0}{L^3}\sum_{kk'} \cos\theta_k \sin\theta_{k'} \cos\theta_{k'} \sin\theta_k \\ &= \sum_k 2\xi_k \cos^2\theta_k - \tfrac{V_0}{L^3}\sum_{kk'} \tfrac{1}{4} \sin 2\theta_k \sin 2\theta_{k'}\end{aligned} \tag{2.34}$$

$$\frac{\partial \Xi_{BCS}}{\partial \theta_k} = 0 = -4\xi_k \cos\theta_k \sin\theta_k - \frac{V_0}{L^3}\sum_{kk'} \sin 2\theta_k \sin 2\theta_{k'} \tag{2.35}$$

$$\xi_k \tan 2\theta_k = -\frac{1}{2}\frac{V_0}{L^3}\sum_{k'} \sin 2\theta_{k'} \tag{2.36}$$

Conventionally, one introduces the parameter $E_k = \sqrt{\xi_k^2 + \Delta^2}$, where $\Delta = \frac{V_0}{L^3}\sum_k u_k v_k = \frac{V_0}{L^3}\sum_k \cos\theta_k \sin\theta_k$. Then we get

$$\xi_k \tan 2\theta_k = -\Delta \rightarrow 2u_k v_k = \sin 2\theta_k = \frac{\Delta}{E_k} \tag{2.37}$$

$$\cos 2\theta_k = \frac{-\xi_k}{E_k} = \cos^2\theta_k - \sin^2\theta_k = v_k^2 - u_k^2 = 2v_k^2 - 1 \tag{2.38}$$

$$w_k = v_k^2 = \frac{1}{2}\left(1 - \frac{-\xi_k}{E_k}\right) = \frac{1}{2}\left(1 - \frac{\xi_k}{\sqrt{\xi_k^2 + \Delta^2}}\right) \tag{2.39}$$

After substituting Eq. 2.37 into Eq. 2.34, we get

$$\Xi_{BCS} = \sum_k \xi_k \left(1 - \frac{\xi_k}{E_k}\right) - \frac{L^3}{V_0}\Delta^2 \tag{2.40}$$

Compare this to the normal state energy, again measured relative to E_F

$$\Xi_n = \sum_{k<k_F} 2\xi_k \tag{2.41}$$

or

$$\frac{\Xi_{BCS} - \Xi_n}{L^3} = -\frac{1}{L^3}\sum_k \xi_k \left(1 + \frac{\xi_k}{E_k}\right) - \frac{\Delta^2}{V_0} \tag{2.42}$$

$$\approx -\frac{1}{2} Z(E_F)\Delta^2 < 0 \tag{2.43}$$

This can also be interpreted as $\Delta Z(E_F)$ electron pairs per volume condensed into a state Δ below E_F. The average energy gain per electron is $\Delta/2$. As a result, the formation of superconductivity reduces the ground state energy. However, in the case of high-T_c cuprates, other interactions than the weak phonon-mediated attractive interaction play a more pronounced role.

2.3 The electronic phase diagram of high-T_c cuprates

Cuprate superconductors are generally referred to as doped Mott insulators. To understand the origin of this terminology, we begin with an investigation of the cuprate crystalline and electronic structures. All high T_c superconductors share the following two elements: the CuO_2 planes that form single-layer or multi-layer conducting blocks per unit cell, and the charge reservoirs in between the CuO_2 planes that are responsible for contributing either electrons or holes to the CuO_2 planes. In Fig. 2.11, three representative cuprate superconductors, the one-layer hole-doped $La_{2-x}Sr_xCuO_4$ (LSCO), the one-layer electron-doped $Nd_{2-x}Ce_xCuO_4$ (NCCO) [14], and the infinite layer $Sr_{1-x}La_xCuO_2$ (SLCO), are illustrated as examples. It is understood that the electronic states of the CuO_2 planes control the physics of high T_c superconductivity. By doping with substitution elements or by changing the oxygen content (as in $YBa_2Cu_3O_{6+\delta}$) in the charge reservoirs, the carrier density in the CuO_2 planes can be controlled. In the undoped parent compound, the electronic states of the Cu on the plane are in the d^9 configuration. The presence of octahedral oxygen surrounding the central Cu ion and the associated Jahn-Teller distortion split the degenerate e_g orbitals of Cu d^9 with the resulting highest partially occupied orbital being $d_{x^2-y^2}$. The Cu $d_{x^2-y^2}$-orbital and the doubly occupied O p_x, p_y-orbitals form a strong covalent bonding. In the absence of interaction among electrons, the hybridization of these three orbitals gives rise to the bonding, non-bonding and half-filled anti-bonding bands and predicts a good metal, in sharp contrast to the large charge gap observed in the undoped compounds. The failure of the band theory, and hence that of the conventional Fermi liquid approach to high T_c problems, stems from the existence of a large on-site Coulomb interaction that well exceeds the bandwidth of the tight-binding anti-bonding band. If a charge carrier were to hop onto a partially filled Cu $d_{x^2-y^2}$ orbital, the two Cu $d_{x^2-y^2}$ carriers would experience a large energy penalty, and, hence, it is energetically more favorable to localize the electrons. Electronic systems with half-filled states and strong localizations are known as Mott insulators. Specifically, the strong on-site Coulomb repulsion suppresses charge fluctuations, splits the half-filled anti-bonding band into an empty upper-Hubbard band and a filled lower-Hubbard band, thereby turning a band metal into a Mott insulator with an optical gap of a few eV. More precisely, in the cuprate systems, the energy penalty of having a second

hole in the Cu d-orbital is much larger than the energy separation between the Cu $d_{x^2-y^2}$ and O p-orbitals. Thus, the extra hole primarily goes to the O p_x, p_y orbitals, and the energy cost $(E_p - E_d)$, of the order of $\sim 2\,\mathrm{eV}$, is named the charge transfer gap. Because the hybridization integral, t_{dp}, is much smaller than the energy barrier $(E_p - E_d)$, the electrons in the undoped compounds form localized moments on the Cu sites. These spins are anti-ferromagnetically aligned via the super-exchange interaction that involves virtual hopping to the neighboring O p-orbitals. As a result, the parent compounds of high T_c materials are referred to as anti-ferromagnetic Mott insulators. When charge carriers are introduced to the CuO_2 planes, several novel phases appear as exemplified in Fig. 2.12. This section provides an overview of the electronic phase diagrams of cuprates and summarizes the most important phenomena shared among all cuprate superconductors. We remark that the physics of cuprate superconductors is extremely rich, and therefore a simplified phase diagram such as that shown in Fig. 2.12 cannot capture many interesting details that take place in different cuprate systems. As mentioned above, at zero doping, the electronic state of the parent compound is an anti-ferromagnetic Mott insulating state for both the n-type (electron-doped) and the p-type (hole-doped) cuprates. Chronologically, soon after the discovery of La_2CuO_4, long-range Néel spin ordering in this system was experimentally determined [15, 16]. Strictly speaking however, the Hohenberg-Mermin-Wagner theorem asserts that an ideal two-dimensional (2D) magnetic system with isotropic anti-ferromagnetic Heisenberg couplings would remain magnetically disordered at finite temperature. The finding of long-range anti-ferromagnetic ordering in real systems can be reconciled with theory by relaxing the strict 2D picture and incorporating three-dimensional (3D) anisotropic effects. The anisotropic effects in cuprate can arise through many different ways. For instance, in addition to the dominant 2D Heisenberg term, there are small interlayer coupling, Dzyaloshinski-Moriya (DM) anisotropic coupling and easy-plane $(x-y)$ anisotropic coupling terms in the real and spin space Hamiltonian [17]. In orthorhombic systems, such as La_2CuO_4, DM and interlayer anisotropy stabilize the 3D long-range anti-ferromagnetic phase [18, 19]. In tetragonal systems, such as Nd_2CuO_4, where the former two anisotropies are absent, $x - y$ anisotropy results in a crossover from the 2D Heisenberg behavior to the 2D XY regime, followed by a crossover to the 3D XY regime, and hence stabilizes the long-range Néel order [19, 20]. As holes are introduced to the CuO_2 planes, the Néel

temperature of the system decreases rapidly upon doping. Moreover, the commensurate anti-ferromagnetic (AFM) long-range order disappears completely at around $x \approx 0.03$, where x is the number of doped holes per Cu. Above this doping level, various types of spin fluctuations replace the original commensurate AFM order and continue to survive in the superconducting phase. In $La_{2-x}Sr-xCuO_4$, static incommensurate spin fluctuations develop beyond the Néel state and persist in the superconducting state, while in other compounds, such as $YBa_2Cu_3O_{6+\delta}$, commensurate magnetic resonance modes and significant dynamic spin fluctuations coexist with superconductivity in the underdoped and optimally doped region. When hole-doping is further increased, superconductivity sets in at $x \approx 0.05$ and lasts up to $x \approx 0.25$. There is general consensus that the pairing symmetry of the superconducting order parameter of hole-doped cuprates is predominantly $d_{x^2-y^2}$ -like in the underdoped and optimally doped[2] region [21, 22]. In the heavily overdoped limit, on the other hand, a significant s-wave component in addition to the $d_{x^2-y^2}$ component has been revealed [23]. In the normal state of the underdoped cuprates, various phenomena associated with a partially suppressed density of states around the Fermi level and an opening of the spectral gap in the spin and charge fluctuations have been observed [24]. This state is termed as the pseudogap phase (Chapter 2.6). Near the optimal doping, the pseudogap phase crosses over to an anomalous non-Fermi liquid region where quantum critical scaling behavior in the spin and charge density fluctuations is suggested [25, 26]. As we further increase the doping to the overdoped range, conventional Fermi liquid physics is eventually recovered. On the electron-doping side, despite an overall similarity, we notice that the AFM state exists over a wider doping range and the superconducting region is much narrower in comparison with that of the hole-doped cuprates. An intuitive way to visualize the robustness of the AFM order in the electron-doping phase diagram is the spin-dilution picture. While the hole doping introduces carriers to the O p-orbitals, the electron doping takes place in the Cu d-orbital. The resulting mobile spinless Cu $3d^{10}$ configuration dilutes the background anti-ferromagnetic coupling and leads to a gradual reduction of the Néel temperature [27]. The suppression of T_N is comparable to that observed in the Zn-doped La_2CuO_4 [28, 29] where the doped Zn with

[2] The optimal doping $x = 0.15$ is defined as the doping concentration with the highest transition temperature $T_c(x_0)$. Underdoping refers to the doping level where $x < x_0$, and overdoping refers to $x > x_0$.

a localized $3d^{10}$ configuration dilutes the AFM order of the Cu spins. In contrast, the doped holes in the O orbitals induce ferromagnetic coupling between adjacent Cu spins, strongly frustrating the anti-ferromagnetic background [30]. Therefore, the Néel temperature drops rapidly with increasing hole doping, and the resulting AFM phase is much narrower in the hole-doped cuprates. In the normal state of the n-type cuprates, no discernible zero-field low-energy pseudogap is observed by the tunneling and photoemission spectroscopy measurements, although, upon the application of a large magnetic field that fully suppresses superconductivity, a partial tunneling gap is again detected [31, 32, 33] (Chapter 2.6). Besides, the electronic properties of the normal state measured by the transport and zero-field tunneling experiments are more conventional, similar to what the Fermi-liquid region in the overdoped p-type cuprates exhibits.

The high-temperature cuprate superconductors are based on a certain class of ceramic materials. All share the common feature of square planar copper-oxygen layers separated by charge reservoir layers. These block layers serve to donate charge carriers to the CuO_2 planes. Shown in Fig. 2.11 is the crystal structure for the canonical single layer parent material La_2CuO_4 (LCO) and Nd_2CuO_4 (NCO). These undoped materials are antiferromagnetic insulators. With the partial substitution of Sr for La in La_2CuO_4, holes are introduced into the CuO_2 planes. This is shown in the phase diagram of cuprate superconductors (Fig. 2.12). The Néel temperature precipitously drops and the material at some finite doping becomes a superconductor. As shown in Fig. 2.12, approximately the same behavior exists upon doping the CuO_2 planes with electrons. The similarities and differences observed upon doping with the two signs of charge carriers will be discussed in more detail below. The high-T_c phase diagram is characterized by the obvious existence of two distinct phases. At half-filling (one charge carrier per site) the antiferromagnetic state is described by the basic Heisenberg Hamiltonian

$$H = \sum_{i\delta} S_i \cdot J \cdot S_{i+\delta} \tag{2.44}$$

where the sum over i is a sum over Cu spins and J is the exchange coupling. Note that in addition to the two dimensional (2D) Heisenberg terms there is a coupling between spins in neighboring layers, made smaller because of frustration effects. Each spin has two parallel spins and two antiparallel spins that are equidistant in the tetragonal phase. In $La_{2-x}Sr_xCuO_4$ the small

orthorhombic distortion lifts the frustration and results in a residual antiferromagnetic coupling between layers. It is this interplanar coupling that allows true long-range order in the 2D plane, as otherwise via Hohenberg-Mermin-Wagner considerations the only long range ordered state would be at T = 0 [34]. In Eq. 2.44 the spin anisotropies are reflected by the fact that the exchange term J is a tensor. In a pure tetragonal structure, like K_2NiF_4, J would be diagonal and a vectorial representation would be possible. The other distinct phase of the cuprate phase diagram is of course superconductivity. The superconducting state and symmetry of its order parameter will be discussed in more detail in Chapter 2.5, but let it suffice to say for now that these materials have properties different from typical low-T_c BCS superconductors. Most obvious is the symmetry of their order parameter, which

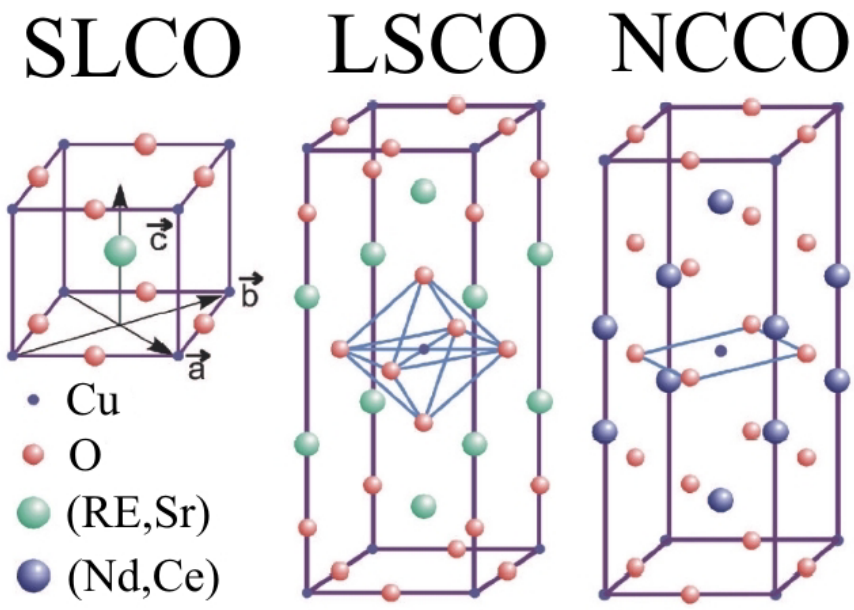

Fig. 2.11: Crystalline structures of representative hole-doped and electron-doped cuprates: electron-doped $Sr_{1-x}La_xCuO_2$ (SLCO), hole-doped T-$La_{2-x}Sr_xCuO_4$ (LSCO), and electron-doped T′-$Nd_{2-x}Ce_xCuO_4$ (NCCO) [14]. Note the absence of apical oxygen in all electron-doped cuprates, in contrast to the presence of CuO_6 octahedron in hole-doped cuprates. Furthermore the infinite-layer system (SLCO) differs from all others in that no excess charge reservoir exists between consecutive CuO_2 planes.

is now more or less universally agreed to be of higher order $d_{x^2-y^2}$ symmetry. This has important implications for the low-energy properties of the superconducting state and it sheds light on the nature of the superconducting

mechanism.
Aside from its symmetry, the superconducting state of the high-T_c's may also differ from that of the BCS superconductors in its low superfluid density deriving from the low carrier density of the doped Mott insulator. This gives relatively small phase-stiffness and poor screening which leads to large phase fluctuations and a non-mean field superconducting transition. The small superfluid density has led to proposals that the phase coherence energy scale and the pairing energy scale are separated and have opposite doping dependencies. In the underdoped regime, preformed pairs may form at a higher temperature than T_c, and it is with the Bose-Einstein condensation of these pairs that superconductivity occurs [35]. It is the fulfillment of both these conditions that allows the occurrence of superconductivity. For the antiferro-

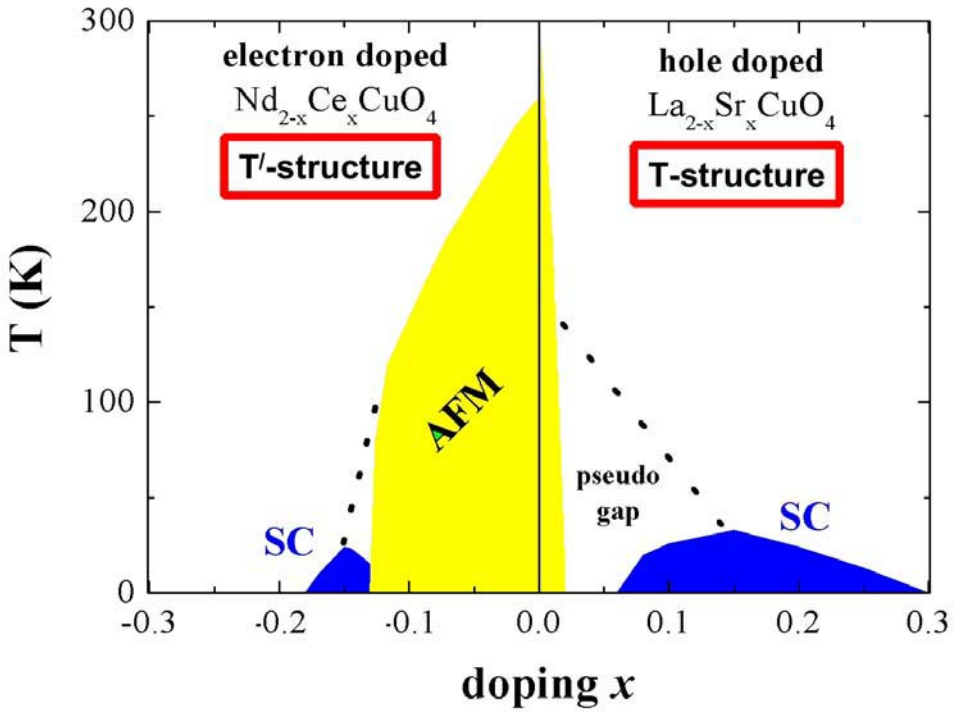

Fig. 2.12: The phase diagram of the cuprate superconductors. Adapted from Ref. [36].

magnetic material, the Hamiltonian represented by Eq. 2.44 gives low-lying

magnon excitations that well describe the low-energy degrees of freedom with the consideration of relevant anisotropies [17]. Not as clear is what happens to the normal state properties when the material is doped away from half-filling. In the discussion below, let us consider the case of hole doping, as the vast majority of experiments have been done on the hole-doped (p-type) compounds, their properties are the ones most modeled, and because it will serve as a counterpoint to the electron-doped compounds discussed in the next section. The phenomenology of the doped compounds is characterized by breaking up the phase diagram into under-, optimal-, and overdoped regimes. As holes are introduced to the CuO_2 planes, the material quickly loses its antiferromagnetic phase and moves into a so-called strange metal phase. At very low doping levels, the materials resemble semiconductors with polaronic charge carriers. At slightly higher doping levels, but below the doping level that gives the highest T_c, these compounds can be characterized as metals. However, the description of this normal state escapes modeling by the conventional theory of metals. Inferred from a variety of probes is a

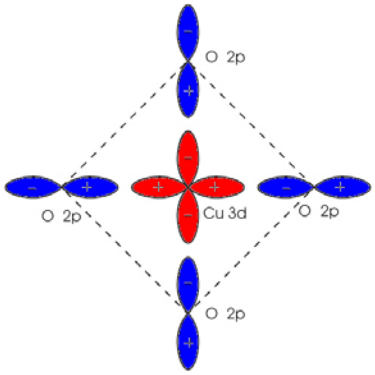

Fig. 2.13: Schematic diagram of a single CuO_4 cluster and the hybridization of the Cu $3d^9$ hole with the surrounding O $2p$ hole states.

large suppression in the low-energy density of states, i.e., a pseudogap [24]. Pseudogap signatures are seen in ARPES, infrared, Raman, tunneling, DC resistivity, and specific heat measurements among others [24]. Most experiments sensitive to this pseudogap indicate a temperature (referred to as T*) that it opens. Although techniques differ as to what the exact temperature is, they generally agree that the T* line falls monotonically with increased doping and that it merges somewhat smoothly with T_c near the top of the superconducting dome.

The fact that the pseudogap appears to merge smoothly with T_c has led to proposals that it is intimately related to the superconducting gap. This point will be addressed later as our measurements on $Pr_{2-x}Ce_xCuO_4$ may be able to shed light on it. However, many measurements show, that there are two distinct pseudogap energy scales, of which neither, one, or both may be related explicitly to superconductivity. For underdoped samples there is a clean leading edge gap in the normal state that has been claimed to be indicative of pairing fluctuations [24, 37]. At higher binding energy ($\sim$200 meV) there is a large hump feature. Alternatively this high-energy pseudogap could be viewed as a suppression of spectral weight over a large energy range near-E_F. The fact that in p-type materials both of these features show a similar d-wave symmetry and in the extreme underdoped samples the distinction between the two gets blurred has led to proposals that they share a common origin.
Neutron scattering and nuclear magnetic resonace (NMR) measurements show the large remnant of antiferromagnetic spin fluctuations that are still present in this underdoped regime. They are obviously weaker and broader than in the antiferromagnetically ordered state, but persist until the material is overdoped. There are differences between materials as to whether or not the fluctuations remain commensurate at (π, π) or not. In few materials (notably T-$La_{2-x}Sr_xCuO_4$) the incommensurability gives strong evidence for spin-charge ordering or fluctuations into one-dimensional stripes [38]. The incommensurability parameter δ of both x-ray (sensitive to charge) and neutron (sensitive to spin) has been shown to be proportional to the doping for $x < \frac{1}{8}$. This is consistent with a picture where domains of one dimensionally ordered charge stripes are created. A similar incommensurability has also been found in $YBa_2Cu_3O_{7-\delta}$ (Y123) [39].
As one moves towards optimal doping pseudogap effects get less pronounced, although they may still exist at the lowest energy scales. In the highest-T_c optimally doped p-type materials many of the temperature and frequency dependent probes (DC resistivity, optics, width of ARPES[3] features) show a striking linear dependence up to many hundreds of degrees or meV in the normal state. Varma *et al.* postulated that this linearity is due to a coupling of charge carriers to critical fluctuations from a nearby quantum critical point [25]. This was termed marginal Fermi liquid. However as pointed out by others (most recently by Allen [40]) the resistivity above T_c is actually well fit by conventional electron-phonon scattering theory as described by

[3] Angle resolved photo emission spectroscopy

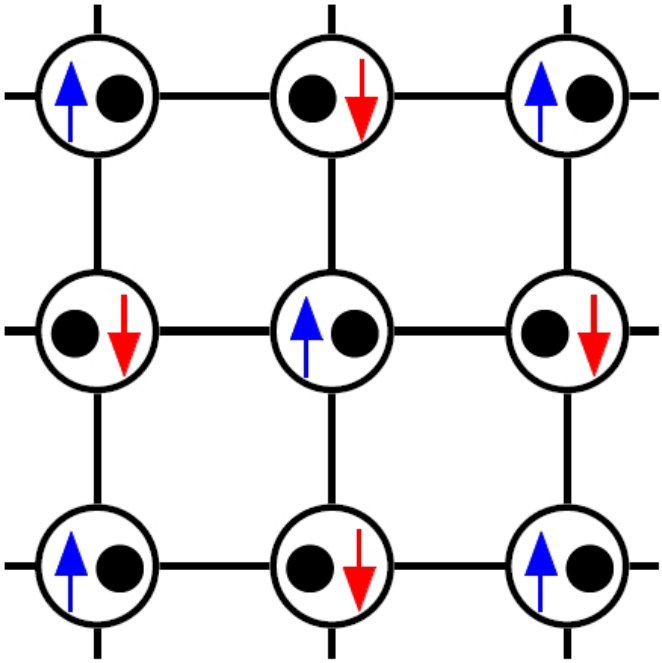

Fig. 2.14: Schematic of antiferromagnetic half-filled square lattice. Electrons can hop to nearest neighbor sites only if the adjoining site's spin is anti-aligned.

the Bloch-Grüneisen equations. It may be that the strikingly straight temperature dependence is due to the unfortunate occurrence of 90 K superconductivity that obscures the normal metal low temperature behavior. In the overdoped regime, the linear dependence of the resistivity begins to acquire a power law dependence with an exponent greater than 1. In well overdoped samples it may be roughly quadratic thereby having been termed more Fermi liquid-like. This is important because if the cuprates are Fermi liquids in the overdoped regime and there are no intervening phase transitions[4] as one underdopes then all the anomalous physics at low dopings are relegated to the category of messy details and not indicative of a new state of matter *a la* resonant valence bound theory (RVB).

[4] Reports of a quantum phase transition as a function of doping do exist; see Ref. [41].

2.4 Electron doped cuprates

$Pr_{2-x}Ce_xCuO_{4\pm\delta}$ is a member of the small family of cuprate superconductors that can be doped with electrons [42]. Other members of this material class with the chemical formula $RE_{2-x}M_xCuO_4$ include substitutions where RE = La, Pr, Nd, Sm or Eu and M = Ce or Th [43]. These are all single-layer compounds which, unlike their brethren 214 systems (for instance T crystal structured $La_{2-x}Sr_xCuO_4$), possesses a T′ crystal structure, characterized by a lack of oxygen in the apical position[5] (see Fig. 2.11). It is found experimentally that only T′ crystal structures appear to accept electron doping and structures with apical oxygen (like T) can only be doped with holes. This can be understood within a Madelung potential analysis, where strong modification of the local ionic potential on the Cu site is expected by the inclusion of an O^{2-} ion immediately above it [45]. As doped electrons are expected to primarily occupy the Cu site, while doped holes primarily occupy in-plane O sites these considerations play a large role in the underlying physics. In addition to T′-structure cuprates, there exist the so called "infinite layer cuprates" ($Sr_{1-x}La_xCuO_2$). The crystal consists of CuO_2 planes separated by (Sr^{2+}, La^{3+}) ions where the copper is not a Jahn-Teller ion.
The most dramatic difference between electron- and hole-doped materials is in their phase diagrams. Only an approximate symmetry exists about the zero doping line between p- and n-type, as the antiferromagnetic phase is much more robust in the electron-doped material and persists to much higher doping levels[6]. Superconductivity occurs in a doping range that is almost five times narrower. In addition, these two ground states occur in much closer proximity to each other. From neutron scattering, in contrast to many p-type compounds, spin fluctuations remains commensurate where they can be resolved [47, 48]. One approach to understanding the differences in the extent of the antiferromagnetic region is to consider spin-dilution models. It was shown that Zn doping into T-La_2CuO_4 reduces the Néel temperature at a similar rate as Ce doping in $Nd_{2-x}Ce_xCuO_{4\pm\delta}$ [28]. Since Zn substitutes in a configuration that is nominally a d^{10} filled shell, it can be regarded as a spinless impurity. In this regard Zn substitution can be seen as simple dilution of the spin system. The similarity with the case of Ce doping into

[5] Note: There is also an oxygen rich phase found, e. g. $Nd_2CuO_{4.17}$ ($Nd_{12}Cu_6O_{25}$), but it crystallizes monoclinically (C2/m) [44]

[6] This result has been proposed for a long time after the experiments by Luke *et al.* [46]

$Pr_{2-x}Ce_xCuO_{4\pm\delta}$ implies that electron doping serves to dilute the spin system by neutralizing the spin on a d^9 site. It was subsequently shown that the reduction of the Néel temperature in these n-type compounds comes through a continuous reduction of the spin stiffness, ρ_s, which is consistent with this model [27]. This comparison of Ce with Zn doping is compelling, but cannot be exact as Zn does not add itinerant charge carriers like Ce does, as its d^{10} electrons are tightly bound and can more efficiently frustrate the spin order. This point of view may have some validity, though can be seen by the fact that applied to hole doping, it consistently explains the asymmetry of the AF phase on the two sides of the phase diagram. Aharony proposed that the reason hole-doping requires a much smaller density of holes than primarily exist on the in-plane oxygen atoms and result in spin-frustration instead of spin-dilution [30]. It was proposed that the exchange interaction between the doped hole on the oxygen site and the holes on neighboring Cu site mediate an effective ferromagnetic interaction between Cu spins. The oxygen-hole/copper-hole interaction, whether ferromagnetic or antiferromagnetic, causes the spins of adjoining Cu-holes to align. This interaction competes with the antiferromagnetic superexchange and frustrates the Néel order; a small density of doped holes has a catastrophic effect on the long-range order. This additional frustration does not occur with electron doping as electrons are primarily introduced onto Cu sites and hence no frustration occurs.

The differences upon electron and hole doping have also been purportedly understood by considering the differences in sign of the higher-order hoppings within the context of $t - t' - t'' - J$ model [49, 50]. A large next-nearest-neighbor hopping term t' can serve to stabilize the Néel state as it facilitates hopping on the same sublattice. As the parameterization of the hole-doped $t - t' - t'' - J$ has $t' < 0$ and the electron doped material $t' > 0$ by these considerations has a greater stability of the Néel state. However, it may be that a complete treatment that includes t' explicitly, must also include next-nearest-neighbor spin-interaction $J' = t'^2/4$ (discussed below) which will frustrate the nearest-neighbor interaction [50]. Yet another scheme to understand the dissimilarities between the doping dependence of the magnetism with holes or electrons has been with spin fluctuations models that start from a Hubbard Hamiltonian in the weak coupling limit with $t > U$ [51]. This approach assumes a Fermi Surface (FS) that changes volume with doping and typically neglects t'' terms. For electron doping, this means that

the FS just coincides with the antiferromagnetic Brillouin zone boundary near $(\pi/2; \pi/2)$. In the electron-doped compounds the magnetism is mediated by the nesting between these approximately flat sections of Fermi surface. The underlying band structure is such that the position of the FS near

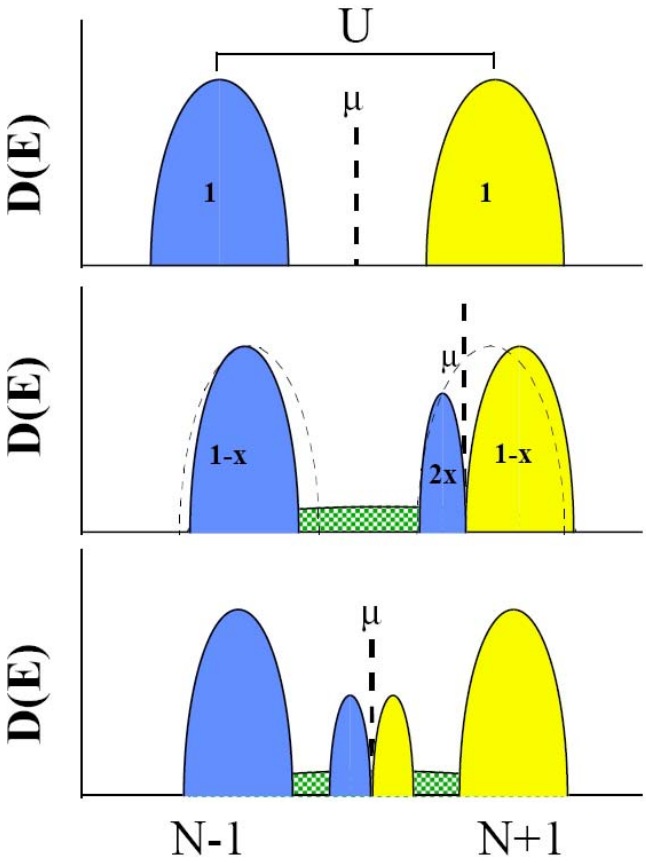

Fig. 2.15: A scheme of the Hubbard model for the CuO_2 square plaquettes. The top panel represents the half-filled case. In the middle panel is the simplest scenario where the chemical potential moves into the upper Hubbard band with electron doping. The green shaded area represents impurity states or excitonic effects that do not play a direct role in the low-energy properties. The bottom panel shows states being created inside the insulator's gap. Yellow represent $N+1$ excitation spectra and blue represents $N-1$ excitation spectra.

$(\pi/2; \pi/2)$ is relatively incompressible for electron addition and hence gives a large stability with doping and spin- fluctuations remain commensurate. In the hole-doped compound the magnetism is mediated by nesting between

the extended van Hove singularities near (π; 0). In the p-type case the FS rapidly vanishes with doping near (π; 0). This changes the nesting between Fermi patch regions and, in this picture, is the reason that the Néel temperature falls precipitously and the spin fluctuations become incommensurate. Experiments show other contrasting behavior between n-type superconductors and their p-type counterparts. There is a much touted T^2 dependence of the in-plane resistivity that may be evidence for more-Fermi liquid-like behavior [52]. This behavior exists over a relatively large doping range for $Pr_{2-x}Ce_xCuO_4$. This is in contrast to the p-type materials, which show such a T^2 dependence of the resistivity only in the heavily overdoped regime. It is interesting to note that many of the normal state properties of the highest T_c samples of the n-type materials are similar to those of the overdoped p-type compounds. Whether there is an intrinsic connection between them and the highest T_c samples of the n-type materials can be seen as overdoped remains an open question. To investigate this, one must take into account the differences in FS shape and spin fluctuation spectrum. In contrast to the p-types these materials possess a negative Hall sign[7] over much of the superconducting doping regime. At first glance this confirms their n-type character, but is somewhat hard to understand given that ARPES measurements show the Fermi surfaces of electron and hole-doped materials to not have gratuitously different topologies. Moreover, they show an anomalous temperature induced sign reversal of the Hall coefficient near optimal doping that cannot be understood with conventional transport theory without invoking the existence of two bands [54, 55, 56]. For much of their history it was believed that the pairing symmetry in the electron-doped compounds was s-wave [57, 58, 59, 60]. This picture has changed recently and now it seems the n- and p-type compounds appear to share a superconducting d-wave pairing symmetry [61, 62, 63, 64]. Some differences in the superconductivity do exist, for instance, the $2\Delta_{sc}/k_BT_c$ ratio of the n-type material is much smaller than that of its optimally-doped p-type counterparts [65]. Thus far, no signal resembling a 41 meV (π, π) resonance mode has been reported and hence, more neutron scattering experiments are required [47, 48]. Another rarely mentioned aspect of the electron-doped system is the large magnetic

[7] Suzuki *et al.* [53] showed that the effect of oxygen reduction on the hall coefficient R_H and resistivity ρ for $Nd_{2-x}Ce_xCuO_{4\pm\delta}$ thin films is serious and that the algebraic sign of R_H for superconducting samples can be positive. The result was interpreted in terms of band structure effects rather than the two-band model.

moment developed in the crystal electric field by the core $4f$ electrons of the rare earth ions (Nd for instance). This large crystal field comes from the low positional symmetry at the rare earth site. Such a field strongly splits the energy levels of the $4f$ states and gives, with Hunds rule considerations, an electronic ground state with a large magnetic moment [66, 67].

2.4.1 Doping dependence of electron doped cuprates

It is generally accepted that the high-temperature superconductors belong to a class of materials known as Mott insulators [68]. At half-filling (one charge carrier per site) these materials, predicted to be metallic by band theory, are insulating due to the large on-site Coulomb repulsion that inhibits double site occupation and hence charge conduction. The half-filled material, with its gapped charge excitations, only has antiferromagnetic spin degrees of freedom. These cuprates become metals and then superconductors when doped with charge carriers (holes or electrons). Although the general systematics of Mott insulators and certainly normal metals are understood, the question of how one may proceed from a half-filled Mott insulator with only low-energy spin degrees of freedom to a metal is unclear. Even after 20 years of research into this fundamental solid state issue in the cuprates, the manner in which this evolution occurs and the nature of electronic states at the chemical potential is unresolved. In actuality the high-T_c and cuprate materials are not Mott insulators *per se*, but are more properly characterized as charge transfer insulators. It is believed that such systems can be described by a Hubbard Hamiltonian, where oxygen derived Zhang-Rice singlet states substitute for the lower Hubbard band and the charge transfer gap Δ plays the role of an effective U. In the following discussion the terms Mott and charge transfer insulator are used somewhat interchangeably. As detailed above, within the Hubbard model, Mott insulators are described as a single metallic band that is split into an upper Hubbard band (UHB) and a lower Hubbard band (LHB) by a correlation energy U that represents the energy cost for a site to be doubly occupied, as shown in the top panel of Fig. 2.15. Thus, at half-filling the LHB (UHB) is totally occupied (unoccupied) with the chemical potential inside the insulator's gap. In the simplest picture, the chemical potential shifts into the LHB or UHB respectively with a concomitant transfer of spectral weight across the correlation gap [69], as the material is doped away from half filling with a few holes or electrons

(middle panel of Fig. 2.15). A transfer of spectral weight occurs due to the many body nature of these correlated bands. The upper and lower Hubbard bands are not bands *per se*, but are more properly excitation spectra that represent the total weight for $N+1$ or $N-1$ excitations respectively (electron addition and subtraction spectra). If the system was a semiconductor, the chemical potential would move into the UHB as electrons are doped. For x doped electrons one would obviously observe occupied spectral weight = 1 in the LHB, occupied weight x in the UHB and unoccupied weight $1-x$ in the UHB. In a purely ionic picture ($t = 0$) the *occupied* weight of the lower Hubbard band and the *unoccupied* weight of the upper Hubbard band are both proportional to the number of sites that are singly occupied. As one dopes electrons to the material the number of singly occupied sites decreases and therefore the occupied weight of the lower Hubbard band decreases. If we doped x electrons into the system, the number of electrons on singly occupied sites becomes $1-x$ and the number of electrons on doubly occupied sites becomes $2x$ (there are x sites with 2 electrons each). This conserved spectral weight reappears as additional occupied weight of the upper Hubbard band. Every doped electron counts double in the upper Hubbard band (one doped electron can be added to an already filled site, but two electrons can be removed from the site with the same energy). A symmetric situation exists for hole-doping. In an alternative scenario the act of doping creates "states" inside the insulator's gap and as a result the chemical potential is more or less pinned to these states inside the gap (bottom panel of Fig. 2.15). It has been proposed that these states can be created in a number of ways. These may be impurity states created by doping that become metallic when some sort of percolation threshold is reached. However, it is difficult to see how this may happen in some samples with metallic conduction for very low dopings as well how a universal mechanism for creating these states could exist across all the cuprates with very different doping requirements[70]. Phase separated systems (stripes or other) may also show in-gap states. A thermodynamically necessary requirement for phase separation is that the chemical potential must be constant for a large region of doping. For the chemical potential to be constant, a mechanism must exist for the creation of intragap states. In dynamic mean field theory (DMFT) it is proposed that the Mott insulating state breaks down by the creation of coherent spectral weight in the gap [71]. Some aspects of this picture of a doped Mott insulator have been confirmed in the cuprates. In particular, high-energy spectroscopies

such as EELS and XAS have clearly shown a transfer of spectral weight from lower Hubbard band (LHB) to upper Hubbard band (UHB) or vice versa with electron or hole doping respectively [72, 73]. However, because the location of the chemical potential can be judged only approximately from XAS and EELS as the degree that excitonic effects play in the core hole excitation spectrum is unknown, the question of whether or not the chemical potential actually sits in either of these Hubbard bands or instead lies in mid-gap states is an open question. A definitive answer has been hampered by a lack of reliable inverse photoemission measurements, that in principle, coupled with photoemission could show where the E_F states exist with respect to the upper and lower Hubbard band. Thus far, this information has been culled from photoemission measurements only. Predictably, this information has been both contradictory and confusing [74, 75, 76]. Allen *et al.* [74] concluded from their valence band measurements of LSCO and NCCO that the chemical potential didn't move appreciably when going from $La_{1.85}Sr_{0.15}CuO_4$ to La_2CuO_4 to Nd_2CuO_4 to $Nd_{1.85}Ce_{0.15}CuO_4$ and that it was stabilized in the middle of the gap by impurity states. This was a somewhat suspect conclusion because of the large occupation of Nd $4f$ states in NCCO that makes the maximum of the valence band a very poor zero for the binding energy. Ino *et al.* [75] concluded from their doping dependence of the near-E_F weight of $La_{2-x}Sr_xCuO_4$ that weight was transferred from a CTB singlet like object at $\sim 600\,\text{meV}$ binding energy to the chemical potential and that this was consistent with the existence of phase separation. Due to the strong evidence for stripe fluctuations in this system, they concluded in favor of a stripe midgap state scenario.

2.4.2 Antiferromagnetism in the T′-structures 214 phase

As discussed above, the undoped copper oxygen plane is a Mott insulating antiferromagnet. Several authors have measured the Néel temperature of the undoped compound Pr_2CuO_4 by neutron diffraction experiments. According to them, the Néel temperature lies in the range $190 < T_N < 270\,\text{K}$ [77, 78, 79, 80, 81, 82, 83]. Néel temperatures of end-member compounds of Nd_2CuO_4-type are plotted in Fig. 2.16. Results from single-crystals as well as from powder material are included. According to the above cited reports, it is not clear whether these undoped samples have been treated by a reduction step. Since it was not possible, so far, stabilizing La_2CuO_4 in the T′-structure as

bulk material, no data are available for La. But this point is of prior interest considering the phase diagram of cuprates, irrespective of wether there is hole or electron doping. Neutron scattering experiments on doped samples

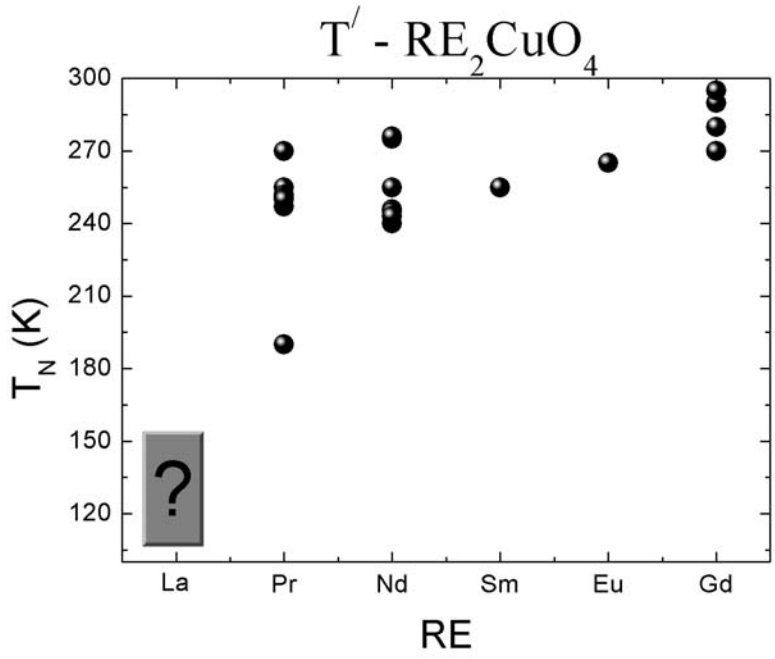

Fig. 2.16: Néel temperatures of end-member compounds RE_2CuO_4. Data points are taken from various authors [77, 78, 79, 80, 81, 82, 83, 67, 84, 85, 86, 87, 36, 88, 89]. Note that no information on the reduction process are given.

of $Nd_{2-x}Ce_xCuO_4$ by Uefuji *et al.* [90] show, that a reduction process reduces the Néel temperature by approx. 30 K for $x_{Ce} \approx 0.12$. The authors note, that identical reduction conditions have been used irrespective to the cerium content of $Nd_{2-x}Ce_xCuO_4$.
In the report of Radaelli *et al.* [91] summation over all oxygen atoms for as-grown undoped ($x = 0$) and doped ($x = 0.15$) samples gives 3.97(4) and 3.95(3). This means that already the non-reduced samples have oxygen deficiencies.
Additionally, Kuroshima *et al.* [92] synthesized $Pr_{1-x}LaCe_xCuO_4$ with $x \approx 0.11$. Within there neutron scattering experiments it was found that the non-reduced sample shows long-range antiferromagnetism with $T_N \approx 200$ K.

When this sample is reduced, superconductivity was found with $T_c \approx 25\,K$. This experiment clearly demonstrates that the apical oxygen stabilizes an antiferromagnetic ground state.

2.5 The order parameter of superconducting cuprates

The identification of the pairing symmetry is an important step towards the determination of the pairing mechanism of high-temperature superconductivity because it poses great constraints on the microscopic theory. Empirically, the Knight shift and spin-lattice relaxation measurements by the nuclear magnetic resonance (NMR) technique have shown that carriers in cuprate superconductors form singlet pairing below the transition temperature [93, 94]. Consequently, from a symmetry consideration the parity of the

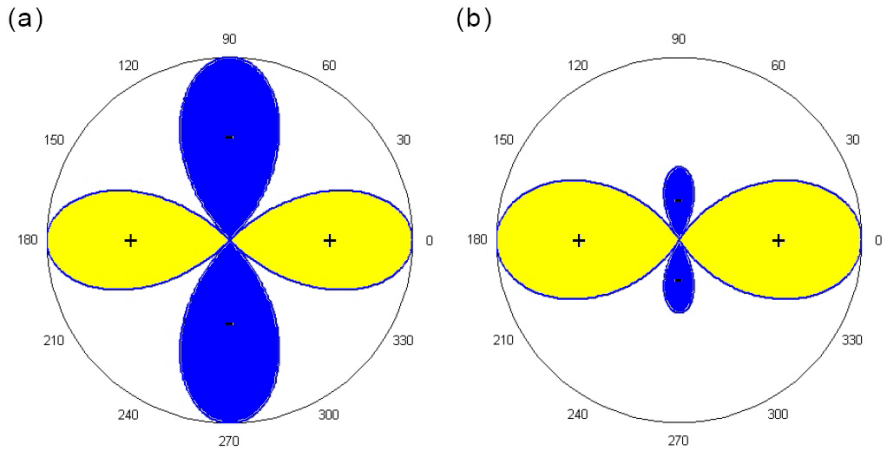

Fig. 2.17: Magnitude and phase of the superconducting order parameter as a function of direction in the momentum space. The superconducting order parameter of (a) a d-wave superconductor is given by $\Delta_d(\vec{k}) = \Delta \cos 2\theta_{\vec{k}}$, where Δ is the maximum gap value and $\theta_{\vec{k}}$ is the angle between the quasiparticle wavevector $\vec{k}$ and the antinode direction, while that of (b) a $(d+s)$-wave superconductor is $\Delta_{d+s}(\vec{k}) = \Delta[(1-x)\cos 2\theta_{\vec{k}} + x]$. In figure (b), $x = 30\%$ s-wave admixture is assumed.

(orbital) order parameter must be even. In a quasi-two-dimensional system where inter-layer coupling is sufficiently weak and electron motion is strongly confined in the CuO_2 planes, d-wave pairing is preferable because it minimizes the on-site Coulomb repulsion while retaining 2D confinement. When the inter-layer coupling strength increases, however, s-wave pairing becomes

more favorable as the system gains a larger condensation energy at the expense of the Coulomb energy. It is well established that the pairing symmetry of the underdoped and optimally doped p-type cuprates is predominately d-wave [21, 22]. Preponderant evidence from non-phase-sensitive experiments such as the angle resolved photoemission spectroscopy (ARPES) [95], thermal conductivity [96], and penetration depth measurements [97] has revealed the anisotropy of the pairing potential, the presence of line nodes, and the existence of low-energy nodal quasiparticles. Additionally, ingenious phase-sensitive techniques such as the SQUID interferometry [98], single-Josephson junction modulation [98, 99], and tricrystal scanning SQUID magnetometry [100] experiments have confirmed the change of phase across the line nodes, which is consistent with a d-pairing symmetry. Curiously, in the heavily overdoped cuprates, there is a significant s-wave component mixing into the d-wave order parameter [23]. Subsequent ARPES measurements on overdoped $YBa_2Cu_3O_{6.993}$ (YBCO) reconfirms the large in-plane gap anisotropy [101]. In addition, Raman spectroscopy results on tetragonal $Bi_2Sr_2CaCu_2O_{8+\delta}$ (Bi-2212) [102] and $Tl_2Ba_2CuO_{6+\delta}$ (Tl-2201) [103] single crystals suggest that the s-wave mixing with overdoping is a generic feature of high-T_c superconductors regardless of the crystalline symmetry. In the electron-doped cuprates, the determination of the pairing symmetry has been more controversial. While quasiparticle tunneling spectroscopy [104, 105] and earlier Raman spectroscopy [60] indicate an s-wave pairing in nearly optimally doped one-layer $Nd_{2-x}Ce_xCuO_4$ (NCCO) and $Pr_{2-x}Ce_xCuO_4$ (PCCO), tricrystal SQUID magnetometry [61], ARPES measurements [64, 106], and recent Raman spectroscopy results [107] are more consistent with d-wave pairing[8] Recently, doping-dependent pairing symmetry is observed by point-contact spectroscopy [108] and penetration depth measurements [109], where the change from d-wave pairing in the underdoped to s-wave in the optimally doped and overdoped one-layer PCCO is reported. Furthermore, scanning tunneling spectroscopy studies of the infinite-layer $Sr_{0.9}La_{0.1}CuO_2$ (SLCO) [110, 111] have identified an s-wave pairing in this simplest cuprate compound that is free of the complications from the Cu-O chain effect as in YBCO and

[8] It is worth to note that the d-wave pairing observed in ARPES [106] and Raman scattering [107] is not an exact $d_{x^2-y^2}$ symmetry, since the maximum gap is displaced away from $[\pi, 0]$ to where the Fermi surface crosses the magnetic Brillouin zone boundary, indicating a strong coupling to the background anti-ferromagnetic fluctuations in the single layer electron-doped cuprates.

the oxygen inhomogeneity induced disorder as in NCCO, PCCO, and Bi-2212. The non-universal pairing symmetry observed in electron-doped and hole-doped cuprates indicates that, instead of being a ubiquitous property of high-temperature superconductors, the symmetry of the order parameter varies with material-dependent properties including the anisotropy ratio, the on-site Coulomb repulsion and the anti-ferromagnetic coupling strength. Thus, the pairing symmetry is possibly a mere consequence of the compromise between different competing energy scales [112] rather than a sufficient condition of cuprate superconductivity.

2.6 The pseudogap

The first experiments showing evidence for a normal state gap-like feature in the hole-doped cuprates are the temperature-dependent NMR spin-lattice relaxation rate and Knight shift measurements of underdoped YBCO [112, 113]. The spectral weight of the low-frequency spin fluctuations is transferred to the high-frequency range in the normal state, and a spin gap is developed well above the transition temperature T_c. Other measurements probing the charge, spin, and single-particle excitations of underdoped p-type cuprates all hint at an opening of low-energy spectral gaps above T_c. The development of spectral gaps in spin fluctuations (as measured by the NMR spin-lattice relaxation rate), in charge fluctuations (as measured by the optical conductivity spectra via infrared reflectance [114]), and in single-particle excitation spectra (as measured by the tunneling spectroscopy [115] and ARPES [116, 117]) all takes place at different temperatures. In the phase diagram given by Fig. 2.12, we define the pseudogap temperature $T_p^\star$ as the temperature below which a suppression of electronic density of states around the Fermi level develops. While NMR, neutron scattering, transport, and optical conductivity measurements probe the reduced spin and charge scattering rates, tunneling spectroscopy and ARPES probe directly the loss of single-particle density of states. ARPES measurements of underdoped Bi-2212 reveal a normal state (leading edge) spectral gap whose magnitude and momentum anisotropy resembles the superconducting gap [116, 117], and the earlier tunneling spectroscopy measurements observe a smooth evolution of the superconducting gap into the pseudogap [115, 118]. Based on these results, some physicists speculate that the pseudogap is a precursor to the superconducting gap. There are two main categories of theories un-

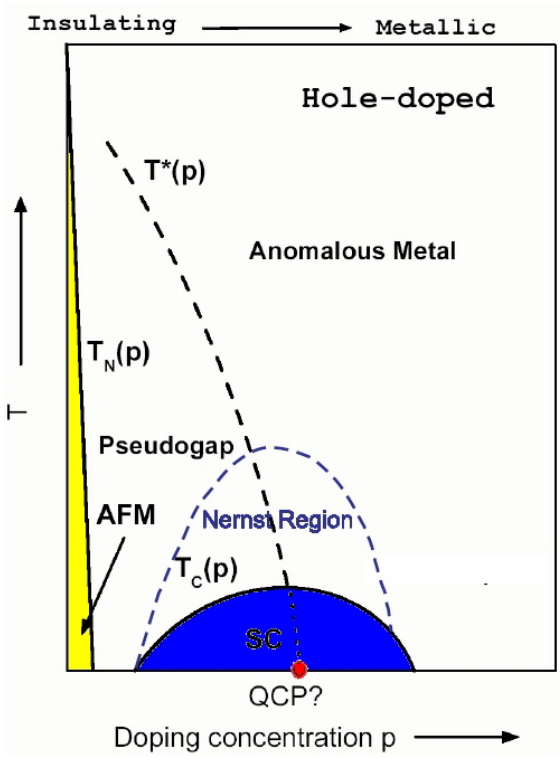

Fig. 2.18: Schematic phase diagram for the hole-doped cuprates showing that the Nernst region only covers a small part of the pseudogap phase. Note that the normal metal coincides with the anomalous metal state shown in Fig. 2.12.

der the precursor scenario: the pre-formed magnetic pairing conjecture and the pre-formed Cooper pairing conjecture. Representative theories of pre-formed magnetic pairs include the resonating valence bond (RVB) theory and its derivative, the SU(2) gauge theory [119, 120], which view the pseudogap as a spin gap opening up upon the singlet pairing below a pseudogap temperature $T^{\star}$. In the theory, the singlet pairing fluctuates and resonates among different pairs, thus restoring translational symmetry of the CuO_2 planes. This ground state is known as an RVB spin liquid state. The orbital wavefunction of such a pseudogap phase could display staggered-flux correlations [120, 121], equivalent to the d-wave superconducting correlations in the zero-doping limit [122]. By cooling the pre-formed magnetic-pair system below T_c, the singlet pairs would turn into Cooper pairs, so that long-range superconductivity becomes established. Experimental data suggestive of this scenario have been reported by the observation of a normal

state spin gap in NMR measurements [123]. However, direct observation of the proposed staggered flux phase (in which orbital currents circulate in a staggered pattern) remains elusive. Furthermore, that there is no apparent broken symmetry in an RVB spin liquid, cannot be easily reconciled with numerous experimental reports on the observation of broken symmetries in cuprates. Another version of the pre-formed magnetic pairing scenario suggests that the singlet pairing would result in a valence-bond solid (spin-Peierls state) instead of the RVB spin liquid [124]. At low temperatures, the conjecture of the bond-ordered states seems to be consistent with several experimental phenomena. However, a finite-temperature theory directly applicable to the pseudogap phase is still lacking. In the preformed Cooper pair scenario, the pseudogap phase is regarded as a state with strong superconducting phase fluctuations resulting from the small phase stiffness in high T_c cuprates [35]. The pairing potential in the pseudogap phase is non-vanishing, and hence the spectral gap is nonzero, though the phase coherence is lost. The supporting experimental evidence for the fluctuating superconducting order above T_c is provided by the Nernst experiments, where the short-range superconducting correlations are manifested as the non-zero Nernst signals [125, 126, 127]. However, the Nernst region where local superconducting order persists and phase fluctuation scenario applies is much smaller than the observed pseudogap region (Fig. 2.18). Therefore, phase fluctuations of the pre-formed Cooper pairs alone cannot account for the wide range of the pseudogap phase. Another viewpoint concerning the nature of pseudogap is based on Landaus symmetry-breaking theory where a competing order is assumed to be responsible for the pseudogap phenomena. In contrast to earlier tunneling spectroscopy with limited spatial resolution that shows smooth transition from the superconducting phase to the pseudogap phase [115, 118], recent spatially resolved scanning tunneling spectroscopy measurements indicate that there are two types of single-particle spectra with different gap values coexisting in the underdoped and optimally doped Bi-2212 samples [128, 129]. Furthermore, the interlayer tunneling spectra of Bi-2212 mesa samples demonstrate that the sharp superconducting coherence peaks coexist with a gradual hump feature at $T \ll T_c$, and that the superconducting gap vanishes above T_c while the higher energy hump background persists till $T^\star > T_c$ [130]. The ARPES measurements on $La_{2-x}Sr_xCuO_4$ [131] and the bulk specific heat measurements [41] also support the conjecture of the pseudogap phase as a competing order phase. Candidates for the competing

order include (fluctuating) stripe order [132, 133], circulating current order [134] also known as d-density wave order [135], (dynamic) anti-ferromagnetic order [136], and valence-bond-solid order [124]. Determining which orders are present in the superconducting and the pseudogap phases is one of the most important current topics of cuprate physics [120, 124, 133, 136]. In contrast to the ubiquitous presence of pseudogap above T_c in underdoped p-type cuprates [24, 116, 117], no discernible normal state single-particle excitation gap has been observed in the zero-field tunneling spectroscopy of n-type one-layer NCCO and PCCO [31, 32, 33], and no discernible normal state leading edge gap has been seen within the resolution of ARPES [137]. Nernst measurement on NCCO also exhibits negligible superconducting fluctuations above T_c [126, 138]. Furthermore, scanning tunneling spectra of infinite-layer SLCO indicate complete absence of any normal state tunneling gap, and the NMR spin-lattice relaxation rate and Knight shift measurements show that there is no normal state spin gap in this compound [139]. Only when a magnetic field exceeding the upper critical field is applied, would a normal state pseudogap appear in the tunneling spectra [32, 33]. However, such a pseudogap in n-type cuprates only appears below T_c, which apparently contradicts the precursor Cooper pairing scenario. To explain the absence of the zero-field pseudogap and the field-induced pseudogap in the electron-doped systems, we propose that the strength of the competing order in the n-type cuprates is smaller than the superconducting gap, which is opposite to their counterparts in the p-type cuprates. Only when the superconducting order is suppressed and the competing order enhanced by a large external field would the single-particle spectral gap associated with the competing order be revealed.

2.7 Strong correlation models

Interactions in conventional metals can typically be considered as a perturbation to the kinetic energy Hamiltonian; this may or may not be possible in the cuprates. The best evidence for strong and unusual interaction effects in the cuprate superconductors comes from a close look at their undoped transition-metal oxide parent compounds. These materials, which at low temperatures are antiferromagnetic[9], belong to a class of materials known as Mott insula-

[9] We will see later that this assumption is only valid if copper is six-fold coordinated.

tors [68]. It was originally pointed out by de Boer and Verweij that a number of transition metal oxides, like NiO and CoO that are predicted to be metallic by band theory (as they have an odd number of electrons per unit cell) are in fact insulating [140]. Later it was explained that the very localized d-orbitals have a large interaction energy for double site occupation and with one electron per site electrons are inhibited from hopping to an adjoining site due to the large energy cost to do so [141, 142, 143]. The low-energy physics attempting to model this behavior can be approximated by various effective Hamiltonians which are described below. But first: "Why effective Hamiltonians?" The full Hamiltonian relevant for solid-state physics is known exactly and sometimes termed as "The-Theory-of-Everything" [144]. It is

$$H = \sum_i \frac{\vec{p}_i^2}{2m_e} + \sum_{i,j} \frac{e^2}{|r_i - r_j|} + \sum_m \frac{\vec{P}_m^2}{2M_m} + \sum_{m,n} \frac{Z_m Z_n e^2}{|R_m - R_n|} + \sum_{i,m} \frac{Z_m e^2}{|R_m - r_i|} \tag{2.45}$$

It is precisely the complexity of this equation that caused Dirac's lamentation recalled in a previous section. As it is too complicated to solve exactly, it is necessary in solid state physics to eliminate those aspects deemed least relevant to the low-energy physics. Degrees of freedom are grouped together into effective parameters and Hamiltonians constructed that describe interactions between these parameters. Formally, this can be done through renormalization group methods, but is more often done through physical intuition. For example, in the Hamiltonian for tight binding models, $H = \sum_{i,j,\sigma} t_{ij} c^\dagger_{i\sigma} c_{j\sigma}$, the hopping parameters t_{ij} are single constants that represent the net effect of all kinds of hybridization between atomic orbitals. In the cuprates this term is the multisite overlap integral of the full complement of Cu $3d$, Cu $4s$ and O $2p$ states, as well as weak components of (for NCCO) Nd $4f$ and $5s$ states. It is obviously much simpler to treat this as a single effective parameter t_{ij} than including each term explicitly.

The Hubbard model is the simplest example of an effective model that can include the strong on-site Coulomb repulsion that is considered at the heart of the properties of the cuprate oxides. In the three-band Hubbard model, one simplifies the square lattice of the CuO_2 plane by three hybridized bands ($d_{x^2-y^2}$, p_x and p_y)) and an interaction term for double occupation on the Cu site. The model can be extended further by considering small interaction terms for double occupation of the O sites and intersite Cu-O interactions. These are typically neglected though as they are smaller perturbations. In

its simplest form the Hamiltonian can be written [145] as

$$\begin{aligned} H &= \epsilon_d \sum_{i\sigma} n^d_{i\sigma} + \epsilon_p \sum_{j\sigma} n^p_{j\sigma} + t_{pd} \sum_{\sigma\langle ij\rangle} (p^\dagger_{j\sigma} d_{i\sigma} + \text{H.c.}) + \\ & \quad t_{pp} \sum_{\sigma\langle jj'\rangle} (p^\dagger_{j\sigma} p_{j'\sigma} + \text{H.c.}) + U_d \sum_i n^d_{i\uparrow} n^d_{i\downarrow} \end{aligned} \tag{2.46}$$

In an ionic picture (all t's = 0) one has a central oxygen band, and a Cu band that is split by the Hubbard U. It was proposed by Zhang and Rice that a strong hybridization between the $d_{x^2-y^2}$ and p bands results in a split-off state from the main manifold of central O states [146]. One imagines a doped hole delocalizing over a CuO_4 plaquette and in a sense forming a singlet bond with the hole already residing on the Cu site. If the doping of the system is such that the chemical potential lies between the energy of this Zhang-Rice singlet and the upper Hubbard band, the singlet may play the role of an effective Hubbard band with an effective Hubbard parameter U_{eff} proportional to the charge transfer energy ($\Delta = \epsilon_p - \epsilon_d$) and an effective hopping $t_{ij} = t^2_{pd}/\Delta$. The Hamiltonian is then

$$H = \sum_{i,j,\sigma} t_{ij} c^\dagger_{i\sigma} c_{j\sigma} + U_{eff} \sum_i n_{i\uparrow} n_{i\downarrow} \tag{2.47}$$

This is equivalent to reducing the three band Hubbard model to a one band model where each CuO_4 plaquette is real space renormalized to an effective site as shown in Fig. 2.14. The summation is now a sum of nearest neighboring plaquettes and as such t_{ij} is an effective hopping term that represents hopping between plaquettes. The attentive reader will notice that the justification for the reduction of the three-band Hubbard model to a one-band model was very "hand-waving" and lacked rigor. It should be pointed out that while the one band Hubbard model (Eq. 2.47) is symmetric upon electron and hole doping, the more realistic three band model is not electron-hole symmetric. It may be that the assumptions that go into the three-band to one-band reduction are unrealistic and that this could be a starting point to justify the somewhat different phenomenology of the p- vs. n-type materials as electrons are doped onto Cu sites and holes onto O sites. The validity of the ZRS picture has been debated [147], but most workers agree that a split-off state is formed (as observed experimentally). As much of the debate revolves around the local spin character (singlet or doublet) this issue is considered not to be of relevance in the present context and therefore ignored. The split-off oxygen derived band hereafter is referred to charge transfer band

(CTB). The single-band Hubbard model, itself a low-energy approximation, can be further approximated at even lower energy scales. If one enforces a constraint of no double site occupation (the so-called Gutzwiller constraint) then the upper Hubbard band need not enter explicitly into the calculation. With the no-double-occupation constraint, electrons with oppositely aligned spins on neighboring sites can still lower their kinetic energy by undergoing virtual hopping to nearest-neighbor sites. First-order perturbation theory gives an energy lowering for oppositely directed spins

$$\Delta E_{\uparrow\downarrow} = \sum_j \frac{|\langle j|t_{ij}c_j^\dagger c_i|i\rangle|^2}{U} = -4\frac{t^2}{U} \tag{2.48}$$

Most of the following discussion will be in terms of the one band Hubbard model. It should be mentioned, that in the full three band model it is possible under similar considerations to derive a superexchange interaction given as

$$J_{se} = \frac{t_{pd}^4}{\Delta + U_{pd}^2}\left(\frac{1}{U_d} + \frac{2}{2\Delta + U_p}\right) \tag{2.49}$$

By Pauli principle considerations, an electron can not hop to a site already occupied by an electron of the same spin. This energy lowering can be subsumed into an effective spin interaction energy. U makes the material an insulator, but a remaining finite t makes it an antiferromagnet. In the limit where $t << U$ but is still finite for nearest neighbors, the effective Hamiltonian reduces to

$$H = \sum_{i.j} tc_i^\dagger c_j + \sum_{i,j} J\left(\mathbf{S_i}\cdot\mathbf{S_j} - \frac{\mathbf{1}}{\mathbf{4}}\mathbf{n_i}\cdot\mathbf{n_j}\right) \tag{2.50}$$

with the constraint on the Hilbert space of no double occupation. This $t-J$ model is valid for calculating low-energy properties. It can be generalized further (and made to closer match experiment), by adding next-nearest (t') and next-next-nearest neighbor hopping terms (t''). The general systematics of the difference between the photoemission spectra of hole- and electron-doped materials can be modeled successfully within a $t-J$ context [148]. However, a question regarding its validity remains. The effective parameter J was derived for the insulating case with localized electrons. Is J still a valid parameter when many holes or electrons have been introduced? This question has not been satisfactorily addressed in the literature. When $t' = 0$

and $t'' = 0$ the one band Hubbard Hamiltonian is particle-hole symmetric. This can be expressed formally as being invariant under the particle-hole transformative operation

$$c_{i\sigma}^{\dagger} \rightarrow (-1)^i c_{i\sigma} \tag{2.51}$$

When $t' \neq 0$ the above transformation to the Hamiltonian with $t' > 0$ can be mapped onto its particle-hole symmetric one, but with the sign of t' reversed. This means that the results obtained for negative sign of t' for dopings below half-filling can be obtained from the results for positive filling. In this way $t - J$ calculations that would represent the hole-doped case with a negative sign for t' can be made to represent the electron-doped case with a positive sign for t'.

There are many approximate solutions of the $t-J$ model, which surprisingly lead to many similar answers [149]. A question remains for the extremely simplified and effective $t - J$ model; Do solutions in the metallic regime give a Fermi liquid? Many workers have answered "no" to this question and have proposed the $t - J$ model naturally leads to a RVB-type 2D generalization of the 1D spin-charge separated Luttinger liquid. It could be argued that the $t-J$ model is the wrong starting point to model a Fermi liquid. In conventional Fermi liquid theory, one typically assumes that kinetic energy is the largest energy scale in the problem and perturbs the bare wavefunctions with an interaction energy $U_{kk'}$. In the $t - J$ model, we have started from localized states that are diagonal in the onsite interaction term U and perturbed them with the kinetic energy term t (Eq. 2.48). It is not obvious that a Fermi liquid can be recovered. Are cuprates Fermi liquids? - is a somewhat independent question, as there is no guarantee that the $t-J$ model describes the cuprates properly.

2.8 Scope

This first part of the thesis will attempt to address a number of issues brought up above, specifically those concerning electron-doped cuprates. The high-temperature superconductors are known to be doped Mott insulators [68]. The symmetry, or lack thereof, between doping with electrons (n-type) or holes (p-type) has important theoretical implications as most existing models implicitly assume symmetry. Most of what we know about these superconductors comes from experiments on p-type materials. The comparatively

fewer experiments on the n-types suggest that there is a substantial difference between these two sides of the phase diagram. Despite this, the issue of electron/hole symmetry has not been seriously discussed, perhaps because the existing database is rather limited. Although p-type materials are interesting in their distinctiveness, the major focus here will be to investigate the electron doped side and understand how or if their phenomenology fits into the somewhat established phenomenology of hole-doped compounds. In this context, one needs to address a number of questions; is the phase diagram symmetric? Does the close proximity of the highest T_c samples to the antiferromagnetic phase give us any insight into this enigmatic effect? How does the phase diagram behave if Nd is exchanged by smaller or larger cations? Being very complex systems, the high-temperature superconductors are represented by models that are highly simplified abstractions of actual materials. It is hoped that these models capture the essence of the essential physics. As pointed out above, most are electron/hole symmetric. In as much as this symmetry is a natural result of these models, one might doubt their suitability or completeness if it is found that the symmetry is experimentally broken. This then raises the question: Do the real materials obey this symmetry or is it only a result of simple models? The majority of experiments only considered the $Nd_{2-x}Ce_xCuO_4$ case and compared to $La_{2-x}Sr_xCuO_4$. Therefore, by aid of thin films, $La_{2-x}Ce_xCuO_4$, $Pr_{2-x}Ce_xCuO_4$, $Nd_{2-x}Ce_xCuO_4$, $Sm_{2-x}Ce_xCuO_4$, $Eu_{2-x}Ce_xCuO_4$ and $Gd_{2-x}Ce_xCuO_4$ will be studied in detail and compared in this thesis. Thin films have been investigated by electrical transport measurements, structural analysis, magnetic measurements using superconducting quantum interference device (SQUID) and low-energy muon spin rotation (LE-μSR).

3

Growth and characterization of electron doped cuprates

Molecular beam epitaxy (MBE) is a thin film growth technique relying on the evaporation of elements from individual sources in a ultra high vacuum environment. Its unique capabilities to control the growth of monolayer doses of several different elements in succession and with relative ease, are difficult to reproduce with other thin film deposition techniques such as sputtering, pulsed laser deposition (PLD), or chemical vapor deposition. These striking advantages have made it the technique of choice for the deposition of complex structures and even hetero-structures in a variety of crystal systems [150, 151]. In addition, unlike traditional single source sputtering and laser ablation, MBE does not require the fabrication of a target of the desired compound, instead, rely on evaporation from elemental material sources. Moreover, MBE technique allows the growth of many metastable compounds and structures that cannot be realized by bulk synthesis techniques. MBE has been successfully used for years for the deposition of a variety of conventional semiconducting materials and devices [152, 153, 154]. In particular, MBE is the primary tool used for the deposition of III-V semiconductors, such as GaAs and InP, employed in a variety of optoelectronic devices. Growth techniques utilizing the volatility of the group V elements (e.g., As and P) have been a key for the stoichiometric growth of these compounds but have limited the development of composition control technologies. In general, ion gauges, mass spectrometers, and reflection high energy electron diffraction (RHEED) are the common flux calibration tools utilized in III-V MBE machines.
In contrast, oxide MBE or reactive molecular beam epitaxy is an emerg-

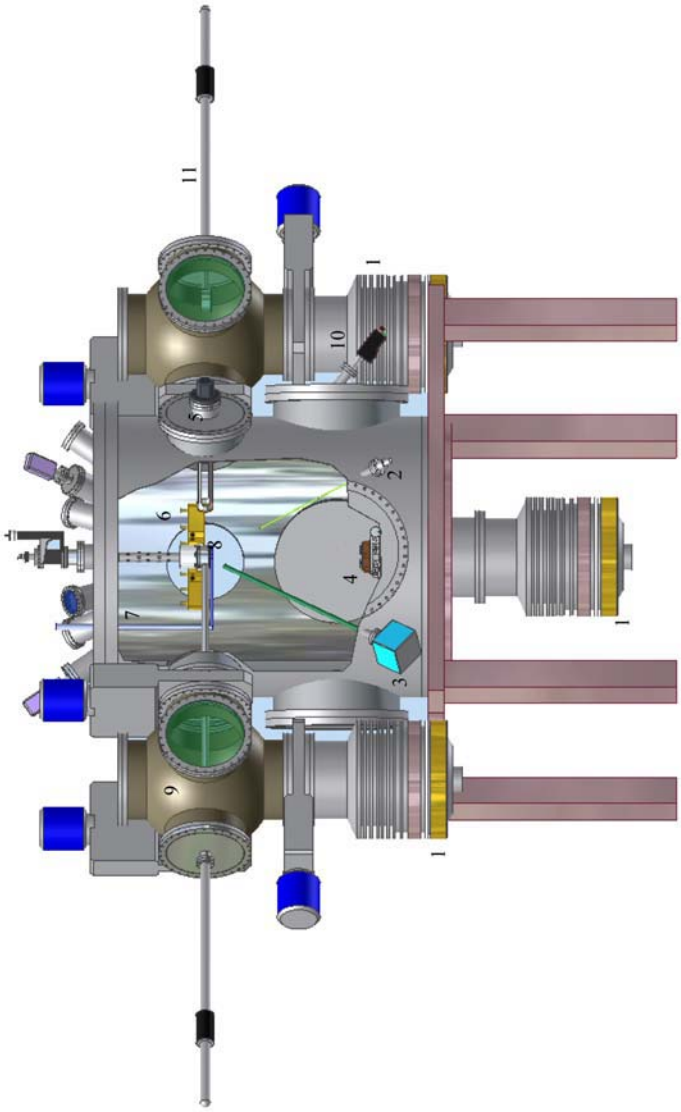

Fig. 3.1: Custom designed reactive molecular beam epitaxy chamber at NTT Basic Research Laboratories. (1) Turbo Molecular Pump, (2) ozone nozzle, (3) radical oxygen source, (4) electron-gun magazine, (5) RHEED screen, (6) EIES sensors (see also Fig. 3.4), (7) shutter, (8) rotating substrate heater, (9) load lock, (10) pyrometer, (11)*in situ* transfer for ARPES, XPS. .

ing field, initially used for the growth of layered perovskite superconductors [155] after the discovery of high-temperature superconductivity in oxides. The growth of multicomponent oxides[156, 157, 158, 159, 160, 161] by MBE

offered many unique challenges, with hardware compatibility in an oxidizing environment and precise composition control of the constituent elements a primary limitation. Deposition of many complex multicomponent oxides, contain two or more elements with little or no volatility, requiring precise flux control to ensure the stoichiometric deposition of the desired phase. The demands of oxide MBE [162] have led to the development of several real time *in situ* composition control techniques such as atomic absorption spectroscopy (AAS), electron impact emission spectroscopy (EIES), quartz crystal microbalances, and RHEED. Currently, composition control continues to be one of the primary limitations in the growth of complex oxide structures and high quality multicomponent oxide compounds by MBE. In this work, $RE_{2-x}Ce_xCuO_4$ films were grown by electron beam coevaporation from metal sources in a custom designed UHV chamber Fig. 3.1. The main feature of this MBE system is the precise control of evaporation flux: A feedback system, which uses electron impact emission spectrometry sensors for evaporation flux measurements, controls the evaporation flux of RE = La, Pr, Nd, Sm, Eu, Gd, Ce, Tb, Y, Lu and Cu, within high accuracy (e.g., Cu can be controlled with $\sim 10^{-3}$ Å/s). The growth rate is such that it takes ≈ 7.2 s for the formation of one unit cell. The films are oxidized by ozone gas ($\sim 10\,\%$)O_3 concentration generated with a commercially available ozone generator, which is introduced in the chamber through a single alumina tube directed at the substrate position. The oxidation condition during growth can be adjusted by changing the amount of gas introduced in the chamber and/or the nozzle to substrate distance. The growth temperature, T_s, ranged from 540 to 760 °C.
The technical details of EIES, RHEED and inductively coupled plasma analysis (ICP) are given in the following paragraphs. Moreover, thermodynamical aspects on the stabilization of T′- or Nd_2CuO_4-structured cuprates in thin film form are also described in detail.

3.1 Electron impact emission spectroscopy

The exigencies on composition control in reactive molecular beam epitaxy are quite high, since evaporation takes place in an ozone or radical oxygen environment. Since three metals, e. g., lanthanum, cerium and copper, are evaporated simultaneously, element specific rate monitoring plays a vital role in growing high quality $La_{2-x}Ce_xCuO_4$ thin films. The devel-

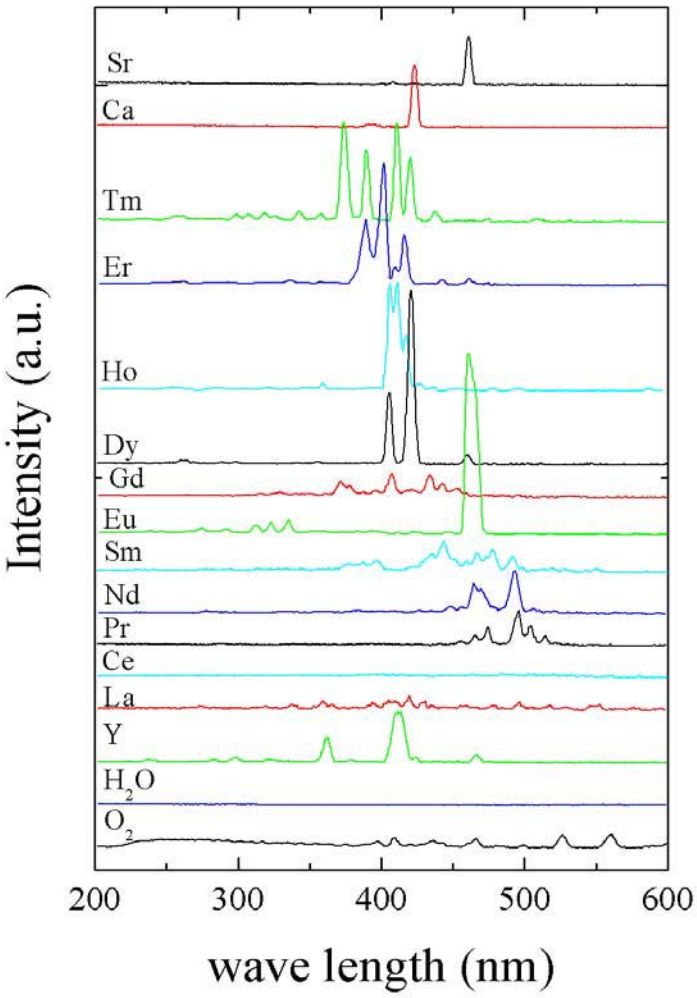

Fig. 3.2: Measured EIES-spectra of several elements (including water) used for thin film synthesis (part 1, for part 2 see Fig. 3.3 on page 58).

opment of electron impact emission spectroscopy started in the early 80's [163, 164, 165, 166, 167, 168]. Although the initial task was deposition of alloys or multilayers, the technique of EIES was adapted and upgraded by M. Naito to be used in a reactive environment.

3.1.1 Principles of EIES measurements

Electron Impact Emission Spectroscopy uses a thermionic emitter to generate free electrons, accelerated across a window (through which the evaporants pass through) by applying an accelerating potential. When these electrons impinge the evaporant atoms passing through the window, they excite outer shell electrons to a higher energy level. When these excited electrons return to their normal state, they emit photons of a characteristic wavelength(s). These characteristic wavelength(s) can be utilized for element specific monitoring. Use of optical filters allows one to select the desired wavelength corresponding to a specific element (see Fig. 3.2 and 3.3) which is then passed to a photomultiplier tube (PMT) detector and the output is used for the monitoring and feedback control of the corresponding evaporation sources. The intensity of the characteristic wavelength is proportional to the rate of deposition of the selected material.

Sensor

The EIES emitter assembly (referred to as the sensor for historical reasons) consists of a hot cathode filament used to emit high-energy electrons. The sensor is installed, so that a portion of the evaporant stream passes through the active sensor region. Within the sensor housing, electrons from the filament strike the evaporant atoms, raising the energy level of the outer electrons. These excited electrons immediately return to their normal energy level, emitting photons. The wavelength of the photons is characteristic of the material, and the intensity is proportional to the number density of the atoms. For any material

$$J \propto i \cdot N \tag{3.1}$$

where J is the emission intensity, i the electron beam current and N the number density of atoms. Hence,

$$D = m \cdot v \cdot N \tag{3.2}$$

where D is the mass deposition rate, m the mass of atoms and v the average velocity of the evaporated atoms. For a constant evaporation velocity this leads to

$$J = k \cdot D, \tag{3.3}$$

where k is a calibration constant. The calibration constant incorporates several reasonable assumptions inherent in the above derivation - constant

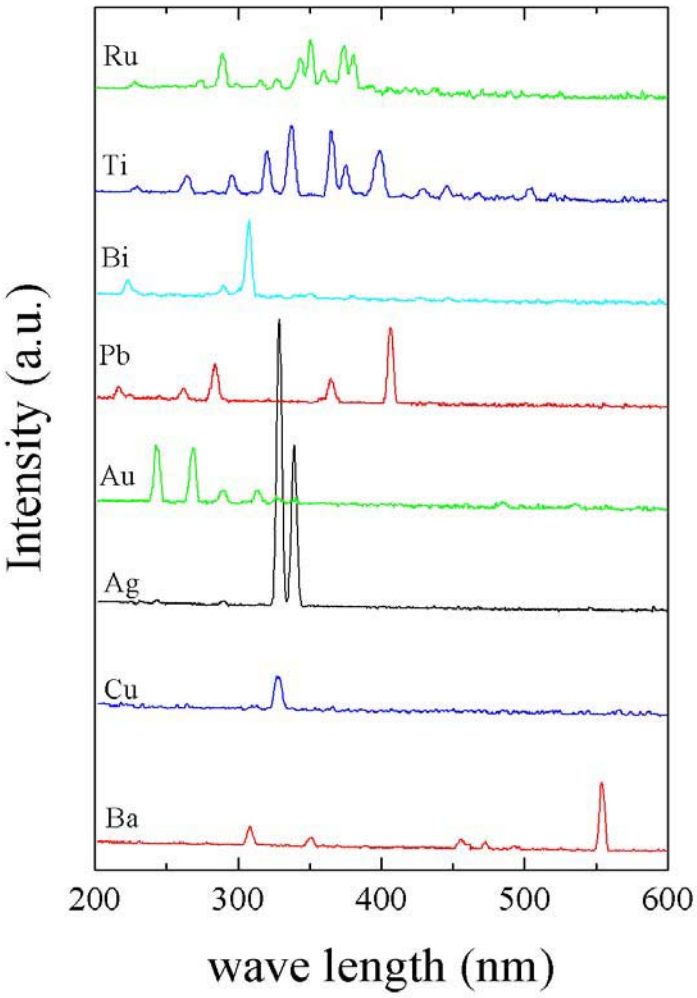

Fig. 3.3: Measured EIES-spectra of several elements used for thin film synthesis (part 2).

velocity, constant source temperature, and optical losses. The emitted light must be efficiently transmitted to the detection devices. For short, straight transmission paths from the sensor to the detectors the sensors hollow tube may be adequate. However, the number of photons reaching the detector is proportional to the inverse of the light path squared ($1/D^2$).

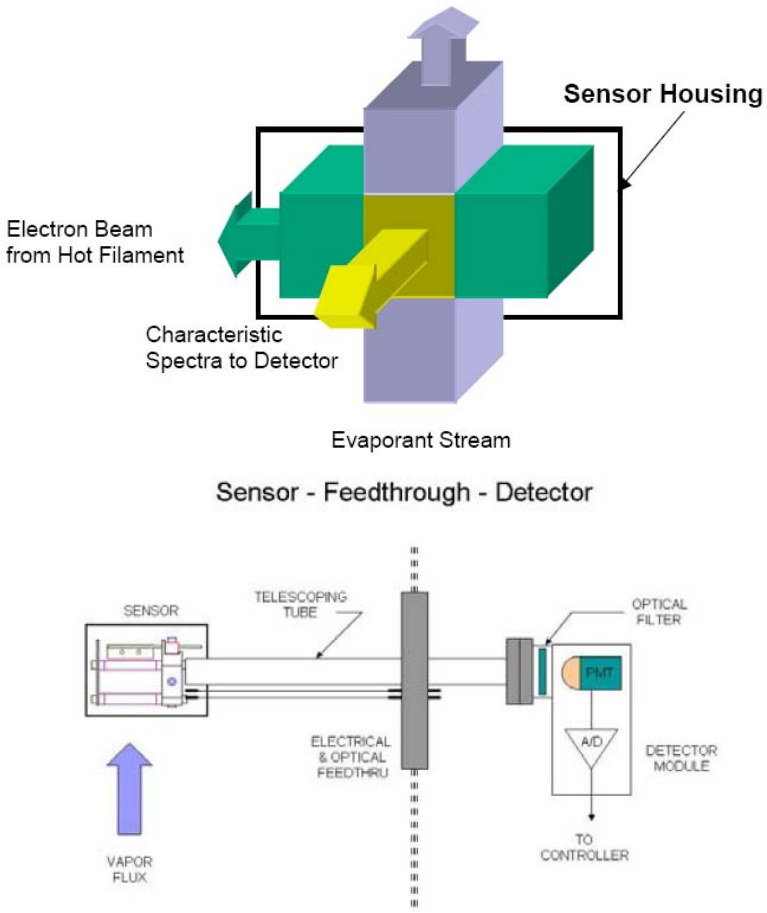

Fig. 3.4: Schematic representation of an EIES sensor head.

3.2 Reflection-High Energy Electron Diffraction

RHEED is one of the most common real time, *in situ* analysis techniques utilized during MBE growth. Typical RHEED geometry involves a beam of high energy (10 - 40 keV) electrons striking the surface of the sample at a grazing angle of incidence ($< 1°$) and the diffracted beam is detected on a phosphorous screen. Because of the shallow angle of incidence, the penetration depth of the electrons is small and RHEED is extremely surface sensitive providing information on the top few mono layers of the deposited film. In addition, the small angle of incidence allows for the monitoring of highly insulating oxide materials without the common charging problems associated with normal incidence electron probe techniques, such as low energy

electron diffraction (LEED). Extensive information on the characteristics of the surface of a film can be obtained from a RHEED image including its crystallinity, roughness, in-plane lattice constant, and phase purity. In addition, analysis of the RHEED intensity oscillations during the growth of a film can be used for composition control and flux calibration [169, 170]. Several different RHEED techniques have been employed for MBE composition control. RHEED oscillations are routinely used to measure the film growth rate during the deposition of either single component materials or two-component materials with a volatile constituent. In multi-component systems with two or more non-volatile constituents adjusting the ratio of incident fluxes in response to the appearance of identifiable impurity phase spots in the RHEED pattern has been successfully used for composition control. In addition, RHEED oscillations have been used during the deposition of the binary oxides, and the co-deposition of multi-component oxides to determine when a full monolayer coverage has been obtained. Prior to the work in this thesis, however, there has been few report of the use of the RHEED pattern for the phase control of multi-component oxides.
The technology of RHEED is widely used. Therefore, we will not go into details but refer to a real comprehensive book by A. Ichimiya [171], where all details about the theory of the RHEED patterns, growth analysis, spots, etc., can be found. However, it is useful to recall the basic physics of RHEED.

Experimental setup

Figure 3.6 is a drawing showing the typical design for a Reflection High Energy Electron Diffraction experiment. A compact beam of 40 keV electrons is glanced across a surface at grazing incident angle. The diffraction pattern that is formed at the phosphor screen reflects the surface atomic arrangement because the component of the electron momentum normal to the surface is very small, and there is a correspondingly small electron penetration depth into the surface. RHEED is the ideal technique for studying real-time changes in a surface unit mesh during deposition or desorption of adsorbates, because the system geometry is such that the electron beam and the phosphor screen do not interfere with MBE and are not adversely affected by typical experimental processes. At the phosphor screen a typical RHEED image will consist of bright streaks and spots against a diffuse background. An example is shown in Fig. 3.5, where the image was obtained by

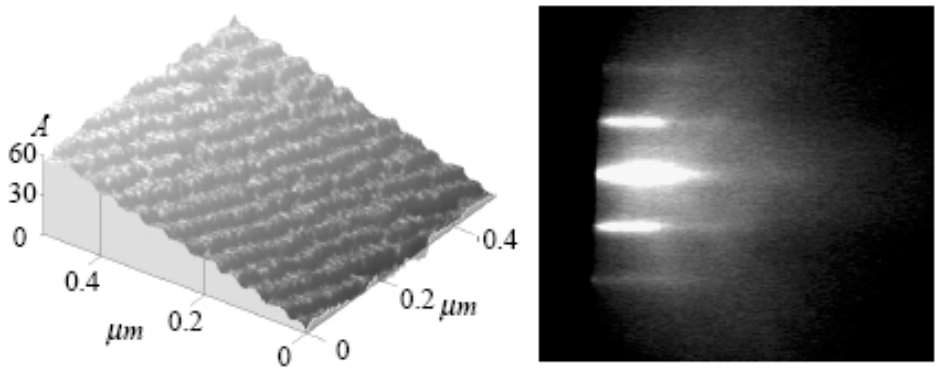

Fig. 3.5: An AFM image taken of a cleaned, chemically etched and oxygen annealed $SrTiO_3$ substrate (left picture) and the corresponding RHEED picture under deposition conditions. In this RHEED pattern sharp streaks corresponding to the $(2;0)$, $(0;0)$ and $(\overline{2};0)$ reciprocal lattice rods are clearly visible, together with Kikuchi lines.

diffraction of 40 keV electrons from the clean $SrTiO_3$ surface along the (100) direction. The arrangement of these bright spots on the screen is related to the arrangement of atoms at the surface. Knowing the connection between the two is like having a window through which to observe the atomic-scale world at the surface of a solid.

Origins of electron diffraction

The physical origin of the pattern of bright spots on the screen can be understood by the theory of elastic scattering of waves as it applies to the wavefunctions describing energetic electrons. Recall that electrons are expected to scatter from a crystal substrate in response to the spatial distribution of electrons within each unit cell of the crystal. The electron distributions are centered on the atoms of the crystal and thus have the same periodicity as the atoms in the basis. To eventually measure scattering from a periodic array of atoms we will be interested, then, in a periodic function known as the electron number density. Since this electron number density, say $n(r)$, is a periodic function, the situation is ideal for Fourier analysis. Accordingly, $n(r)$ can be represented as the infinite sum,

$$n(r) = \sum_g n_g \cdot e^{iG \cdot r} \tag{3.4}$$

In the process of finding the set of vectors G that leave $n(r)$ unchanged under any crystal translation that leaves the crystal invariant, we arrive at the reciprocal lattice vectors, $b1$, $b2$, $b3$ given by,

$$b_i \cdot a_j = 2\pi\delta_{ij} \tag{3.5}$$

where a_j are the real space primitive vectors of the associated crystal lattice. We speak of the reciprocal lattice of a given real space lattice, where the reciprocal lattice is mapped out by the set of vectors,

$$G = v_1 b_1 + v_2 b_2 + v_3 b_3 \tag{3.6}$$

and we refer to G as a reciprocal lattice vector. Armed with this definition of $n(r)$, we are ready to handle an electron scattering event where an electron beam is incident on a crystal for which $n(r)$ describes the periodic distribution of electrons. Fig. 3.7 shows an electron beam represented as $\exp(ik \cdot r)$, where k is the wavenumber of the incoming beam, being scattered by a crystal substrate. According to the theory of elastic scattering of waves, the

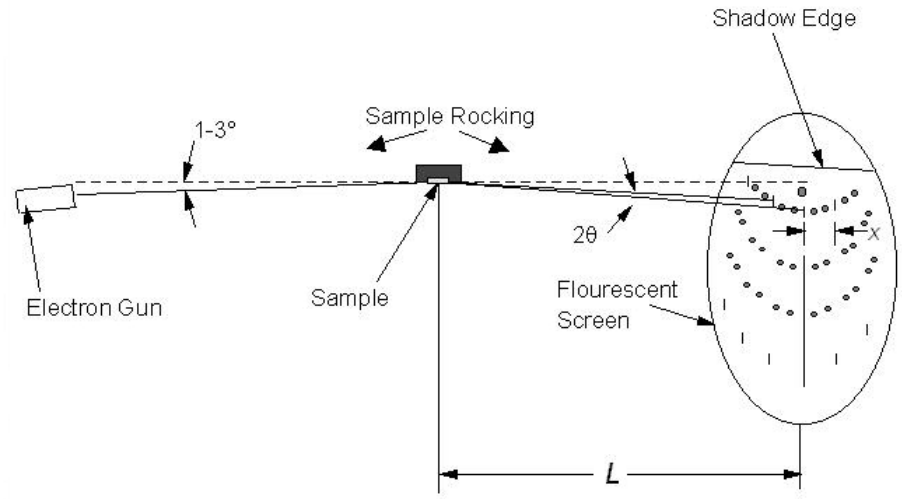

Fig. 3.6: Schematic depicting the RHEED technique. Since MBE hardware is usually positioned below the sample, the technique is ideal for observing real-time changes in surface periodicity during deposition of adsorbate atoms onto the surface.

amplitude of a scattered wave will be proportional to the electron number density, $n(r)$, in the region of the scattering. Figure 3.8 shows the difference

in phase factors ($\exp[i(k-k')\cdot r]$) in the direction of k'. The total amplitude, F, of the scattered wave in the direction of k' is obtained by integrating over the whole crystal the contributions of the scattering due to $n(r)$ at the infinitesimal volume elements dV, and adjusted by the phase factor:

$$F = \int dV n(r) e^{i(k-k')\cdot r} \tag{3.7}$$

After introducing the Fourier components of $n(r)$ given by Equation 3.4 and defining a scattering vector, Δk, as the vector representing the difference between the incoming and outgoing wavevectors,

$$k + \Delta k = k' \tag{3.8}$$

one gets

$$F = \sum_g \int dV n_g \cdot e^{i(G-\Delta k)\cdot r} \tag{3.9}$$

Notice that the maximum value for scattering amplitude will be obtained when

$$\Delta k = G \tag{3.10}$$

and the argument of the exponential is zero. This intensity can be shown to fall off rapidly for $\Delta k \neq G$. Thus we have found the diffraction condition, $\Delta k = G$, that is responsible for the bright spots that appear on the phosphor screen in the RHEED experiment. This condition can be shown to be equivalent to Braggs law for constructive interference of reflected radiation from successive lattice planes. Ultimately, the constructive interference that causes bright spots at the phosphor screen is due to the arrangement of points in the reciprocal lattice. The location of these diffraction maxima in space (i.e., at the phosphor screen) leads to a deduction of the form of the reciprocal lattice, and subsequently to the form of the real space lattice by virtue of equations 3.5.

The Ewald sphere construction

A useful graphical representation of the conditions for diffraction is provided by the Ewald Sphere construction. A 2D representation is shown in Fig. 3.8, where the vector k is drawn to terminate at the origin of a reciprocal lattice (a square lattice in this case). Now a sphere of radius k is drawn whose center, P , is the origin of the vector k. Where the sphere passes through

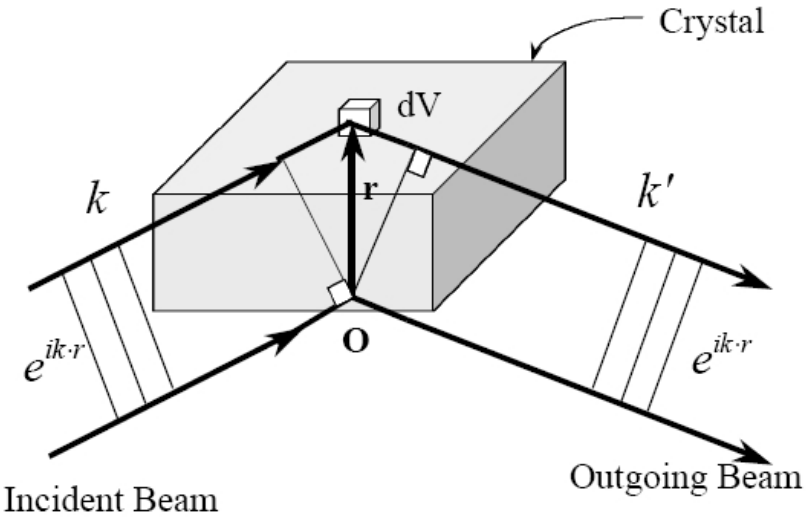

Fig. 3.7: The difference in path length of the incident wave k at the points 0 and r is $r \cdot \sin\theta$, and the difference in phase angle is $\frac{2\pi r}{\lambda} \sin\theta$, which is equal to $k \cdot r$. For the diffracted wave the difference in phase angle is $-k' \cdot r$. The total difference in phase angle is $(k - k') \cdot r$, and the wave scattered from dV at r has the phase factor $e^{i(k-k')} \cdot r$ relative to the wave scattered from a volume element at the origin 0.

a reciprocal lattice point, a line to this point from the center of the sphere represents a diffracted beam of wavevector k'. The vector connecting the two is then a reciprocal lattice vector G. By varying either the energy, i.e., the length of the incoming wavevector, of the incident beam, or the orientation of the crystal relative to the beam, all reciprocal lattice points may be mapped. In surface physics, we are most interested in the 2-dimensional arrangement of atoms that forms the boundary between the bulk crystalline structure and the ambient environment. The reciprocal lattice of a 2-dimensional array is no longer a set of points, but rather a set of infinitely long rods extending normal to the surface and having the periodicity of the surface unit mesh. To understand this, consider that distances in reciprocal space are inversely proportional to distances in real space. Therefore if points move farther apart in real space, the associated reciprocal space points move closer together. In the direction normal to a crystal surface, the real-space spacing of atoms is removed to infinity, so the reciprocal lattice points are packed infinitely close together to form continuous rods normal to the atoms forming the surface reciprocal mesh. This relaxing of the diffraction conditions means

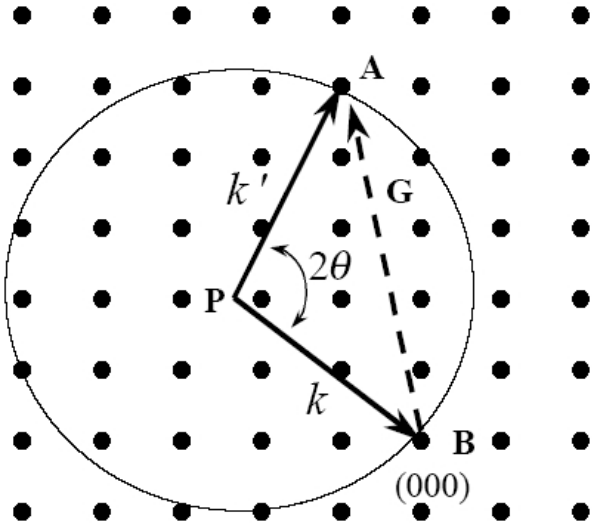

Fig. 3.8: The Ewald Sphere Construction. The wavevector k of the incident wave is drawn to terminate at the origin of reciprocal space. A sphere drawn with radius k and with center P is the Ewald Sphere. If a point on the reciprocal lattice lies on the surface of the Ewald Sphere, the condition for elastic scattering is satisfied and diffraction will occur with the scattered beam having wavevector k'. The vector G connecting k and k' is a reciprocal lattice vector. Note, for arbitrary k there will be few instances where the conditions for diffraction are satisfied.

that a diffraction pattern can be observed at all energies and in any geometry, as is shown in Fig. 3.9. Notice that the conditions for diffraction occur at the intersection of the Ewald Sphere with reciprocal lattice rods, and consequentially first order diffraction results in bright spots occurring along arcs at the phosphor screen. According to the Bragg relation for first order diffraction, where

$$2d \sin\theta = n \cdot \lambda \tag{3.11}$$

we can find the real space separation between atoms corresponding to the reciprocal lattice spacing. Recall that the energy of the plane wave with wave vector k is given by $E = h^2k^2/2m$. Using the fact that $k^2 = 2\pi/\lambda$ we can write $\lambda = \sqrt{h/2mE}$, and this is a known quantity for the 40 keV electrons. The angle formed between the sample and two adjacent spots is 2θ, as in Fig. 3.8. By geometry $\tan 2\theta = t/L$, where t is the separation between spots and L is the distance between the sample and the screen. Since L is long compared with t, $\tan 2\theta \approx 2\theta$ and $\theta \approx t/2L$. Substituting these into the

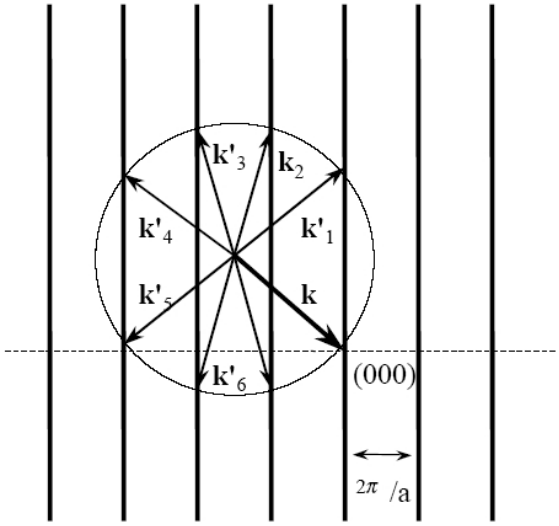

Fig. 3.9: The 2D Ewald Sphere construction for diffraction from a square net of surface atoms of side a. Notice that because the diffraction conditions have been relaxed by the 2D arrangement at the surface, and reciprocal lattice points have become elongated rods normal to the surface, diffraction maxima will be observed for any sample orientation and almost any beam energy.

Bragg relation gives

$$t = \lambda \cdot L/d \tag{3.12}$$

This simple equation is a relation between the measurement t obtained as the distance between spots at the phosphor screen and the reciprocal space distance d for the given diffraction geometry. In principle, Equation 3.12 can be used to determine the reciprocal lattice separation giving rise to the adjacent spots in the first Laue Zone (the zone of diffraction spots closest to the shadow edge on the phosphor screen). The inverse of this separation is the associated real space separation along the crystal direction defined by the two adjacent spots.

3.2.1 RHEED patterns of K_2NiF_4 and Nd_2CuO_4 structured compounds

Let us now have a closer look to the advantages of RHEED for the growth of Nd_2CuO_4-structured compounds. Although the EIES-setup enables sufficient stable and stoichiometric fluxes, RHEED allows the real-time monitoring of what happens at the substrate. The kinetics of phase formation plays a cru-

cial role. At first, we consider the optimal case, where the stoichiometric

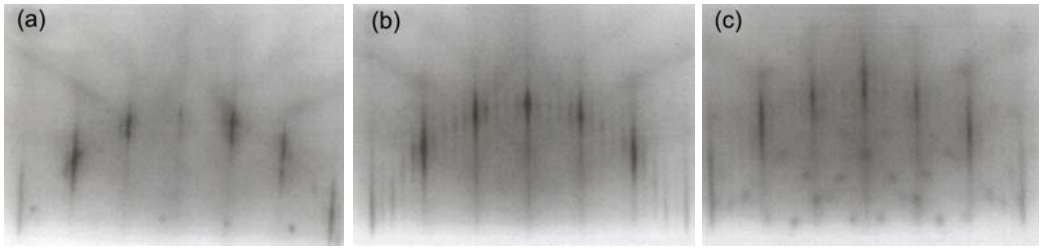

Fig. 3.10: RHEED patterns of T-structured La_2CuO_4, where the copper flux is (a) too poor, (b) stoichiometric and (c) too high. The pictures have been taken during the attempts to synthesize T′-structured $La_{2-x}Tb_xCuO_4$ (see Chapter 6).

adjustments of the lanthanum, terbium and copper- fluxes are ideal. For the T-structure, this is shown in the center pattern of Fig. 3.10. One can clearly observe the main streaks as well as four super-structure streaks. The streakiness, checked at different angles of the incidence beam, suggests that the patterns are dominated by reflection rather than transmission indicating reasonably smooth film surfaces. The Kikuchi lines are still visible for these samples, suggesting also a long range ordering. These Kikuchi lines are three dimensional features which originate from electrons which have suffered inelastic collisions in the bulk before they are finally Bragg diffracted by a lattice plane. However, when the copper-stoichiometry is off, the RHEED pattern drastically changes. Such situations are plotted in Fig. 3.10 (left pattern) for the copper-poor case and for the copper-rich case in the right pattern of Fig. 3.10. Although the main-streaks are still visible, additional spots occur. These additional spots correspond to products other than 214 phase. In a similar way, the T′-phase can be monitored. Figure 3.11(a) shows the RHEED pattern of a copper-poor flux case. Again, additional spots (impurity phases) occur in contrast to the stoichiometric adjustment of the copper-flux (Fig. 3.11(b)).
Moreover, the above mentioned sensitivity of RHEED allows one to precisely determine the phase stabilities of the grown materials. As will be described in Chapter 4 electron doped cuprates have to be subjected to an annealing process in vacuum after the synthesis. The annealing process is required in order to remove apical oxygen, which has been incorporated to the structure during its growth. While for bulk material Argon flow at temperatures around 900 °C is used, thin films are treated in an ultra high vacuum at-

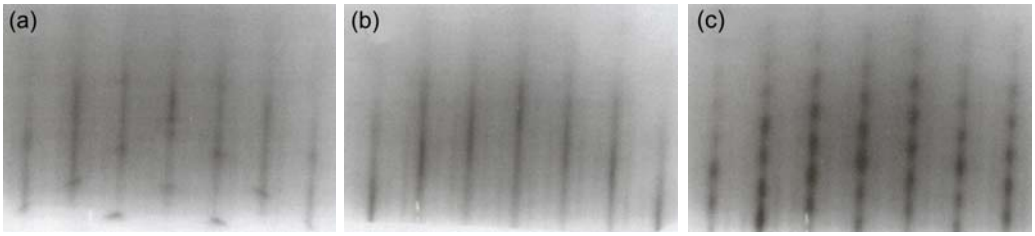

Fig. 3.11: RHEED patterns of T′-structured $La_{2-x}Tb_xCuO_4$, where the copper flux is (a) too poor, (b) stoichiometric and (c) too high. The pictures have been taken during the attempts to synthesize T′-structured $La_{2-x}Tb_xCuO_4$ (see Chapter 6).

mosphere. The removal of apical oxygen is a diffusive process and therefore dependent on time, temperature, sample size and environmental atmosphere. It is therefore crucial to determine appropriate reduction conditions for this reduction treatment in order to avoid decomposition of the T′-phase. In this context, RHEED is a vital tool since it is surface sensitive. This means, if the surface (the first unit cells) start to decompose and therefore other phases are stabilized, by aid of RHEED one can observe these boundaries in real-time. For example, in the case of $Nd_{2-x}Ce_xCuO_4$, the typical decomposition products are $(Nd,Ce)_2O_3$, $NdCuO_{2.5}$ and/or Cu_2O [172, 173, 174, 175]. In the case of europium, also $CuEu_2O_4$ is a possible product [176]. Since all of them have completely different crystal structures, epitaxial growth is unlikely. Since the crystal structure differs from that of the 214 phase, different RHEED patterns appear. By applying this method the phase stability of several T′-structured compounds has been determined and the results are plotted in Fig. 3.14.

3.3 Inductively coupled plasma analysis (ICP)

Inductively Coupled Plasma Mass Spectrometry (ICP-MS) is a very powerful tool for trace (ppb-ppm) and ultra-trace (ppq-ppb) elemental analysis [177, 178, 179]. ICP-MS is rapidly becoming the technique of choice in many analytical laboratories for the accurate and precise measurements needed for todays demanding applications. In ICP-MS, a plasma or gas consisting of ions, electrons and neutral particles is formed from Argon gas (Fig. 3.12). The plasma is used to atomize and ionize the elements in a sample. The resulting ions are then passed through a series of apertures (cones) into the

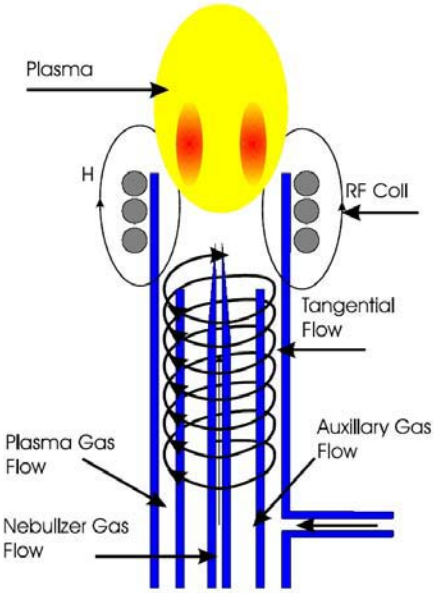

Fig. 3.12: Scheme of an ICP torch. A circular quartz tube (12-30 mm OD) has three separate gas inlets. The only gas routinely used is argon. The gas enters the plasma through the outer channel with a tangential flow pattern at a rate of 8-20 Lmin^{-1}. The auxiliary gas, which travels up the center channel, also has a tangential flow (0.5-3 Lmin^{-1}) pattern. The nebulizer gas has a laminar flow pattern (0.1 to 1.0 Lmin^{-1}) and injects the sample into the plasma. The analytical zone is approximately 1 cm above the coils and offers the best optical viewing area for maximum sensitivity. The plasma temperature in the analytical zone ranges from 5000-8000 K (the temperature varies with power, flow rate, etc.). The high temperature assures that most samples are completely atomized, although some molecular species (e.g., N_2, N_2^+, OH, C_2, etc.) do exist and can be readily measured in the plasma.

high vacuum mass analyzer. The isotopes of the elements are identified by their mass-to-charge ratio (m/e) and the intensity of a specific peak in the mass spectrum is proportional to the amount of that isotope (element) in the original sample. The inductively-coupled plasma is a very aggressive ion source. Because the source operates at temperatures of 7000 K, virtually all molecules in a sample are broken up into their component atoms. In ICP, a radio frequency (RF) signal is fed into a tightly wound, water-cooled coil where it generates an intense magnetic field. In the center of this coil is a specially made glass or quartz plasma torch where the plasma is formed. The plasma is generated in the argon gas by "seeding" the argon with a spark from a Tesla unit (similar to that used on a car spark plug). When

the spark passes through the argon gas, some of the argon atoms are ionized and the resultant cations and electrons are accelerated toward the magnetic field of the RF coil. Through a series of inelastic collisions between the charged particles (Ar^+ and electrons) and neutral argon atoms, a stable high temperature plasma is generated. The concentrations of electrons, Ar^+ and neutral species in the plasma very quickly reach equilibrium, after which the plasma will remain 'lit' as long as the RF field is maintained and there is a constant supply of argon gas into the plasma. The plasma torch is designed in such a way as to allow a sample to be injected directly into the heart of the plasma. The sample consists of a fine aerosol, which can come from any number of sources including, but not limited to, nebulized liquids and ablated solids. As the sample aerosol passes through the plasma, it collides with free electrons, argon cations and neutral argon atoms. The result is that any molecules initially present in the aerosol are quickly and completely broken down to charged atoms. These are usually in the M^+ state although a few M^{++} are also formed. Some of these charged atoms will recombine with other species in the plasma to create both stable and meta-stable molecular species (e.g., MAr^+, M_2^+, MO^+, etc.). Many of these molecular species will be positively charged and will also be transmitted into the mass analyzer along with the charged atoms (M^+ and M^{++}). The emitted light characteristics of each element is then used for the elemental specific weight measurements.
Although we have used EIES to control the beam flux, an independent way to measure the final stoichiometry of the grown samples is necessary. For each series of $RE_{2-x}Ce_xCuO_4$ three samples were measured by ICP analysis to calibrate the real cerium concentration. Moreover, ICP-analysis is also a powerful tool to measure the full cation stoichiometry. As it was discussed in Section 3.2.1, the RHEED pattern was said to be copper poor or copper rich. This evaluation is supported by ICP analysis.
Since the thin films are grown on oxide substrates like $SrTiO_3$, always some substrate material is dissolved and nebulized. Therefore, the determination of oxygen content in thin films is not possible [180].

3.4 Thermodynamics and phase stability

Soon after the discovery of high-T_c superconductors, it became more clear, that the complexities of chemistry of these oxides plays a vital role for their synthesis. However, as the complexity of the composition for oxide super-

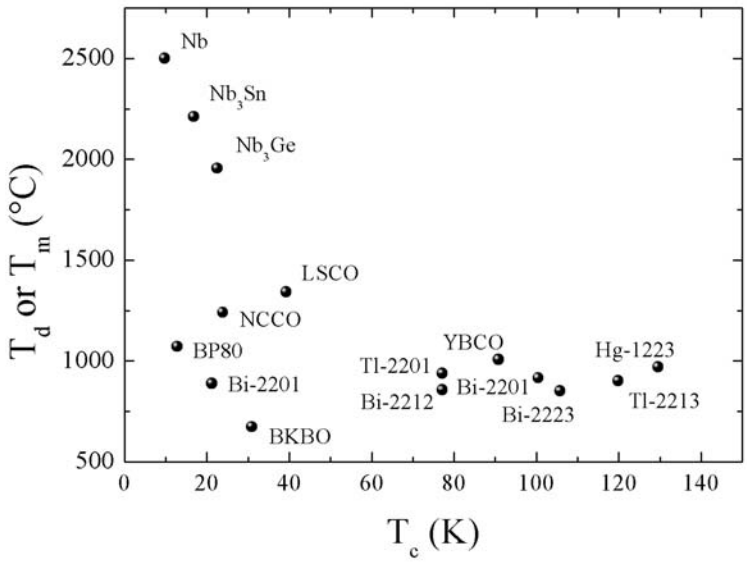

Fig. 3.13: Superconducting transition temperature (T_c) and decomposition (T_d) or melting temperature (T_m) of conventional and layered cuprate superconductors.

conductors increased, they exhibited less and less stability. Nearly all of the high T_c oxide compounds decompose before melting (incongruent melting). Figure 3.13 shows the dependence of decomposition temperature (T_d) or melting temperature (T_m) for the cuprate superconductors with layer structure compared with superconducting metals or intermetallic A15 alloys with three dimensional chain structure. Thermal and chemical stabilities of oxide superconductors are much poorer than A15 alloys. For the same family, the decomposition temperature or stable range of the superconducting phase reduces as T_c increases, which brings more difficulty to the material preparation and fabrication. Now we are facing two challenging strategies - to improve present compounds and to find new ones. The knowledge of phase diagram is fundamental data to understand, to control and to improve the material stability. Phase diagrams also provides basic information to starting the preparation of new type of materials.

The phase diagram shows the relation between phases, components under various conditions (temperature, pressure and electric field etc.) at a state

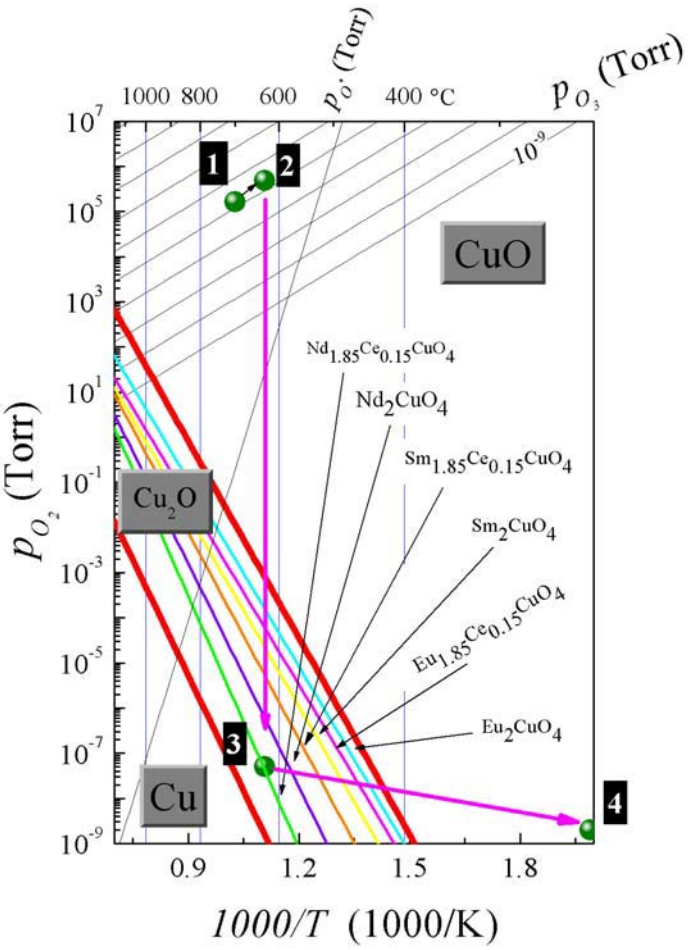

Fig. 3.14: Thermodynamic phase stability diagram for electron doped cuprates. Stability lines for CuO and Cu_2O have been calculated using the commercially available program MALT2®. Additionally, the equilibria oxidizing potential lines for ozone and oxygen are calculated. The ozone oxidation equilibria lines have an interval of $\log(p_{O_3}) = -1$. Additionally, the equilibrium oxidation potential line for radical oxygen is plotted for $p_{O^\star} = 10^{-9}$ Torr. The typical growth conditions encountered are indicated by points 1, 2, 3 and 4. Point 1 represents the condition, were the film growth take place (e.g., 700 °C, $2 \cdot 10^{-6}$ Torr O_3). The sample is subsequently cooled at constant ozone pressure to point 2. Then, ozone supply is stopped and therefore the pressure drops to point 3. After annealing the sample is cooled down to room temperature to point 4. The border lines for the different copper valency are indicated by thick red colored lines and the stability lines for the T′-structure compounds lie between them.

of thermodynamical equilibration. At thermodynamical equilibration, a system does not change, which includes: (a) The temperature does not change - thermal equilibration; (b) The pressure or the extra force does not change – mechanical equilibration and (c) The chemical potential of any component in all the phases is the same - chemical equilibration.

A phase is a homogeneous body with the same composition, structure and

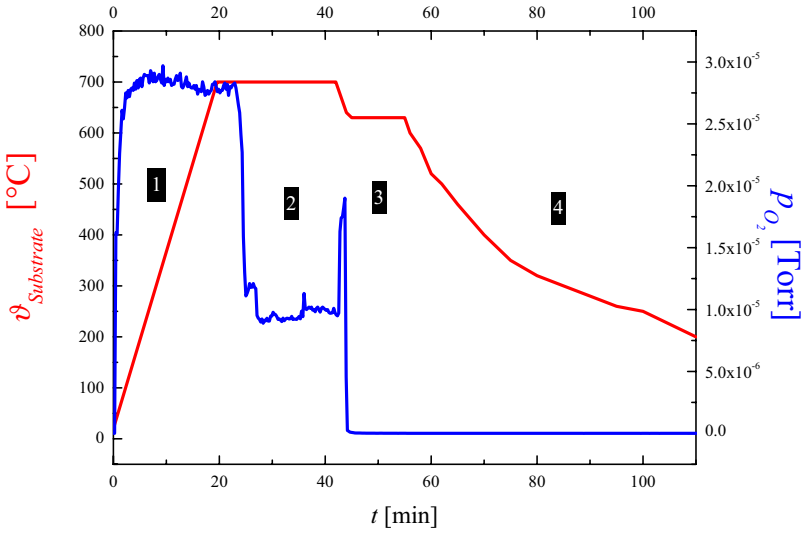

Fig. 3.15: Typical progression of substrate temperature (red line) and oxygen partial pressure (blue line) during growth of $RE_{2-x}Ce_xCuO_4$ thin films. The indicated numbers correspond to those in Fig. 3.14.

properties. Different adjacent phase are distinguished by a boundary where the chemical and physical properties change discontinuously. A system may contain one or more phases, consisting of various elements or compound compositions. The independently changeable composition is called a component. The main element compositions for the compounds are located at several groups in the periodic table, which decides the characters of the high T_c oxide superconductors and its relative phase diagram. The chemical properties of the elements in each group are similar, which decides some common nature of the oxide superconducting phase and their phase relation as well.

3.4.1 Phase diagrams and growth process of T′-phase compounds

The basis for controlling the growth and the reduction process for 214 cuprates is the copper-oxygen phase diagram as shown in Fig. 3.14. Such

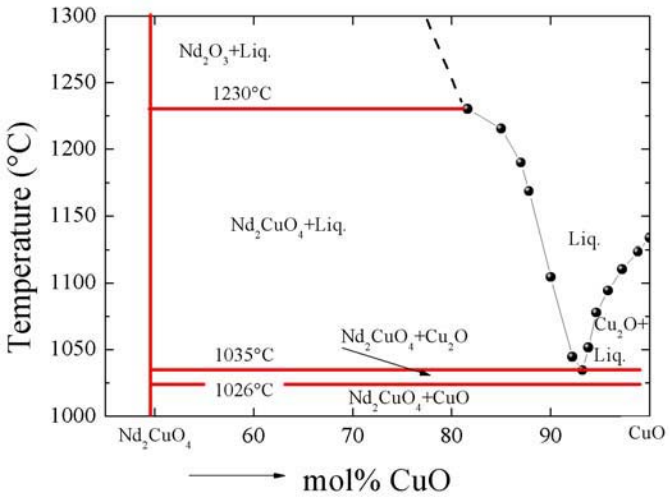

Fig. 3.16: Ternary phase diagram for Nd_2CuO_4 used for bulk synthesis. With increasing amount of CuO, the eutectic temperature decreases up to 93% CuO excess. Adapted from [181].

phase diagrams are successfully used and applied in the synthesis of superconducting transition oxide materials [182]. In the case of bulk synthesis, the oxygen partial pressure usually is constant. A typical phase diagram for Nd_2CuO_4 synthesis is shown in Fig. 3.16; these phase diagrams slightly deviate for different rare earth elements [183]. The valency of copper is determined by the oxidizing potential (or equipotential oxygen partial pressure) and temperature. Between the two thick red lines in Fig. 3.14, copper is monovalent. Typical growth conditions encountered are indicated by points 1, 2, 3 and 4. Point 1 very much depends on the rare earth ion in $RE_{2-x}Ce_xCuO_4$ and the doping level x. The dependence of the growth and annealing conditions are plotted for RE = Pr in Fig. 3.4.1 as a typical example. From the phase-diagram (Fig. 3.14) one can clearly see that the growth is performed far away from the Cu_2O-CuO equilibrium line. Such conditions can only be achieved by using a strong oxidizing agent like ozone (It is worth-

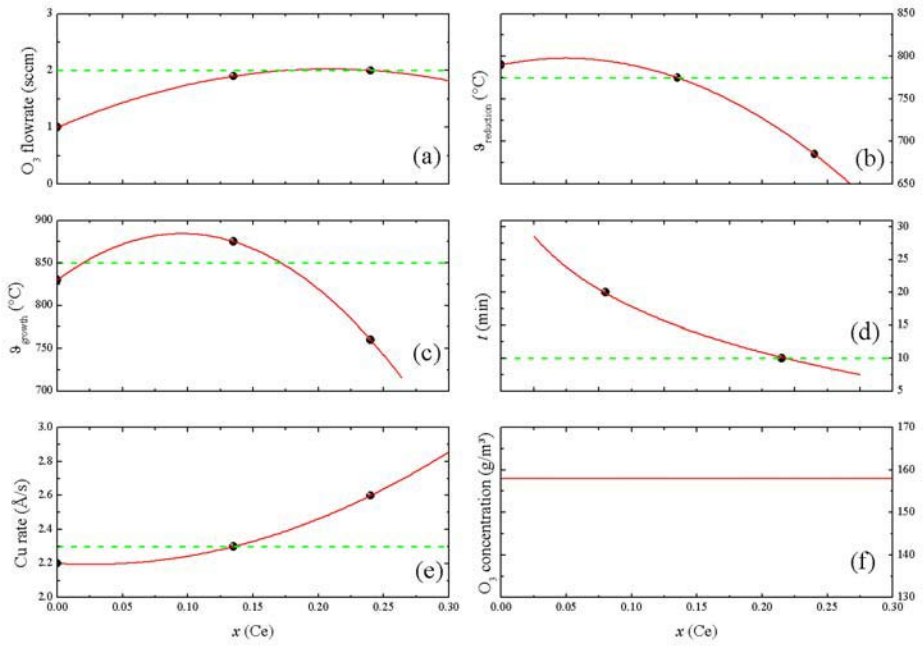

Fig. 3.17: Growth parameters for thin films of $Pr_{2-x}Ce_xCuO_4$ versus cerium doping concentration. In (a), the ozone flow rate has been increased for increasing cerium concentration. Plot (b) shows the reduction temperature dependency used for thin film growth. The reduction temperature has been decreased upon doping. Fig. (c) maps the optimized growth temperature trend. For films with optimal doping level, the growth temperature was highest. The variation of reduction time with cerium concentration is plotted in Fig. (d). Optimization of the parameters indicate an increasing reduction time for decreasing cerium contents. While the ozone flow rate has been increased, subsequently copper was augmented (e). For all runs the ozone concentration was kept constant (f).

while to note that in order to achieve a similar oxidizing potential by use of pure oxygen, the chamber pressure should be $\approx 10^5$ Torr. Such high pressure is meaningless for MBE[1].). The thermodynamic phase diagram (Fig. 3.14) also contains the equilibrium oxidation potential line for the use of radical oxygen. Although the growth chamber (Fig. 3.1) is equipped with a radical oxygen source, it was found that ozone yields superior results. Since the calculated equilibrium oxidation potential lines do not include finite lifetime

[1] Oxidizing potentials are listed in Table 8.1

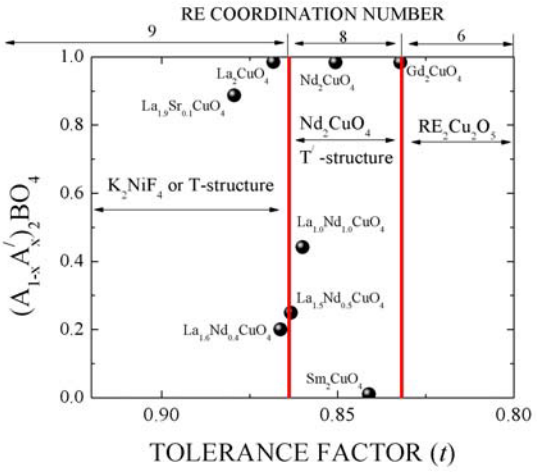

Fig. 3.18: Phase diagram of crystal structure vs. tolerance factor for various materials. Data points taken from Bringley *et al.* [184].

effects (see Fig. 8.12 on page 179), the effective oxidation potential of ozone is higher. However, once the growth is finished, the sample is subjected to annealing in UHV environment. The UHV conditions were kept the same for all samples irrespective of the rare earth element or the cerium content. This step is the most crucial step for the synthesis of electron doped cuprate superconductors. Plausible scenarios for the underlying mechanism during the reduction process are discussed in Chapter 4. Since superconductivity was found in electron doped cuprates, the reduction process was performed in a more or less arbitrary way were the as-grown sample (bulk or thin films) is heated up to a certain temperature in vacuum or flowing argon for a certain time in order to remove apical oxygen. Since the reduction process is of diffusive nature, homogeneous annealing is a difficult task for bulk samples. Therefore, the annealing time is extended. On the other hand, the cuprate itself is not stable under such conditions and therefore starts decomposing. The decomposition products themselves have, of course, different physical properties than the desired 214 phase[2]. However, in contrast the formation

[2] Delafossite type phase $NdCuO_2$ [188], monoclinically ordered $Nd_4Cu_2O_7$ with monovalent copper [189] and Sr_2CuO_3-type structured $Nd_2CuO_{3.5}$ [190] together with simple oxides Nd_2O_3 and Cu_2O are typical decomposition products with completely different crystal structures.

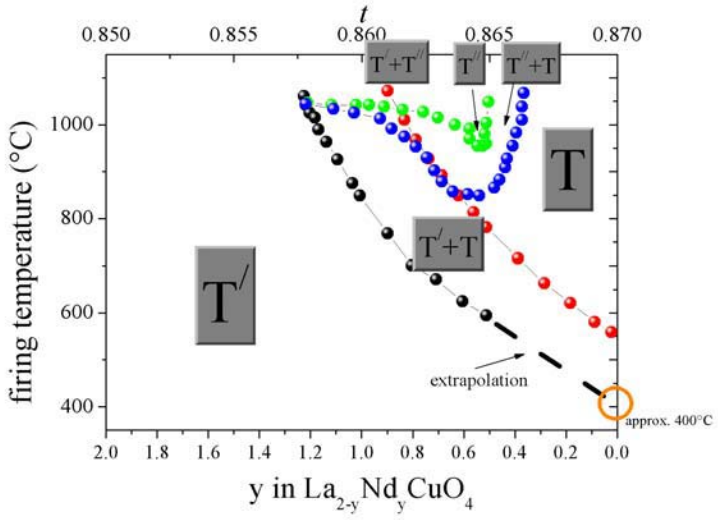

Fig. 3.19: Phase relationship for the system $La_{2-y}Nd_yCuO_4$ obtained by firing the co-precipitated hydroxide/carbonate progressively at higher temperatures[185]. Black points basically separate the T′-phase from T or T″-phases. Mixture of T′ and T-phase was observed in the region between red- and black lines. Above the red line the T-phase dominates the phase diagram.

of decomposition phases is avoided by the aid of RHEED in the case of MBE grown thin films. Since RHEED is sensitive to the surface, any deviation from the 214 phase can be observed in real time. After the growth of 214 phase compounds, the sample is rapidly cooled to 400 °C. Then, the sample temperature is increased in steps of 10 °C, whereby each temperature is kept stable for 10 min. As soon as any changes in the RHEED pattern is observed (appearance of spots, vanishing of streaks, etc.), this temperature is therefore set to be the decomposition temperature. Applying this method to the reduction process leads to optimally reduced samples without decomposition products.

As it is well known from bulk synthesis [191], the hole doped side of the cuprate phase diagram is represented by $La_{2-x}Sr_xCuO_4$. For the electron doped side there exist $RE_{2-x}Ce_xCuO_4$ with RE = Pr, Nd, Sm and Eu but not $La_{2-x}Ce_xCuO_4$. $La_{2-x}Ce_xCuO_4$ has not been synthesized so far in bulk form. This in fact is a consequence of the temperature dependency of the tolerance factor t. The limitations of bulk synthesis caused by the tempera-

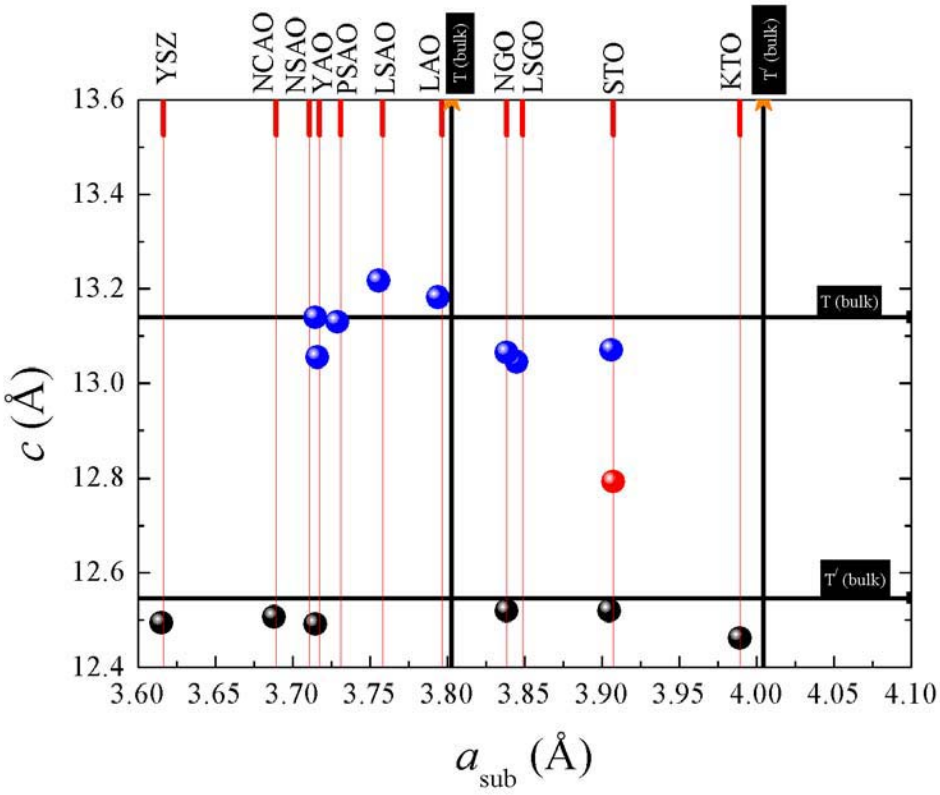

Fig. 3.20: c-axis and a-axis of thin films of T-La_2CuO_4 and T′-La_2CuO_4 for various substrates grown at $\vartheta = 550\,^{\circ}\mathrm{C}$. Substrate materials: (111)Yttria stabilized ZrO_2 [YSZ], (100)$NdCaAlO_4$ [NCAO], (100)$NdSrAlO_4$ [NSAO], (110) $YAlO_3$ [YAO], (100)$PrSrAlO_4$ [PSAO], (001)$LaAlO_3$ [LAO], (110)$NdGaO_3$ [NGO], (100)$LaSrGaO_4$ [LSGO], (001)$SrTiO_3$ [STO] and (110)$KTaO_3$ [KTO]. Note that the bulk values of the lattice parameters of T′-La_2CuO_4 are extrapolated from the T′-RE_2CuO_4 homologue series using the ionic radii values in Table 3.1. Adapted from Naito *et al.* [186]. Note, in the case of (001)$SrTiO_3$ substrates, also the T*-structure can be stabilized (red dot), where copper is pyramidal coordinated [187].

ture dependency of the tolerance factor t is circumvented by using reactive MBE technique. However, the case for RE = La is a special case and needs to be discussed in more detail, since it does not exist in bulk material, so far.

RE	r_i ionic radius (Å)
La^{3+}	(VIII) 1.16 (IX) 1.216
Ce^{4+}	(VIII) 0.97
Pr^{3+}	(VIII) 1.126
Nd^{3+}	(VIII) 1.109
Sm^{3+}	(VIII) 1.079
Eu^{3+}	(VIII) 1.066
Gd^{3+}	(VIII) 1.053
Y^{3+}	(VIII) 1.019
Tb^{3+}	(VIII) 1.04
Tb^{4+}	(VIII) 0.88
Tm^{3+}	(VIII) 0.994
Cu^{2+}	(IV) 0.57
Cu^{2+}	(VI) 0.73

Tab. 3.1: Ionic radii of various elements used in this thesis. After Shannon [192].

3.4.2 Impact of the substrate

The tolerance factor t was initially proposed to predict the stability of the perovskite structure ABO_3 [193]. It presents the bond length matching between AO layers and BO_2 layers. Ideal matching corresponds to $t = 1$, and the perovskite structure is stable within $0.8 < t < 1.0$. Similar arguments work in the case of K_2NiF_4 structures [194] and hence, the rules governing the perovskites may also be applied to the stability of K_2NiF_4-structures.
On the basis of a systematic investigation of the mixed lanthanide system $La_{2-x}RE_xCuO_4$, in which the tolerance factor t (Eq. 3.13) can be varied continuously, Bringley *et al.* [184] found that the T-structure is stable for $0.87 \leq t \leq 0.99$, whereas the stability region for the T′-structure lies between $0.83 \leq t \leq 0.86$. For tolerance factors smaller than $t < 0.83$, the so-called $Ho_2Cu_2O_5$-structure is formed (with six-fold coordinated RE-ions). These results can be interpreted in the following way. When t is close to 1, i.e., when the bond length matching is nearly ideal, the stability of T-structured phases are favorable. If the tolerance factor t is substantially smaller than 1 (because the rare earth ionic radii shrink), the T phase becomes unstable. The first indication of T-phase instability is the occurrence of orthorhombic and even monoclinic distortions as seen in La_2CuO_4, where $t \approx 0.868$ [195].

The distortions occur in a way in order to accommodate the large bond length mismatch by tilting the CuO_6 octahedra. For $t < 0.86$, the bond

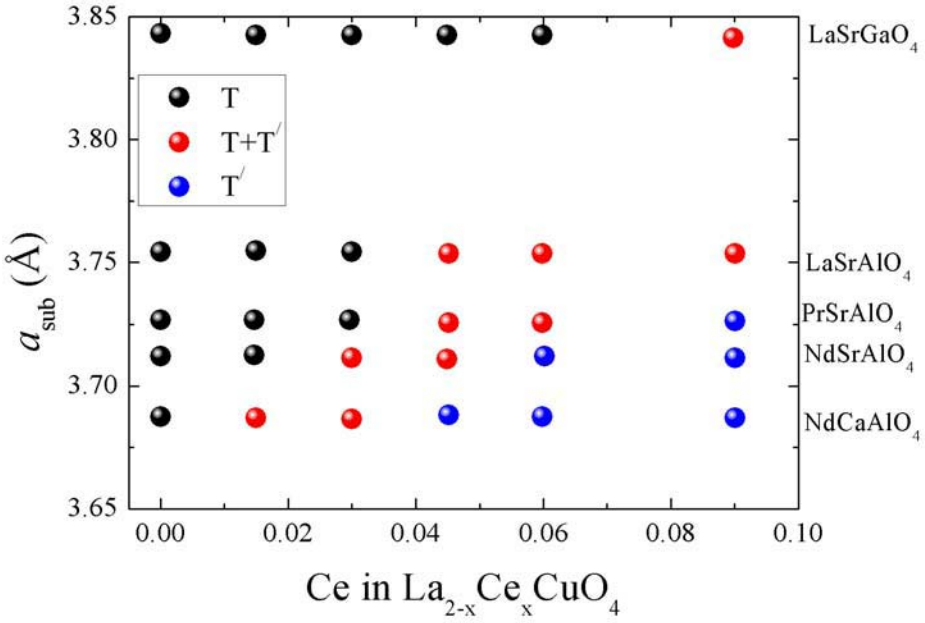

Fig. 3.21: Influence of the cerium concentration and the substrate in-plane lattice constant a_{sub} on the phase boundary of $La_{2-x}Ce_xCuO_4$. Black dots mark the region where pure T-structure has been found while blue ones represent single phase T′-structured $La_{2-x}Ce_xCuO_4$. Simultaneously, T- and T′-phase have been found in the region marked by red dots. There is a clear trend, that larger substrate lattice parameters a_{sub} are stabilizing the T-phase until higher x is reached. Ce doping provides electrons effectively for the CuO_2-plane and therefore stretch stretch the Cu-O bonds by filling electrons into the antibonding $dp\sigma$ orbitals. As a consequence, the in-plane lattice constant expands. Adapted from Naito *et al.* [186].

length mismatch becomes intolerable, resulting in a transformation to the T′-phase. The critical value for the T→T′ transition is around $t_c \approx 0.865$. In addition, Manthiram *et al.* [185] investigated the undoped $La_{2-y}Nd_yCuO_4$ system. The result is shown in Fig. 3.19. Pure Nd_2CuO_4 crystallizes in the T′-structure and no transition to the T structure has been found. When lanthanum is added, a structural change occurs when crossing the black-dotted

line in Fig. 3.19 separating the T′ from the T phase[3].
It has been already mentioned above, that there exists a threshold line between T- and T′-structured 214 cuprate phases. According to Figure 3.19, this threshold shows a temperature dependency where higher synthesis temperatures favor the T phase. The origin of this temperature dependency originates from the temperature dependency of the Tolerance factor

$$t = \frac{r_{RE^{3+}} + r_{O^{2-}}}{\sqrt{2}\,(r_{Cu^{2+}} + r_{O^{2-}})} \tag{3.13}$$

where $r_{RE^{3+}}$, $r_{Cu^{2+}}$ and $r_{O^{2-}}$ are the empirical room-temperature ionic radii for RE^{3+}, Cu^{2+} and O^{2-} ions by Shannon and Prewitt [192].
Beside the temperature dependency of the tolerance factor itself, the choice of the substrate plays a prominent role on the threshold line between the T- and T′-structure in the growth of epitaxial thin films. The influence of the substrate on the selective phase stabilization of 214 films deposited under identical growth conditions has been investigated by Naito *et al.* [186] and is shown in Fig. 3.20 and Fig. 3.21. In Fig. 3.20 the c-axis length of La_2CuO_4 versus its in-plane axis length a is plotted for various substrate materials. The phase stabilization of T- or T′-structured 214 phase is influenced by the lattice matching between the substrate and the thin film. For the case of (001)$SrTiO_3$ substrates, both phases are possible. Moreover, even the case for pyramidal coordinated copper is possible, the so-called T⋆-structure. However, the crystalline quality is superior for the T-structured La_2CuO_4 phase compared to the T′-structured analogue. Although the samples are single phase, the crystallinity (determined from the FWHM of the (006) peak) is poor compared to cerium doped samples with cerium concentration larger than 0.06.
The threshold between the T- and the T′-phase in $La_{2-x}Ce_xCuO_4$ has been also investigated by varying the cerium concentration as well as the substrate material and is shown in Fig. 3.21. It is found that for substrates with a larger in-plane lattice, the threshold is shifted to higher cerium concentrations. Since the ionic radius of cerium is much smaller than that of lanthanum (see Table 3.1), the tolerance factor is increased and therefore the T′-phase stability is enhanced.

[3] This result is verified using neutron diffraction [196].

4

The reduction process

Since the beginning of the investigation of electron doped high temperature superconductors it was realized that superconductivity could only be induced in those samples that are subjected to an additional annealing step under reducing atmospheric conditions (i.e., inert gas or vacuum) [197, 198]. Without this additional treatment, the resistivity behavior of the samples shows a semiconducting temperature dependence and no superconductivity[199]. A typical behavior of this is given in Fig. 4.1 as an example of single crystalline $Pr_{1.85}Ce_{0.15}CuO_{4+\delta}$. During this reduction step the oxygen content δ of the sample ($x = 0.15$) decreases only by $\Delta\delta \approx -0.01$. The oxygen content can be estimated by thermogravimetric technique. Thereby the weight loss of 10 mg sample material under various partial oxygen pressures p_{O_2} was measured temperature dependent at the thermodynamic equilibrium state. With thermogravimetric technique it is possible to obtain a high resolution of the $\Delta\delta$ value down to 0.001. In Fig. 4.2 the $\Delta\delta$ dependency of temperature and oxygen pressure p_{O_2} are shown [201, 202, 203, 204, 205]. Rapid cooling of the sample after the reduction process ($> 10\,\mathrm{K/min}$) freezes the achieved drop of $\Delta\delta$ [206]. Due to the fact that a tiny decrease of δ obviously shows a dramatic impact on the superconducting and normal state properties [207, 208, 209], there remains the question of the origin of this behavior and hence there exists the question of the absolute amount of oxygen δ in the superconducting sample [210]. In order to achieve maximum T_c in the $RE_{2-x}Ce_xCuO_{4+\delta}$-system, whether the value of δ is equal, smaller or larger than zero?

In order to answer this serious question, it is necessary to determine the value of δ before and after the reduction process due to the possibility that the sam-

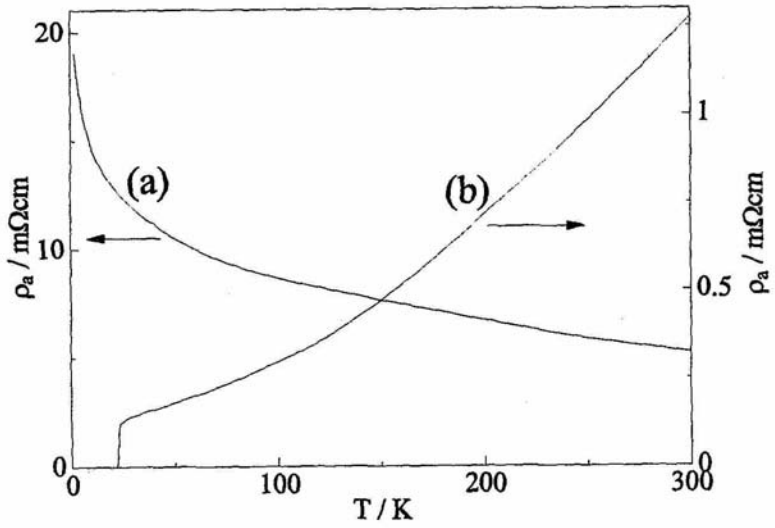

Fig. 4.1: Electrical resistivity of a single crystal $Pr_{1.85}Ce_{0.15}CuO_{4+\delta}$-sample before (a) and after (b) the reduction process. From [200].

ples may have an excess amount of oxygen which decrease partially or totally during the reduction process or, the reduction process produces an oxygen deficiency $\delta < 0$ [211]. The determination of the absolute amount of oxygen is difficult and the method has certain limitations. Usually, the method of wet-chemical analysis of double iodometric titration technique is used [212]. Within this method the valency of the Cu-cation is measured. Therefore the valency of the other ions (RE^{3+}, O^{2-} and $Ce^{3.84+}$) is assumed. To determine the valency of the copper ion a polycrystalline sample $RE_{1.85}Ce_{0.15}CuO_{4+\delta}$ is dissolved in a KI containing acid. The complete amount of copper forms the monovalent compound CuI and the remaining I_2 in the solution determines the original valency of copper. In order to achieve a measurement resolution in the range of 0.01 of δ it requires a minimum sample weight of a few mg. Therefore only polycrystalline samples had been used. As a result several values for nonsuperconducting $RE_{1.85}Ce_{0.15}CuO_{4+\delta}$ samples of δ_0 are given in literature within the range of 0 to 0.03. So, the optimal superconducting state (depending on the amount of oxygen) sometimes shows an oxygen deficiency ($\delta = \delta_0 - \Delta\delta < 0$)[204, 202, 201, 203], sometimes an excess amount of oxygen [213, 214, 206, 215] and even perfect oxygen stoichiometry

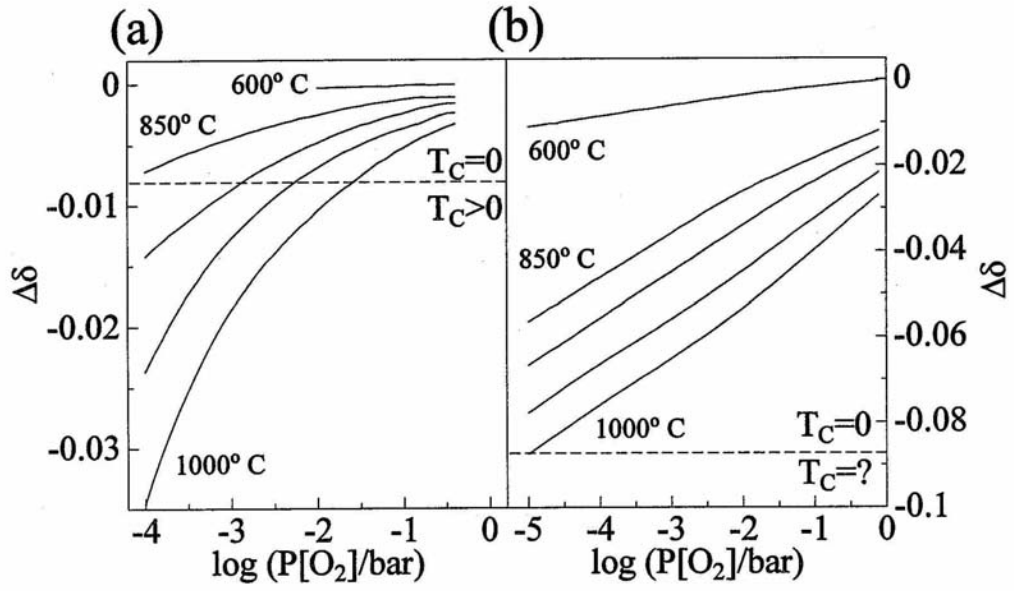

Fig. 4.2: Variation of the oxygen content δ of poly-crystalline $Nd_{2-x}Ce_xCuO_{4+\delta}$, (a) case $x = 0$ and (b) $x = 0.15$ for different reduction temperatures as a function of the oxygen partial pressure p_{O_2}. From [201, 203].

$(\delta = 0)$[216, 217].

The procedure of the wet chemical analysis has to be viewed critically because first of all, it is not possible to determine the valency of Cerium directly [218] and secondly, polycrystalline material shows non-stoichiometric compounds at the grain boundary. In summary, it is an experimental fact that the relative variation $\Delta\delta$ of oxygen between the superconducting and the nonsuperconducting phase could be determined precisely in the $RE_{1.85}Ce_{0.15}CuO_{4+\delta}$-system but not the absolute value of δ.

Hence, solving the puzzle of the optimal value of δ for a maximum in T_c is tremendously necessary for an explanation of superconductivity in T'-compounds, where several models of explanation are given and are as follows. Within the model of extra electron doping due to oxygen vacancies, it is assumed that the superconducting phase shows an oxygen deficiency $\delta \approx -0.01$. Therefore, it is possible that the missing oxygen anions in the $RE_{1.85}Ce_{0.15}CuO_{4+\delta}$-system generate additional doping of $2|\delta| \approx 0.02$ electrons which are necessary to set metallic conductivity and superconductivity. Hence, the total amount of free charge carriers in this scenario would

be $x + 2|\delta| = 0.17$. Here, it is assumed that, each Ce-atom provides one electron to the conducting band and each missing oxygen anion left two electrons to the lattice. In case of only additional doping of oxygen vacancies, a $RE_{1.83}Ce_{0.17}CuO_{4+\delta}$ sample should show superconductivity without the vacuum annealing process. But, for such a sample ($x = 0.17$) superconductivity is induced only after the annealing step. On the other hand one may think that it may be possible to induce superconductivity to a Ce-free non-doped $RE_2CuO_{4+\delta}$ sample just by creating oxygen vacancies. It was found that, in the case of $x = 0$, the amount of oxygen vacancies is much larger than those for $x = 0.15$ case. As an example, this inter-relationship is shown in Fig. 4.2. The estimation of the amount of excess oxygen in non-doped and non-reduced sample by iodometric titration technique provides that $\delta_0 \approx 0.01$. In order to achieve the required concentration of electrons of 0.17 per formula unit, it is necessary to accomplish $\delta \approx 0.85$ by the reduction step. Nevertheless, Ce-free T' compounds show for various amounts of δ semiconducting behavior with resistivity values larger than $1\,\Omega cm$ at low temperatures. This means, that the electrons induced by oxygen vacancies for $x = 0$ scarcely delocalize and therefore there is only a weak contribution to metallic conductivity.
A certain pertinence of the idea of extra electron doping by oxygen deficiencies still remains in the $Gd_{1.85}Ce_{0.15}CuO_{4+\delta}$-system where superconductivity was not yet found because of the arduousness to remove homogeneously excess oxygen of $\delta_0 \approx 0.05$ [219]. The above mentioned calculation of the charge carrier density leads to a maximum value of $x-2|\delta| = 0.05$, a very tiny value, through which the lack of superconductivity for R = Gd could be explained. In summary, it should be pointed out that it is not possible explaining the impact of oxygen vacancies in T′-compounds by a simple model of additional doping.
Finding an explanation of the behavior of oxygen doped superconductors, the distribution of the oxygen vacancies inside the lattice of the T′ structure has a significant impact. Figure 4.3 shows the positions of the two regular oxygen lattice places O1 and O2. While the O1 positions are arranged in the superconducting CuO_2-planes the O2 occupies the $(REO)_2$ intermediate layer above the O1 position. Oyanagi *et al.* [220, 221] first indicated the position of the excess oxygen atoms above the Cu atoms. This Oi-position of $(0, 0, \approx 0.2)$ inside the unit cell corresponds to the apex-oxygen position of the T-structure of the $La_{2-x}Sr_xCuO_{4+\delta}$. Regularly this position is not occupied in the T′-structure.

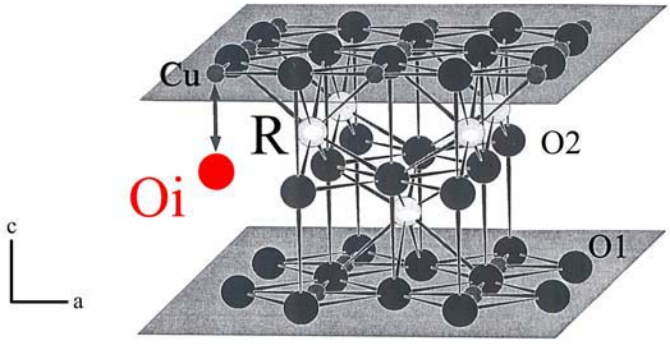

Fig. 4.3: Position of regular oxygen position O1 and O2 and the interstitial oxygen Oi in the T′ structure. .

Reference	x	as grown			reduced		
		n(O1)	n(O2)	n(Oi)	n(O1)	n(O2)	n(Oi)
Radaelli [91]	0.00	1.96(2)	1.90(2)	0.10(2)	1.94(2)	1.91(2)	0.04(1)
Marin [222]	0.00	1.99(3)	1.94(3)	0.00(3)	1.95(3)	1.94(3)	0.00(3)
Mangelshots [223]	0.15		- - -		2.00	2.01(4)	0.02(2)
Izumi [224]	0.15	2.00	1.93(2)	-	1.98(2)	1.93(2)	-
Takayama [225]	0.15		- - -		1.95(2)	1.92(2)	-
Schultz [226]	0.15	1.96(2)	1.93(2)	0.06(1)	1.96(2)	1.96(2)	0.04(1)

Tab. 4.1: Distribution of oxygen vacancies at the lattice places O1, O2 and Oi in $Nd_{2-x}Ce_xCuO_{4+\delta}$ (measured by elastic neutron scattering). In the case of an ideal arrangement the relation n(O1) = n(O2) = 2, n(Oi) = 0 is valid.

In order to determine the distribution of oxygen vacancies of the three oxygen places elastic neutron diffraction is used. In Table 4.1 some of the results are summarized.

Comparing the data before and after the reduction process three main differences are found:

1. In almost all cases there is a big deficiency at the O2-position, which is larger for non-doped ($x = 0$) samples ($\delta \approx -0.08$) than for $x = 0.15$ ($\delta \approx -0.03$)

2. Marin *et al.* found mainly an oxygen deficiency at the O1 position

3. Radelli *et al.* and Schultz *et al.* found mainly an emptying of the

Oi-position after the reduction process

Although it was found by Marin *et al.* and Izumi *et al.* that, there is a large deficit at O1-positions (this means inside the CuO_2-plane), nowadays it is assumed that a blank O1 position suppresses the metallic and superconducting properties due to the fact that the narrow conduction band becomes rapidly disturbed. A thorough neutron diffraction study on $Nd_{1.9}Ce_{0.1}CuO_{4\pm\delta}$ carried out by Petrov *et al.* [227] for different annealing conditions unambiguously showed, that higher reduction temperatures and lower partial oxygen pressure leads to a less occupied Oi position. Also in the case of Petrov *et al.*, the O1 occupation was 1.96 indicating oxygen deficiencies at the O1 site. However, the reduction conditions did not affect the O1 site occupation.
Another approach to this problem was described within the model of Hirsch [228]. There it is presumed that the reduction process generates oxygen vacancies at the O2-position whereby superconductivity is induced in the sample. This idea is based on the observation of a change of the algebraic sign of the Hall-constant which means that negative and positive charge carriers are responsible of the electronic properties. Figure 4.4 demonstrates

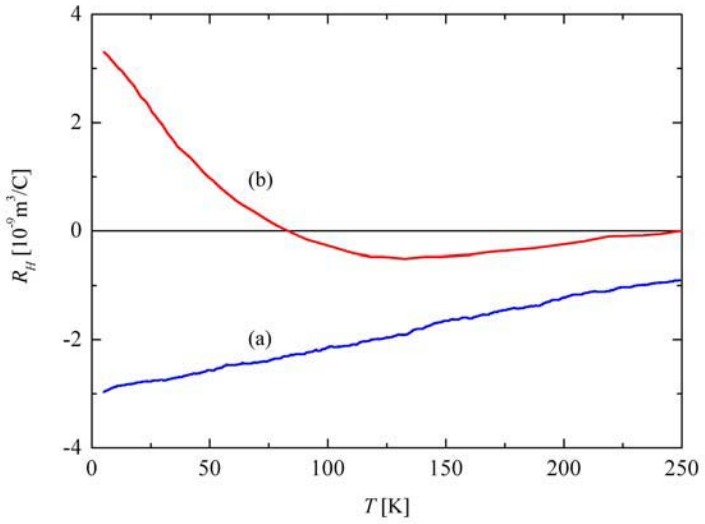

Fig. 4.4: Hall-coefficient R_H of single crystalline $Pr_{2-x}Ce_xCuO_{4+\delta}$ before the reduction process (a) and after the reduction process (b). In the case of (a), the sample does not show superconducting properties. From [200].

the hall coefficient R_H before and after the vacuum annealing step. In the case of the non-superconducting state (a) the hall coefficient is negative in the total temperature range. Considering the relationship of non-interacting charge carriers in a simple single band model with $2x = 0.3$ electrons per unit cell this leads to the temperature independent value of the hall coefficient of $\approx -4 \cdot 10^{-9}\,\mathrm{m}^3/\mathrm{C}$. This matches roughly with the range measured in Fig. 4.4. Moreover, the algebraic sign remains negative. In the case of the superconducting sample (b), the hall coefficient changes its algebraic sign around $T \approx 80\,\mathrm{K}$ and turns to high positive values. This unconventional low-temperature behavior can not be explained by conventional single band models. Therefore it is conjectured that not only electrons are responsible for the superconductivity but also positive charged charge carriers [229]. Within the two-band model noninteracting charge carriers of different algebraic signs the hall coefficient is given by:

$$R_H = e \cdot \frac{p \cdot \mu_h^2 - n \cdot \mu_e^2}{\sigma_e + \sigma_h} \tag{4.1}$$

Drawing a possible scenario, an increasing mobility of the positive charge carriers with decreasing temperature may cause the algebraic sign change of R_H. Therefore additional holes may have been created in the crystal which had not been there in the oxidized state (see Fig. 4.4(a)). The model of Hirsch describes the induction of holes due to oxygen vacancies at the O2-position to the CuO_2-plane and the binding energies of the doped charge carriers in the potential of the lattice ions are calculated. Binding energies of the covalency type are neglected. A scheme of this process is given in Fig. 4.5 and a description of the doping process is given below.
In the $RE_{1.85}Ce_{0.15}CuO_{4+\delta}$ system the CuO_2-planes can be easily doped by the electrons of Ce. These electrons are unable to delocalize due to the positive charge of the $(Ce^{3+})^+$ (binding energy $\approx$ 4.35 eV). Close to the localized negative charge an electron-hole excitation is likely and therefore the following equation for electron doping into the CuO_2-planes is valid:

$$e^- + 2Cu^{2+} + O^{2-} \longrightarrow 2Cu^+ + O^- \tag{4.2}$$

Nevertheless, the electron as the electron-hole excitation remains localized (binding energy $\approx$ 3.28 eV) and therefore no metallicity nor superconductivity is induced. Now, the reduction process generates oxygen vacancies at the O2-position, which most likely are at the opposite site of the CuO_2-plane

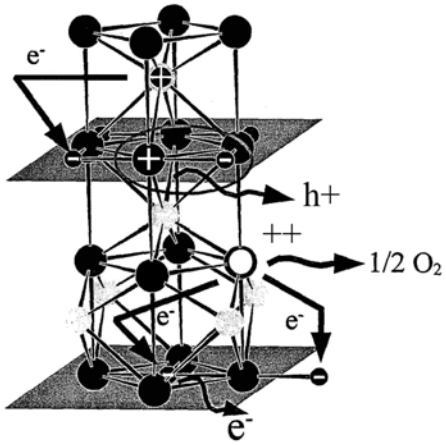

Fig. 4.5: Electron-hole doping within the Hirsch-model. The structure shows one part of the unit cell of the T′-system, containing two CuO_2-planes (grey shaded areas, Cu^{2+}: small grey spheres, O1: big black spheres) and two layers of O2-anions. One of the RE^{3+}-ions was substituted by Ce^{4+}.

(gain of energy, electron doping at this certain position generates a negative repulsion to the O^{2-}-ion). The environment of the new O2-vacancy is positive charged whereby the binding energy of the hole is further decreased (-0.36eV) and so it delocalises. Therefore two bound electrons at the $(Ce^{3+})^+$ and O2-vacancy positions remains. In addition, during the reduction process oxygen abandon the crystal molecularly whereas two more electrons remain in the lattice grabbed by the lower CuO_2-plane (the upper CuO_2-plane is already negative charged from the localized electrons). The binding energies of these two O^{2-}-electrons are lower than the Ce^{4+}-electron whereby one delocalises. The doping by Ce and the O2-vacancy leads in total to a delocalization of a hole and an electron in adjacent CuO_2-planes. Electronic properties have to be explained by the two-band model.
While the Hirsch-model is focused on the introduction of O2-vacancies due to the reduction process leading to superconductivity, the model of interstitial oxygen mainly describes the removal of oxygen scattering centers at Oi-positions. Simultaneously, the position of the O2-places exhibits a tremendous amount of vacancies in the as-grown and the reduced case. This deficit is almost stable during the reduction process. In total, the amount of oxygen δ decreases from -0.04 down to -0.11 for $x = 0$ and it remains constant for $x = 0.15$. These results presume that the vacancy of the interstitial posi-

tion Oi is essential for superconductivity. During the growth of the samples, atomic interstitial oxygen is built-in most likely near the Ce-cation due to the possibility of a charge transfer to oxygen. This is schematically shown in Fig. 4.6. Due to interstitial oxygen, the doping electron may not be added

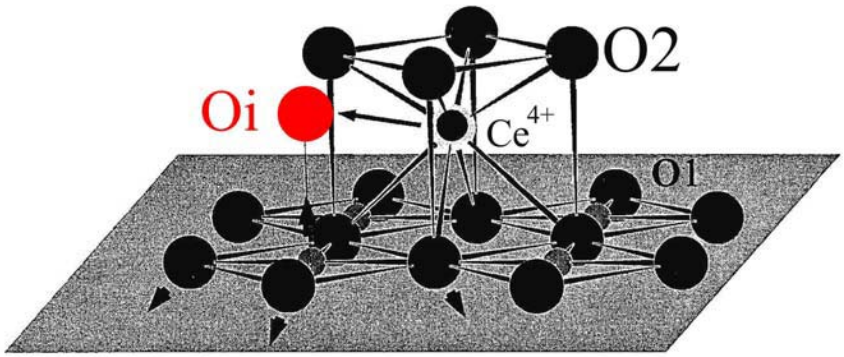

Fig. 4.6: Impact of interstitial oxygen on the electron doping by Ce. The doping electron may either jump to the CuO_2-plane or may be trapped by the interstitial oxygen. From [200].

to the CuO_2-plane, but remains at the Oi oxygen site. This leads to a drop of charge carriers for $x = 0.15$ of roughly 0.02 per formula unit between the as-grown and the reduced state.
Nevertheless, this influence of interstitial oxygen may not be the only impact mechanism because in that case it should be possible to achieve superconductivity by increasing the amount of Ce to $x = 0.17$. It is an experimental fact that the reduction step is necessary for all doping levels to induce superconductivity. Therefore it is assumed that the distortion of the periodicity of the lattice by interstitial oxygen strongly influences the transport properties, leading to local deformation of the CuO_2-planes (attractive potential to the Cu^{2+}-ion, repulsive potential to the O1-ions) and on the other hand, a giant distortion potential nearby the CuO_2-planes [230] leads to a big scattering rate regarding the quasi-two-dimensional electron gas in the planes, because the Oi-charges are not shielded by the conducting electrons. Due to the occupation of interstitial oxygen sites the antiferromagnetic order of the Cu^{2+} spins remains stable [27] and therefore by removing of interstitial oxygen long range ordered magnetic correlations diminishes whereby the system becomes metallic and finally superconducting. The impact on transport properties of the introduced lattice distortion due to interstitial oxygen is

perhaps stronger than the vacancies at regular O2-sites (no change before and after the reduction step). As already mentioned above the variation of δ is larger for non-doped $Nd_2CuO_{4+\delta}$ than in the $Nd_{1.85}Ce_{0.15}CuO_{4+\delta}$ system. Figure 4.7 shows the decrease of the oxygen content (as-grown to reduced) depending on the doping level x. The measurement was performed by using

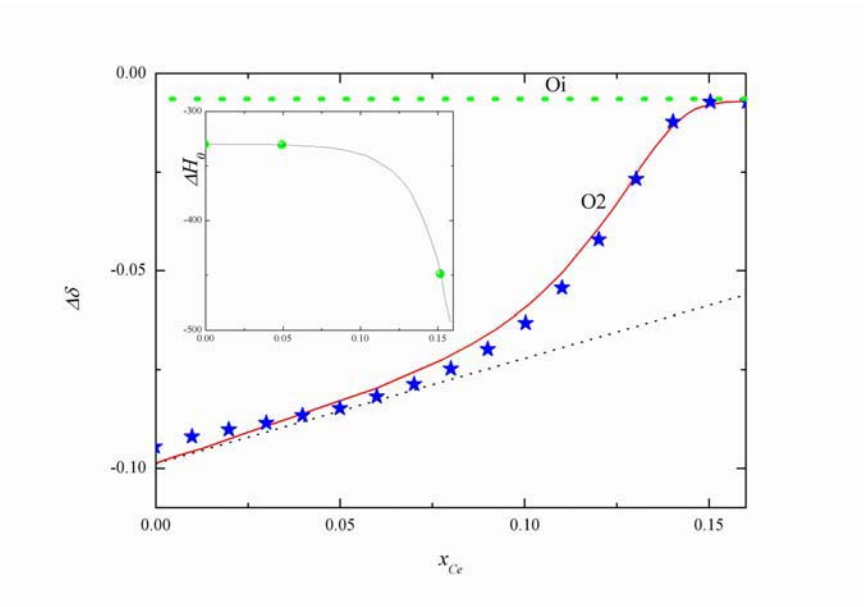

Fig. 4.7: Decreasing amount of oxygen $\Delta\delta$ between the as-grown sample and the annealed sample vs. doping level x [213]. The red-solid line is a result of calculation taking into account the chemical potential of the Ce-electrons. The dotted line ΔH_0 is assumed being doping level independent. The green dotted line shows the doping independent contribution of the Oi-atoms. Data taken from [201].

thermogravimetric technique. Regrettably it is impossible to distinguish between vacancies at the Oi or the O2 sites. Therefore it is assumed that both processes lead to a decreasing value of δ. The following equation describes the generation of vacancies at the O2-site:

$$4Cu^{2+} + 2O^{2-} \longrightarrow 4Cu^{+} + 2V\{O2\} + O_2 \tag{4.3}$$

Here, $V\{O2\}$ describes a vacancy at the O2-site. This reaction is an exothermal process with the equilibrium constant K_{O2}:

$$K_{O2} = \frac{n^2\left[V\{O2\}\right] \cdot n^4\left[Cu^{+}\right]}{n^2\left[O^{2-}\right] \cdot n^4\left[Cu^{2+}\right]} \cdot p\left[O_2\right] \tag{4.4}$$

The exothermal removal of interstitial oxygen O^{z-} is as follows:

$$2z\mathrm{Cu}^{2+} + 2\mathrm{O}^{z-} \longrightarrow 2z\mathrm{Cu}^{+} + 2V\{\mathrm{Oi}\} + \mathrm{O}_2 \tag{4.5}$$

Here, it is assumed that the valency of the interstitial oxygen is equal to z ($0 \leq z \leq 2$). The equilibrium constant of this reaction is given through:

$$K_{O2} = \frac{n^2\left[V\{\mathrm{Oi2}\}\right] \cdot n^{2z}\left[\mathrm{Cu}^{+}\right]}{n^2\left[\mathrm{O}^{z-}\right] \cdot n^{2z}\left[\mathrm{Cu}^{2+}\right]} \cdot p\left[O_2\right] \tag{4.6}$$

The recombination of O2 vacancies and interstitial Oi oxygen is calculated by the sum of equation 4.3 and 4.5 and the equilibrium constant is given by the quotient of equation 4.4 and 4.6. Normalization of the occupation number n to one formula unit of $\mathrm{RE}_{2-x}\mathrm{Ce}_x\mathrm{CuO}_{4+\delta}$ leads to:

$$1 = n\left[\mathrm{Cu}^{2+}\right] + n\left[\mathrm{Cu}^{+}\right] \tag{4.7}$$

and

$$\delta = n\left[\mathrm{O}^{z+}\right] - n\left[V\{\mathrm{O2}\}\right] \tag{4.8}$$

From this follows for the medial valency of Cu:

$$V_{\mathrm{Cu}} = 2 - 0.84 \cdot x - 2\left(n\left[V\{\mathrm{O2}\}\right] - z \cdot n\left[\mathrm{O}^{z+}\right]\right) \tag{4.9}$$

whereby $V_{\mathrm{Cu}} = 1 + n\left[\mathrm{Cu}^{2+}\right] = 2 - n\left[\mathrm{Cu}^{+}\right]$ is valid for simultaneously Ce- and O-doping. In the thermodynamic limit the equilibrium constants are given by an Arrhenius-Ansatz:

$$K(T) = K_0 \cdot e^{\frac{\Delta H_0}{RT}}. \tag{4.10}$$

Figure 4.8 shows the three different energy levels. By changing the oxygen partial pressure p_{O_2}, and/or the temperature T, this equilibrium becomes tuneable. Using equation 4.3 - 4.10 and knowing the values of ΔH_0 and K_0 one can calculate the occupation of the O2 and Oi as a function of the doping level x for various reduction conditions (T, p_{O_2}) in the thermodynamical equilibrium. Idemoto *et al.* [231] estimated the enthalpy change of the $\mathrm{Nd_2CuO_{4+\delta}}$ of $\Delta H_0[O2] \approx -330\frac{\mathrm{kJ}}{\mathrm{mol}}$, Suzuki *et al.* [232] found $\Delta H_0[O2] \approx -440\frac{\mathrm{kJ}}{\mathrm{mol}}$. In the case of $x = 0.15$, this value increases to $\Delta H_0[O2] \approx -390\frac{\mathrm{kJ}}{\mathrm{mol}}$, Kim *et al.*[203] found $\Delta H_0[O2] \approx -470\frac{\mathrm{kJ}}{\mathrm{mol}}$. Zhu *et al.*[217] pointed out that the values of $-\Delta H_0[O2]$ and $\Delta H_0[Oi]$ are roughly equal for the case $x = 0.15$. In the following, the occupation of O2 as a

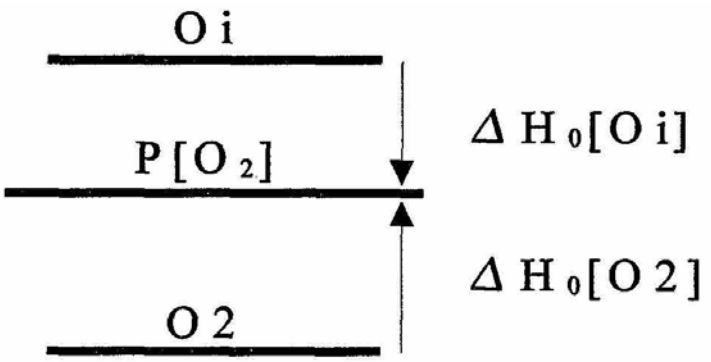

Fig. 4.8: Schematic Illustration of the reaction enthalpies from equations 4.3 and 4.4. Interstitial sites deplete either by leaving the sample or recombine to an O2-site. An endogenous reaction removes O2-oxygen.

function of the doping level is to be considered, which depends on the charge balance (equation 4.9). A degradation of the Cu-valency due to an increase of x, shifts equilibrium of equation 4.4 towards lower vacancy concentration n[O2]. The additional contribution of decreasing $\Delta\delta$ due to the chemical pressure of the Ce-electron corresponds to the dotted line in Fig. 4.7 whereby ΔH_0[O2] is assumed being independent on the Ce-concentration. Obviously, this curve matches very well with experimental data for low doping levels, while at $x = 0.1$ $|\Delta\delta(x)|$ fall off rapidly. This may be caused by the Ce-dependency of ΔH_0[O2]. An increase of this quantity (with increasing Ce) leads to a drop of vacancies $V[O^{2-}]$ (see equation 4.4 and 4.10).
According to Zhu *et al.* [217, 210, 233] an increase of $|\Delta H_0[O2]|$ is caused by a bondlength relaxation process and is shown in Fig. 4.9. Due to electrostatic repulsion between the O2 anions, the $(REO)_2$-interlayer tries to expand the lattice parameter a. Indeed, the lattice parameter a of the T′-structure ($\approx 3.9 - 4.0\,\text{Å}$) is about 3% higher, compared to the T-system $La_{2-x}Sr_xCuO_{4+\delta}$, because within the T-structure the O2(apex)-oxygen distance inside the $(LaO)_2$ interlayer is due to different crystalline order. Therefore there is a tensile strength along the a-direction in the T′-system. $(Ce^{3+})^+$-doping and generating of O2-vacancies reduce the bondlength-mismatch between the layers. Thereby, the Coulomb repulsion at the $(REO)_2$ intermediate layer is compensated and hence the CuO-bondlength increases towards antibonding state with increasing Ce-doping. The increase of the lattice parameter a increases with Ce-doping or O2-vacancies by only

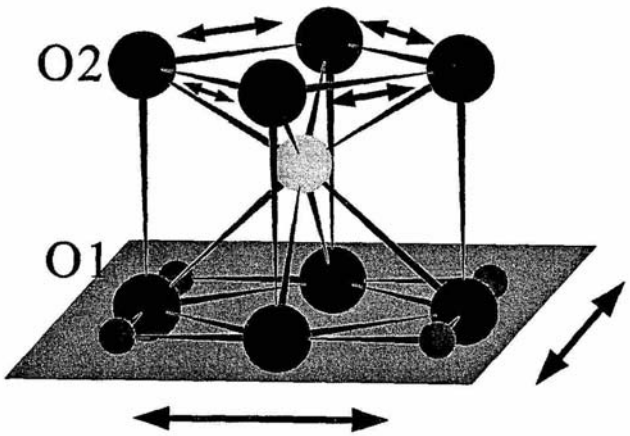

Fig. 4.9: Visualization of the electro statical strain between the CuO_2-planes (grey shaded area) and the $(REO)_{2-}$-interlayer. The repulsion between the O2-anions (small double arrows) tries to enlarge the lattice parameter a. This results a strain of the CuO bond inside the CuO_2-planes (large double arrows).

about 0.01 Å. In other terms this means that decreasing of lattice strength strongly affects the reaction enthalpy creating O2-vacancies (equation 4.3). Increasing the doping level minimizes this contribution and therefore $|\Delta H_0[\mathrm{O2}]|$ increases, too. So, the equilibrium point of equation 4.3 is shifted left hand side, which means that there are less O2-vacancies. Assuming an exponential behavior of $|\Delta H_0[\mathrm{O2}]|(x)$ (inset of Fig. 4.7) the dependency of $\delta(x)$ is calculated again (red solid line in Fig. 4.7). Obviously this curve matches well with the experimental data. Within the Hirsch-model the O2 vacancies are generated predominantly in the neighborhood of the doped Ce atom. This would lead to a decreasing value of $|\Delta H_0[\mathrm{O2}]|$ with increasing doping level x. According to the experimental determination of $|\Delta H_0[\mathrm{O2}]|$ it is shown that this contribution is smaller compared to the contribution of the diminishing bondlength mismatch with increasing x.
The above mentioned scenario was also used by Manthiram *et al.* [219] to explain why it is not possible to reduce the excess oxygen in the $Gd_{1.85}Ce_{0.15}CuO_{4+\delta}$-system by the reduction process. Gd has the smallest ionic radius within the lanthanides (RE = La, Pr, Nd, Sm, Eu, Gd) and therefore the in-plane lattice parameter a of $Gd_{2-x}Ce_xCuO_{4+\delta}$ is smallest[1] amongst them ($a \approx 3.90$ Å). So, the tensile strength between the

[1] A larger in-plane lattice constant improves superconductivity [234].

CuO_2-plane and the $(REO)_2$-interlayer is so small, that it is not possible to create O2-vacancies. Moreover, the utmost reduction temperature is about $\approx 620°C$ at $p_{O_2} \approx 10^{-8}$ Torr, and for higher temperatures, the sample starts decomposing.
Still, there remains another question about the doping dependency of $|\Delta H_0[\mathrm{Oi}]|$, but this is almost unknown. The Oi-position lies between the CuO_2-plane and the $(REO)_2$ interlayer and affects the strength in both directions. Moreover, the occupation of Oi-site is strongly correlated to the valency of O^{z-} (equation 4.5 and 4.6). But the evacuation of the Oi-position is an exothermal process and therefore it is assumed, that a reduction temperature of 800°C and low oxygen partial pressure $p_{O_2} < 10^{-1}$ mbar leads to almost empty Oi-positions. Measuring the oxygen content of an as-grown sample for all doping levels x, δ was found to be ≈ 0.01. Therefore one may assume, that the contribution of $n[\mathrm{Oi}](x)$ to δ is almost Ce-independent (equation 4.9, green dotted line in Fig. 4.7).
To sum up, it was shown that the decrease of $|\Delta\delta|$ is mainly due to a decreasing amount of O2-vacancies. The doping dependence of the Oi-occupation still remains unknown.
However, in a combined thermodynamic and neutron scattering study performed by Petrov *et al.* [227] on $Nd_{1.9}Ce_{0.1}CuO_4$ a slightly different scenario for the reduction process was concluded. According to their results, at almost atmospheric pressure, $Nd_{1.9}Ce_{0.1}CuO_4$ was an oxygen-excess oxide. The transformation from an oxygen-excess oxide to an oxygen-deficient oxide occurred at high temperature and low oxygen pressure. The structure refinements clearly indicate that oxygen vacancies ($V_{O_{xx}}$), which occupy the O1 crystallographic positions, and interstitial oxygens (O_i^{yy}), which occupy the O3 position, are simultaneously present in the crystal structure. Gaseous oxygen intercalates into the $Nd_{1.9}Ce_{0.1}CuO_4$ structure by replacing the oxygen vacancies in the O1 position and the interstitial oxygen atoms in the O3 positions.

Overreduction

Finally, possibilities of crystalline modifications due to excessive reduction conditions are pointed out. It was found by VanAken *et al.* [235, 236] that extreme reduction conditions under H_2-atmosphere create a new phase in

the T′-system. In case of $x = 0$ the new phase $Nd_2CuO_{3.5}$ was identified belonging to the **B**mmm space group with lattice parameters $a = 4.18\,\text{Å}$, $b = 3.74\,\text{Å}$and $c = 11.74\,\text{Å}$. But this phase was identified by Kim *et al.* [203] as the $NdCuO_2$-impurity phase[2]. In the case of $x > 0$ strong reduction conditions lead to a phase separation of an orthorhombic Ce-poor phase and a tetragonal Ce-rich phase [238, 239]. Simultaneously, Cu-poor impurity phases are also found under strong reduction conditions, indicating that, the system starts decomposing by the loss of Cu due to re-evaporation from the film.

Summary of the reduction process

Recapitulating the impact of oxygen to the electronic properties of the electron doped high-temperature superconductors, it is shown that the as-grown samples contains interstitial Oi oxygen atoms. Presumably, these are acting as scattering centers suppressing the superconducting transition. The reduction process evacuates the Oi-sites thereby simultaneously generating O2 vacancies. The amount of vacancies is doping level dependent and changes between 0.1 for the non-doped sample towards 0.01 for $x = 0.15$.

Experimental approach

The above demonstrated impact of the reduction process on δ in the T′-system was derived in the thermodynamic equilibrium. Therefore, a certain time of reduction was assumed, creating a homogeneous oxygen distribution in the sample. In the real experimental scenario the following aspects needs attention:

1. How long is the reduction time t in order to achieve a minimum of apical interstitial oxygen for low temperatures ($T < 700°\text{C}$)?

2. What is the utmost reduction temperature preventing the destruction of the sample? Therefore, a phase diagram of stability of the $RE_{2-x}Ce_xCuO_{4+\delta}$-system is required.

[2] This phase, the so-called `delafossite`-structure, was investigated by Haas *et al.* [188]. Synthesis of delafossite-derived phases was done by Isawa *et al.* [237].

In the following the diffusion of O2-oxygen vacancies and interstitial Oi oxygen atoms is considered. Generally, diffusion is given by Fick s 2nd. law:

$$\frac{dn}{dt} = D \cdot \triangle n \tag{4.11}$$

where n describes the diffusion of O2-vacancies $n[V\{\mathrm{O2}\}]$ or Oi-diffusion $n[\mathrm{O}^{z-}]$. Due to the anisotropy of the T′-system, equation 4.11 has to be considered for tetragonal systems. Therefore one gets two equations, one for the diffusion along the a-direction (diffusion coefficient D_a) and the other one for the diffusion along the c-direction (diffusion coefficient D_c). A microscopic view of the diffusion process of the O2-vacancies and the interstitial Oi oxygen is given in Fig. 4.10. Along the a-direction the diffusion pro-

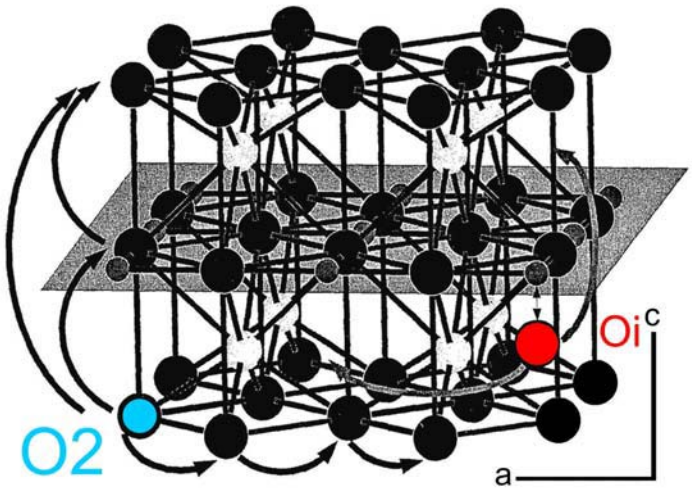

Fig. 4.10: Diffusion of O2-vacancies and interstitial Oi oxygen through the lattice. Due to the tetragonal anisotropy one has to distinguish between diffusion along the a- and along the c-direction. Along the c-direction the CuO_2 planes are limiting the velocity. Along the a-direction diffusion occurs due to hopping processes.

cess of the O2-vacancies is a simple hopping process towards neighboring O2-positions. Identical process powers the Oi-oxygen along the a-direction. Hence, recombination processes between O2 and Oi is also possible. Along the c-direction the diffusion process is powered by the so-called interstitial-mechanism. An O1-ion, whose chemical binding energy is higher than the O2-ion, is shifted to a O2-vacancy and simultaneously an O2-atom from the

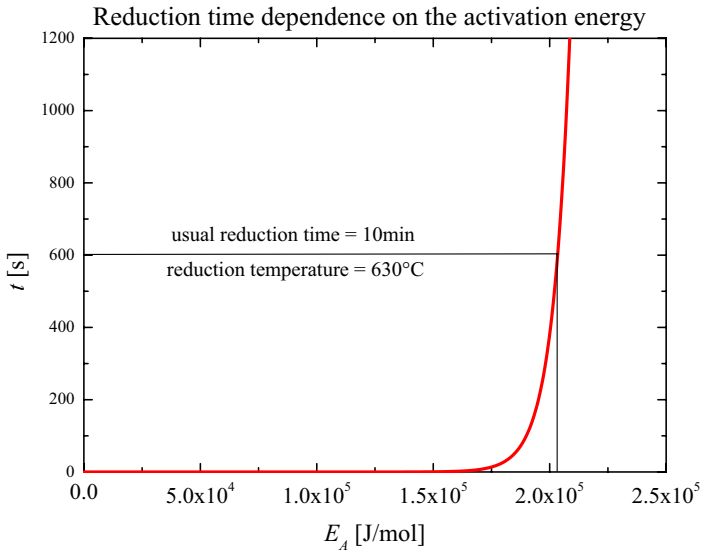

Fig. 4.11: For a given set of parameters ($l_c = 1000\,\text{Å}$, $T = 900\,\text{K}$) the red line shows the strong dependency on the activation energy E_A.

neighboring $(REO)_2$-interlayer is shifted towards the O1-site. So, the O2-vacancy crossed the CuO_2-plane. In a very similar way the diffusion of the Oi along the c-direction occurs. In this picture the activation energy along the c-direction is expected to be higher than along the a-direction because CuO_2-planes are acting like a barrier. In general the oxygen diffusion in the T′-compounds is described as a thermal activated process [240]. The diffusion coefficient follows an Arrhenius-type law:

$$D(T) = D_0 \cdot e^{-\frac{E_A}{RT}} \tag{4.12}$$

Idemoto *et al.* [241] determined the diffusion coefficients D_a and D_c and the results are given in table 4.2. It should be mentioned that in the case of the single crystal there is only a factor 2.5 between the two diffusion coefficients. This is interpreted that the diffusion along the c-direction does not occur through the CuO_2-planes but parallel to them. The transport through the planes may occur due to crystalline miss-orientation. The diffusion coefficient for the polycrystalline sample is given by the values of the single crystal as follows:

$$D_{poly} = \frac{2}{3}D_a + \frac{1}{3}D_c \tag{4.13}$$

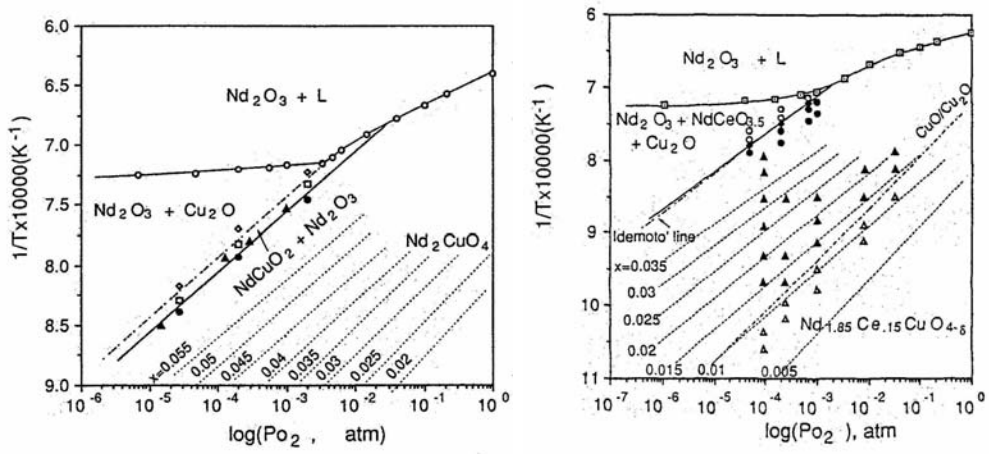

Fig. 4.12: Phase stability diagram for the T′-structure in the $Nd_2CuO_{4+\delta}$ and $Nd_{1.85}Ce_{0.15}CuO_{4+\delta}$ system. The dotted lines correspond to different oxygen contents δ. From [203].

	single crystal	poly crystal
$D_0 \left[\frac{\mathrm{cm}^2}{\mathrm{s}}\right]$	(a) 0.240 (c) 0.099	0.196
$E_A \left[\frac{\mathrm{kJ}}{\mathrm{mol}}\right]$	(a) 88 (c) 88	75

Tab. 4.2: Oxygen diffusion coefficient of the $Nd_2CuO_{4+\delta}$-system. Within the experimental setup it is not possible to distinguish between O2- and Oi vacancies.

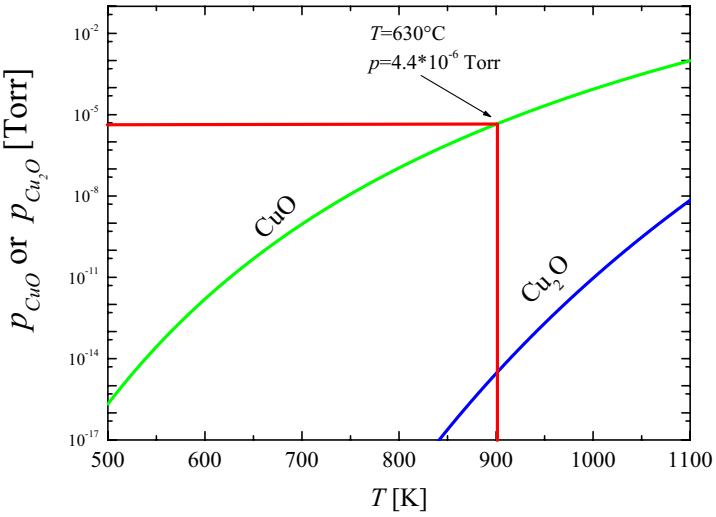

Fig. 4.13: Temperature dependence of the evaporation pressure of CuO and Cu_2O.

In the following, a solution of the diffusion equation 4.11 is derived for the case of thin films. Typical dimensions of the samples are: $l_a \approx 3\,\text{mm}$, $l_b \approx 6\,\text{mm}$ and $l_c \approx 1{\cdot}10^{-4}\,\text{mm}$. Although the diffusion coefficient D_c is 2.5 times smaller than D_a, it is sufficient to consider only the diffusion along the c-direction due to the difference of the dimensions by a factor $2 \cdot 10^4$. A solution of equation 4.11 for the O2-vacancy occupation is as follows:

$$n(z,t) = -n_0 + \frac{4n_0}{\pi} \sum_{k=2n+1} \frac{1}{k} \sin\left(\frac{k\pi z}{l_c}\right) \cdot e^{-\left(\frac{k\pi}{l_c}\right)^2 \cdot D_{\text{O2}} \cdot t} \tag{4.14}$$

and for the interstitial Oi occupation:

$$n(z,t) = \frac{4n_0}{\pi} \sum_{k=2n+1} \frac{1}{k} \sin\left(\frac{k\pi z}{l_c}\right) \cdot e^{-\left(\frac{k\pi}{l_c}\right)^2 \cdot D_{\text{Oi}} \cdot t} \tag{4.15}$$

The exponential function of equation 4.14 and 4.15 contains the product $P = \frac{Dt}{l_c^2}$. In order to achieve an almost homogeneous oxygen distribution along the c-direction $P > 1$ or

$$D_0 e^{-\frac{E_A}{RT}} \cdot t > l_c^2 \tag{4.16}$$

should be fulfilled. According to equation 4.16 the required reduction time for a thin c-axis oriented film at $T = 900\,\mathrm{K}$ is less than $10^{-4}\,\mathrm{s}$. Assuming, that the activation energy in equation 4.16 plays an essential role it is shown in Fig. 4.11 the reduction time dependence on the activation energy E_a for a given temperature.

One can easily recognize, that an increase of only 10% of the activation energy E_A multiplies the reduction time.
In this work the reduction time dependence for the T′-system for different RE = Pr, Sm, Eu, Gd and doping levels was investigated.
In order to generate a large oxygen deficit δ in the T′-system high reduction temperatures and a low oxygen partial pressure are required. Moreover, using higher reduction temperatures the reduction time decreases. But, there are limits of the reduction temperature due to the stability limit of the T′-compounds. In Fig. 4.12 the two phase diagrams for $Nd_2CuO_{4+\delta}$ and $Nd_{1.85}Ce_{0.15}CuO_{4+\delta}$ are given [203].

The phase stability line for $Nd_2CuO_{4+\delta}$ is given through:

$$\log p_{O_2}(atm) \approx \frac{-18930}{T} + 11.26 \tag{4.17}$$

and for $Nd_{1.85}Ce_{0.15}CuO_{4+\delta}$ through:

$$\log p_{O_2}(atm) \approx \frac{-19520}{T} + 10.95 \tag{4.18}$$

Subasri *et al.* [242] investigated the $Sm_2CuO_{4+\delta}$-system and found the phase stability diagram of Fig. 4.14 The phase stability line for $Sm_2CuO_{4+\delta}$ is given through:

$$\log p_{O_2}(atm) \approx \frac{-13285}{T} + 9.5988 \tag{4.19}$$

Phase stability criteria for Ce doped $Sm_2CuO_{4+\delta}$ have not been found in literature. Also no data for RE = Pr are available. However, with these three different stability lines one may recognize a trend-line for different doping levels and different rare earth element like RE = Pr or Gd.
The difference between the non-doped and the doped $Nd_2CuO_{4+\delta}$ stability line shows a shift towards higher activation energy levels and so an extension of the stability range with increasing doping level x. By comparing the $Nd_2CuO_{4+\delta}$ and the $Sm_2CuO_{4+\delta}$ stability lines, the stability range decreases. In other words, if this trend is extended to the lanthanides RE = La, Pr, Nd, Sm, Eu and Gd the phase stability line is higher for RE = Pr than

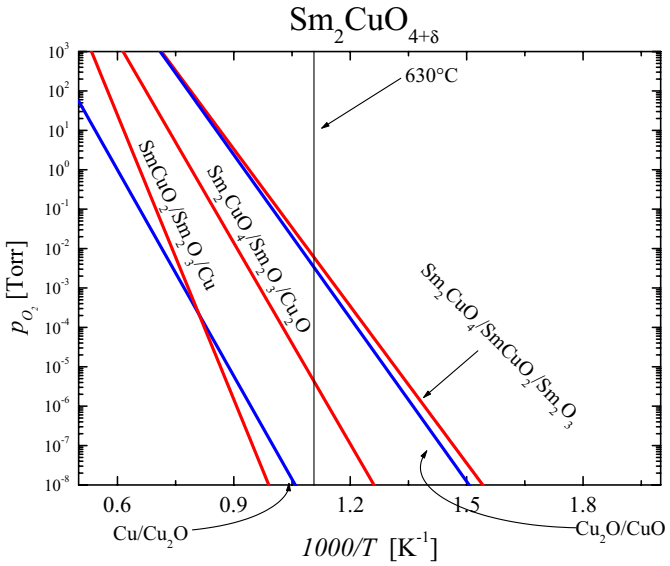

Fig. 4.14: Phase stability diagram for the T′-structure in the $Sm_2CuO_{4+\delta}$ system. For comparison the $Cu/Cu_2O/CuO$ stability lines are included. From [242].

for RE = Eu, Gd. According to the experimental results this prediction seems to be true. A reason for this behavior is that the diffusion coefficient D_c decreases with increasing ionic radii. The oxygen diffusion in the lattice affects mainly the decomposition process [243, 244, 245]. If a maximum of oxygen deficit δ is achieved, the decomposition process starts and CuO evaporates from the sample[3]. This is most likely due to the fact, that the p_{O_2} in our case is roughly 10^{-8} Torr. In Fig. 4.13 the temperature dependence of the evaporation pressure of CuO and Cu_2O are plotted.
The oxygen partial pressure dependence of the variation of the oxygen content of the $RE_{2-x}Ce_xCuO_{4+\delta}$ samples is shown in Fig. 4.2 for $x = 0$ and $x = 0.15$ in the case of RE = Nd. According to equation 4.4 and 4.6, δ is proportional to $p_{O_2}^{\xi}$. Therefore ξ changes almost linear from $-\frac{1}{6}$ for $x = 0$ towards $-\frac{1}{2}$ for $x = 0.17$. This doping dependence was also found by Yamaguchi *et al.* [247].
In summary, the as-grown electron doped T′ structure contains excess oxygen at interstitial sites (Oi) acting as scattering centers and thereby suppressing the superconductivity. The reduction process evacuates the interstitial sites.

[3] Investigations of the reduction process by Raman-spectroscopy proposed, that only the O1 position is evacuated [246].

The doping dependence of Oi of the as-grown and reduced $RE_{2-x}Ce_xCuO_{4+\delta}$ is almost unknown.
However, recent experiments suggest, that interstitial apical oxygen stabilizes long-range antiferromagnetic order [248].

5

Properties of epitaxial thin films of electron-doped cuprates

In chapter 3 the growth of epitaxial thin films of cuprates with T′ structure has been discussed. It was shown, that growth and annealing conditions are not independent of the cerium content or the choice of the rare earth element. RHEED, EIES and mass-spectrometer were used to improve the crystallinity of thin films significantly.
Since the reactive molecular beam epitaxy technique allows stabilizing phases that are not accessible in bulk samples (due to low growth temperatures), a real enrichment to the general accepted phase diagram of electron doped cuprates could be achieved.

5.1 Resistivity measurements and structural characterization

Compared to a simple metal, the electrical properties of oxides show certain characteristic features. One is the metal-insulator transition [249], in which at a certain temperature or pressure, an insulator turns to a metal. The word transition is usually used even when this change occurs at a certain composition. This phenomena has attracted much attention and was the most popular research theme before high-temperature superconductivity exploded onto the scene. The mechanism of the transition is not simple and the phenomena itself seems to become more and more complex as research progresses. It is a result of many electron-electron and/or electron-phonon interactions.
Another characteristic feature of oxide conductivity is a temperature de-

pendence of the resistivity that is stronger than T^1. This is mostly due to scattering by optical phonons but for certain transition element oxides, such as cuprates, electron-electron scattering is by far not negligible. In transition-metal oxides, the conduction bands are mostly formed with oxygen $2p$- and metal d-orbitals. The s-electrons enter into deeper bonding orbitals. The oxygen orbitals are usually located lower in energy, which leads to the observed ionicity. At the same time, the directionality of the p- and d-orbitals, and the strong Coulomb interaction in the d-orbital cloud manifest more directly in the transport phenomena, whereas in the simple metals, s-orbitals are the main constituent of the conduction band. The stronger atomic-electron-like character of the conduction electrons induces a complex many-body aspect in the oxides.
Resistivity measurements are one of major characterization techniques used in the present study. One can easily distinguish between fundamental material properties as there are:

- T_c or no T_c
- insulating or metallic behavior

From these resistivity measurements ($\rho(T)$) superconducting phase diagrams for the different $RE_{2-x}Ce_xCuO_4$ are constructed. These phase diagrams are one of the main achievements in this work and lead to more in-depth understanding on the underlying physics of electron doped cuprate superconductors.
Figure 5.1 shows the temperature dependent resistivity behavior for thin films of $Pr_{2-x}Ce_xCuO_4$ grown on (001)$SrTiO_3$ irrespective of the doping level x and the annealing condition. This illustration should provide an impression of the abundance of $Pr_{2-x}Ce_xCuO_4$. The room temperature resistivity value ranges over three orders of magnitude. Moreover, pure metallic behavior, superconductivity, insulating and semiconducting behaviors are all present for this single compound with two free parameters:

- cerium content (doping level)
- interstitial oxygen

In particular, the drastic impact of interstitial oxygen on transport and superconducting properties can be seen from Fig. 4.1. The influence of apical

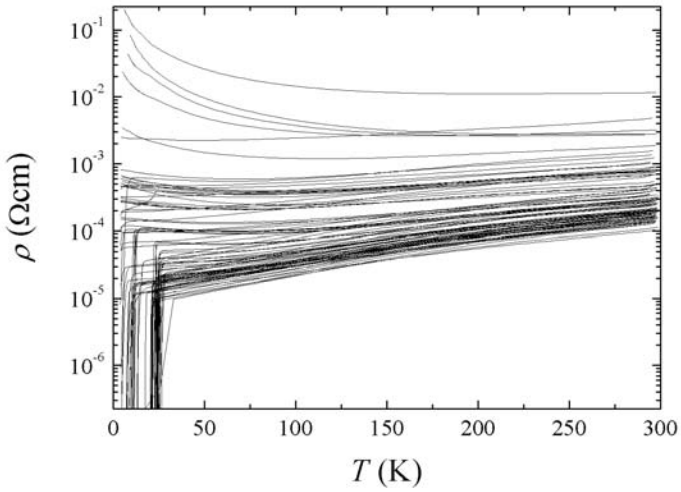

Fig. 5.1: Temperature dependent resistivity for epitaxially, single phase thin films of $Pr_{2-x}Ce_xCuO_4$ on (001)$SrTiO_3$.

oxygen to the Hall coefficient (Fig. 4.4) is significant. Even since the algebraic sign of the hall coefficient is affected by interstitial oxygen, its impact on superconductivity still remains unclear. However, a recent investigation on PCCO thin films [250] emphasized its role as a scattering center.
In order to derive a phase diagram of electron doped cuprates with the stoichiometric formula $RE_{2-x}Ce_xCuO_4$, the impact of the interstitial or apical oxygen should be zero. Since a precise determination of the oxygen content in thin films is not an easy task, the only creditable method remains by following the thermodynamic stability lines as it was discussed in Chapter 3.4.1. Thin films treated by optimized reduction will be considered for evaluating the superconducting phase diagrams[1]. It is worth to mention, that the determination of T_c is by far not unique. In the present study, a critical temperature is termed T_c^0, when the resistivity value drops below 10^{-6} mΩcm. No other temperatures (e.g., onset-T_c) will be considered.
Crystalline information of the grown thin films is integrant for there investigation. X-ray diffraction provides details about the crystallinity, impurity

[1] According to results obtained by Maiser *et al* [251], pulsed laser deposition technique seems to be not appropriate for the synthesis of electron-doped cuprate superconductors.

phases and lattice parameters. Therefore, all thin film samples have been characterized by a two circle `Rigaku` RX2400 x-ray diffractometer. Moreover, the in-plane lattice constants have been measured on a four-circle `Bruker` Advanced D8 x-ray diffractometer. The lattice parameters have been calculated using the Nelson-Riley method[252]. As a result, c-axis lengths values called c_0 and a-axis lengths values called a_0 are obtained. The advantage of the Nelson-Riley method is, that the obtained values for the lattice parameters are highly precise[2]. High precession is necessary, since the changes in the lattice parameters due to doping are small (e.g., $\Delta c \approx 0.01\,\text{Å}$).
Since the rare earth ion and cerium ions in $RE_{2-x}Ce_xCuO_4$ form a solid solution, the c-axis should monotonically decrease by increasing the cerium concentration. Moreover, apical oxygen is found to enlarge the c-axis length. In connection with resistivity measurements, this will provide new information on the physics of interstitial oxygen.

5.1.1 Thin films of $Pr_{2-x}Ce_xCuO_4$

The majority of experiments have been performed on the investigation of $Pr_{2-x}Ce_xCuO_4$ grown on (001)$SrTiO_3$ substrates. The doping dependent c_0 values of all grown $Pr_{2-x}Ce_xCuO_4$ samples are given in Fig. 5.2. The doping-level x is already corrected by the result of the ICP-analysis. A linear least square fit to the $Pr_{2-x}Ce_xCuO_4$ data gives

$$c_0(x) = 12.2347 - 0.5406 \cdot x \tag{5.1}$$

The slope found by the experiment also contains the change of the Cu-valency due to the doping effect. The problem one has to deal with is, that the valency of copper also changes by doping and oxidation effectiveness [255]. In this context, the average ionization potential changes. In order to avoid these problems Huang *et al.* [218] compared the doping dependence of the c-axis value of the $Nd_{2-x}Ce_xCuO_4$-system with the $Nd_{2-x}Th_xCuO_4$-system. Herein it was assumed that the valency of Th is exactly 4+. As a result, an average Ce valency of +3.84 was derived.
Within the doping range $0 < x < 0.21$, the data points match quite well with the linearly fitted curve. For a given doping level x, several data points

[2] Applying the Nelson-Riley function on peak positions measured with typical machine accuracy of $\pm 10^{-3}\,^\circ$, the typical error in d-spacing is of the order of $\pm 10^{-4}$ Å. Therefore, the error-bars vanish within the dimensions of the data point.

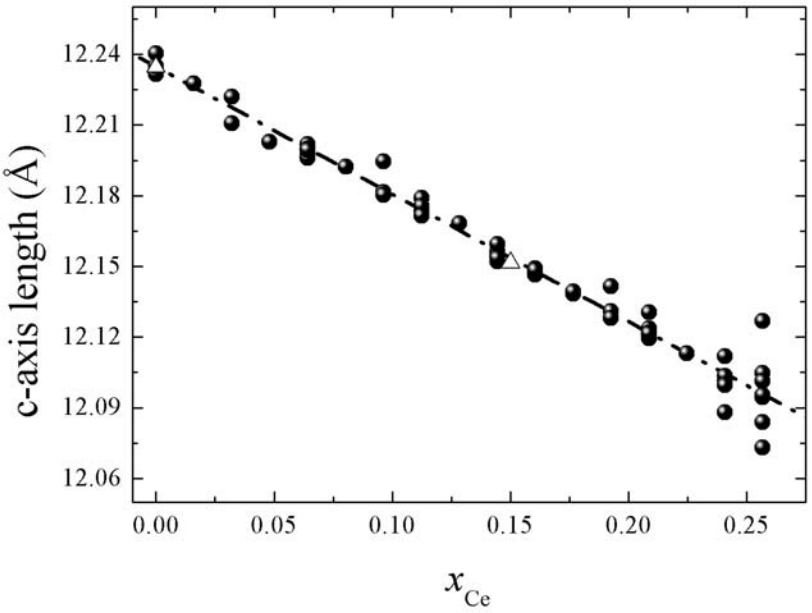

Fig. 5.2: c-axis lattice parameter of $Pr_{2-x}Ce_xCuO_4$ vs. doping. The straight line is a linear least square fit to the data points (spheres). Triangular data points are taken from Uzumaki *et al.* [253, 254].

from various reduction conditions are included. Including data for various reduction conditions, the general trend line is scarcely affected although optimally reduced $Pr_{2-x}Ce_xCuO_4$ thin films have smaller c-axis length (see Chapter 5.1.6). Approaching higher doping levels $x > 0.22$, the deviation from the linear fit increases. This behavior is a clear indicator for the solubility limit of Ce in the $Pr_{2-x}Ce_xCuO_4$-system.
For the determination of the in-plane lattice parameter a_0, the (103), (206) and (309) reflections have been used[3] since these planes have the highest reflection rate. In Fig. 5.3 the a_0-lengths versus cerium concentration are plotted. Although the cerium concentration increases, no clear trend line can be deduced for the in-plane lattice constant being suggestive for a con-

[3] The distance d is also calculated by the Nelson-Riley formalism using the tetragonal relation $\frac{1}{d^2} = \frac{h^2+k^2}{a^2} + \frac{l^2}{c^2}$.

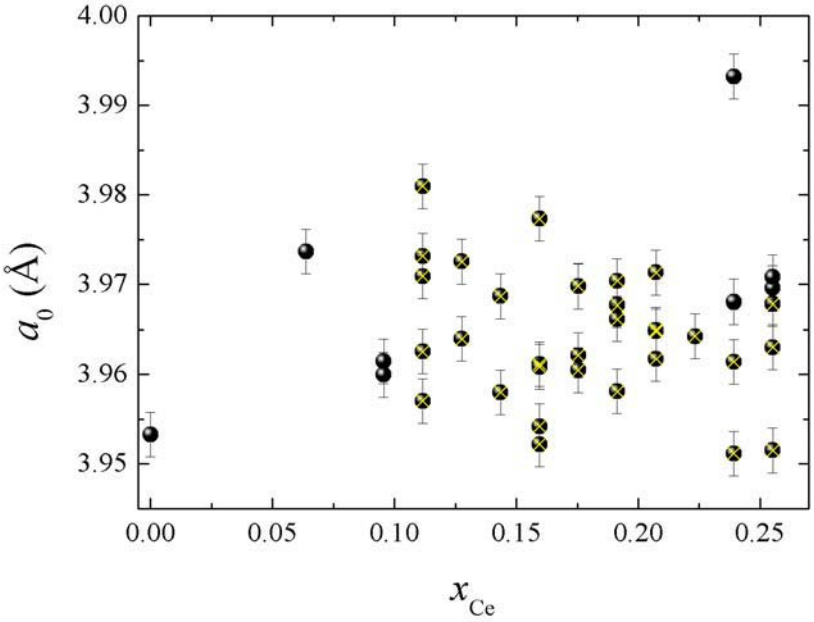

Fig. 5.3: In-plane lattice constant of $Pr_{2-x}Ce_xCuO_4$ thin films grown on (001)$SrTiO_3$ substrates. Points marked with a cross correspond to superconducting samples.

stant or doping-independent in-plane lattice length of $a \approx 3.96\,\text{Å}$. Moreover, even if one only considers superconducting samples (marked by a cross in Fig. 5.3), the in-plane lattice length seems to be independent of the cerium concentration. In addition, a constant in-plane lattice constant is also suggestive taking only optimally reduced samples into account.

As it is mentioned above, resistivity measurements have been utilized to determine the superconducting transition temperature T_c and the result is shown in Fig. 5.4. For cerium concentrations $0 < x < 0.1$, no superconducting transition has been observed. For $x > 0.1$, superconductivity rapidly sets in upon increasing the doping level. The highest superconducting transition temperature is found for $x = 0.135$ with $T_c = 26.4\,\text{K}$. This value is higher than any value reported in the literature [256, 257, 258, 259, 47, 260, 261, 200, 262, 251, 263, 109, 264, 265, 33, 266, 267, 138, 268, 269, 270, 271, 272, 273, 274, 275, 276, 277, 278]. The doping level, where T_c is highest is usually referred to as optimal doping level x_{opt}.

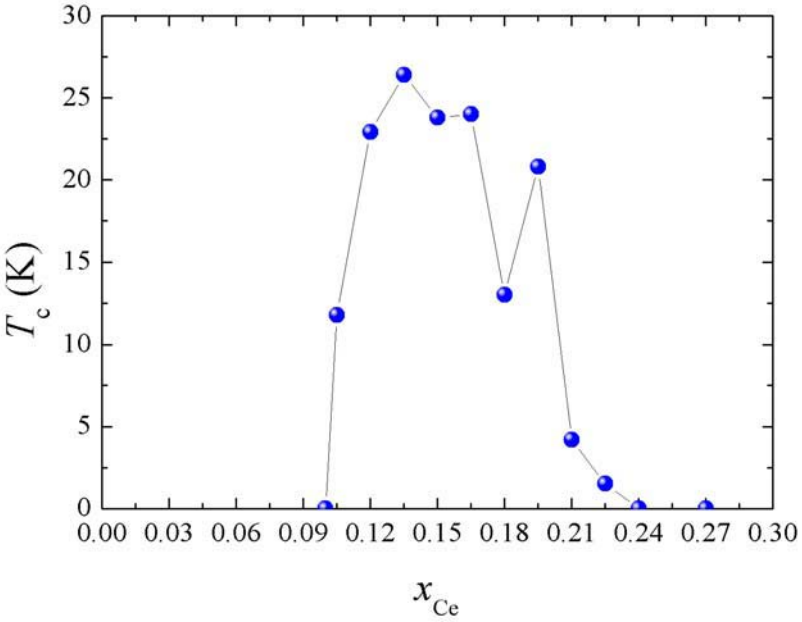

Fig. 5.4: Superconducting phase diagram obtained from single phase *c*-axis oriented thin films of $Pr_{2-x}Ce_xCuO_4$. Highest superconducting temperature is found around $x \approx 0.135$.

Higher doping levels suppress T_c and for cerium concentrations $x \geq 0.22$, superconductivity completely vanish. This behavior is associated to transport properties as it is shown in Fig. 5.5. The undoped compound Pr_2CuO_4 shows insulating rather than metallic behavior since the room temperature resistivity value is smaller than the value obtained at 30 K. Metallic behavior starts for cerium concentrations larger than $x = 0.05$ and persists up to doping levels $x = 0.25$, where the solubility limit of Ce has been reached.

Influence of the substrate

In the case of $Pr_{2-x}Ce_xCuO_4$, the influence of substrate material has been investigated. Within a single run, (110)$NdGaO_3$, (001)$SrTiO_3$, (110)$DyScO_3$, (110)$KTaO_3$ and (001)MgO substrates have been mounted on a substrate holder. It was found that, no T′-$Pr_{2-x}Ce_xCuO_4$ is forming on (110)$KTaO_3$ and (001)MgO substrates. Here it is assumed, that these materials do not

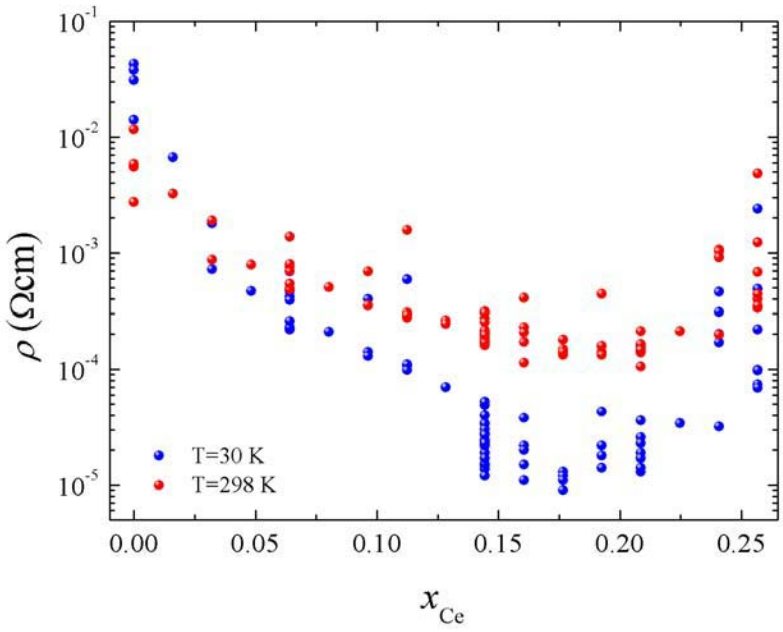

Fig. 5.5: Resistivity versus doping level x_{Ce} at room temperature (red dots) and 30 K (blue dots) obtained from single phase c-axis oriented thin films of $Pr_{2-x}Ce_xCuO_4$.

stand the growth conditions ($\vartheta_{substrate} \approx 700\,°C$, $p_{O_3} \approx 2 \cdot 10^{-6}$ Torr). However, results obtained for (110)$NdGaO_3$, (001)$SrTiO_3$ and (110)$DyScO_3$ are shown in Fig. 5.6. For (110)$NdGaO_3$ the sample shows the highest resistivity and the lowest superconducting transition temperature. In the case of (110)$DyScO_3$ the transition temperature was found to be highest among these three samples. This is also correlated to the observed crystallinity, which is plotted in the inset of Fig. 5.6. When the crystallinity increases, the superconducting temperature increases and the resistivity decreases.

Influence of annealing time

Considering the $T_c(x)$-dependency in Fig. 5.4 together with the resistivity behavior in Fig. 5.5 one can easily recognize, that there is a wide range for T_c for $x \approx 0.105$, the borderline to non-superconducting behavior.
It was found that, this border is strongly affected and influenced by the reduc-

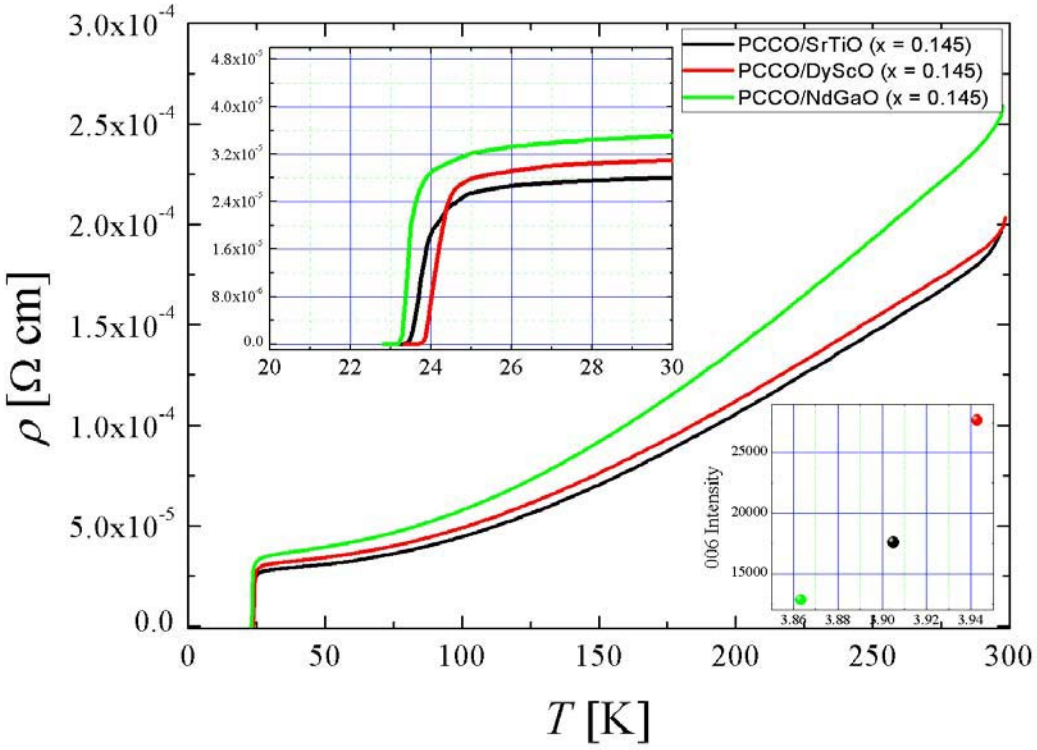

Fig. 5.6: Resistivity behavior of thin films of $Pr_{1.855}Ce_{0.145}CuO_4$ grown on three different substrates. (110)$NdGaO_3$, (110)$DyScO_3$, (001)$SrTiO_3$, (110)$KTaO_3$ and (001)MgO substrates were simultaneously mounted to the substrate holder within a single deposition. The left inset shows the enlarged region near the transition temperatures obtained for these three samples. The right inset plots the x-ray intensity of the (006)-peak of $Pr_{1.855}Ce_{0.145}CuO_4$ vs. the lattice constant of the substrate.

tion process. Therefore, an experiment on the reduction time was performed. In other words, the as-grown samples with equal doping levels (self-consistent with the c-axis value) were treated in reducing atmosphere at $\vartheta \approx 630°C$ for different periods of time. The result is presented in Fig. 5.7 (a). For the usual standard reduction time of 10 min T_c is very low ($\approx$ 2K). By doubling the reduction time under equal reduction conditions, the superconducting transition temperature abruptly changes to $T_c = 12\,K$. Further increasing of the reduction time suppresses the superconductivity and for $t = 720$ min even

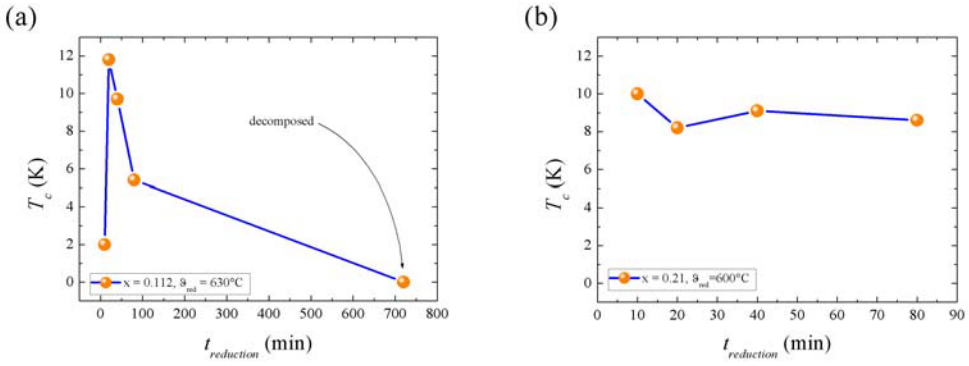

Fig. 5.7: Superconducting transition temperature obtained from thin films of $Pr_{1.888}Ce_{0.112}CuO_4$ (a) at different annealing times. When the sample was removed from the growth chamber, T_c is about 2 K. Within the standard annealing time, a superconducting transition temperature of up to 12 K can be achieved. If the sample is exposed longer to UHV atmosphere, decomposition starts appearing and T_c drops. For long annealing times (720 min), the sample was completely transparent (Pr_2O_3 and CeO_2 oxides have been formed due to decomposition). For overdoped thin films of $Pr_{1.79}Ce_{0.21}CuO_4$ (b), the annealing time is less critical compared to the underdoped case.

the sample decomposes. To give a possible explanation for this scenario one should think about the interstitial oxygen Oi in Chapter 4. It seems that with decreasing doping level the removal of apical oxygen becomes more difficult. On the other hand, with further reduction, T_c decreases because the reducing atmosphere (ϑ and p_{O_2}) is too strong and therefore the sample starts decomposing. The decomposition products are identified by X-Ray diffraction as delafossite compounds ($PrCuO_{2.5}$) and simple rare earth oxides.
Moreover, the almost same experiment was performed for an overdoped sample with $x = 0.21$ at $\vartheta \approx 600°C$. The result is shown in Fig. 5.7 (b). For high doping levels it seems that the influence of the reduction process on T_c is rather minor. The change in T_c is most likely due to different compositions rather than different reduction times. It should be mentioned, that the lower reduction temperature used for the high doping level is necessary because of the doping dependence of the phase stability.
In the present study, the influence of the reduction time on the lattice was also considered. The results are given in Fig. 5.8, showing a decreasing c-axis parameter with increasing reduction time $\vartheta_{reduction}$. In our present understanding, a decrease of the c-axis length is most likely due to the removal of

apical interstitial oxygen, which enlarges the lattice. This result is in sharp contrast to previous experiments on single crystalline $Nd_{2-x}Ce_xCuO_{4+\delta}$ by Pankov *et al.* [208] where an increase of *c*-axis parameter was found after the reduction process.

In this study, all thin films have been grown in our UHV reactive MBE

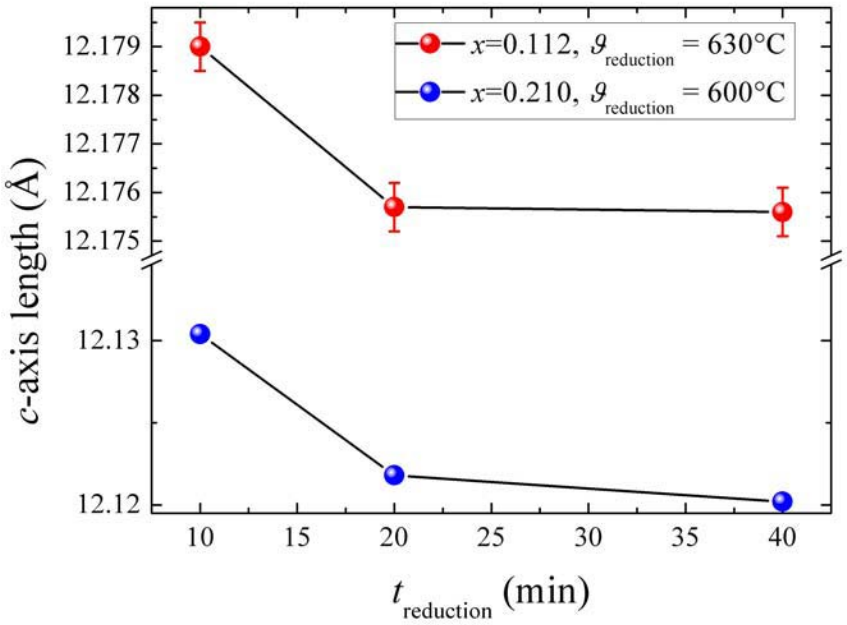

Fig. 5.8: *c*-axis length of under- and overdoped thin films of $Pr_{2-x}Ce_xCuO_4$ vs. reduction time. For the low-doping case, the shrinkage of the *c*-axis is one order of magnitude smaller compared to the overdoped sample. When the sample is treated in reducing atmosphere for longer than 20 min, the *c*-axis length remains constant.

chamber. Therefore, even if the annealing time is equal to zero, there is still a kind of pseudo-annealing since the sample cools in a UHV atmosphere. So, the change on *c*-axis as shown in Fig. 5.8 is tiny ($\Delta c \approx 0.003$ Å). In order to see a more pronounced change, a Pr_2CuO_4 thin film was annealed in ozone ($\approx 28\,\%$) atmosphere at ambient pressure at 300 °C for 24 h and than cooled to room temperature with 2 °C/min (annealing in ozone for 60 h do not change sample properties). The result obtained by this experiment is striking and in good agreement to experiments done by Yoshitake *et al.*

[279]. The c-axis length of the Pr_2CuO_4 thin film increased to $c \approx 12.273$ Å. From this dramatic change of almost 0.1 Å we speculate, that oxygen occupies more and more apical sites and therefore enlarges the c-axis. Moreover, the resistivity value at room temperature increased by more than four orders of magnitude. Later we will see, that this behavior is a general trend.

5.1.2 Thin films of $Sm_{2-x}Ce_xCuO_4$

The next candidate of electron doped cuprates, that has been investigated is $Sm_{2-x}Ce_xCuO_4$. However, up to now, there are no reports on the growth of $Sm_{2-x}Ce_xCuO_4$ thin films. The ionic radius of Sm^{3+} is 1.088 Å and therefore smaller than Pr^{3+}. Consequently, electronic properties are expected to be affected. $Sm_{2-x}Ce_xCuO_4$ thin films were grown on (001)$SrTiO_3$. Similar to

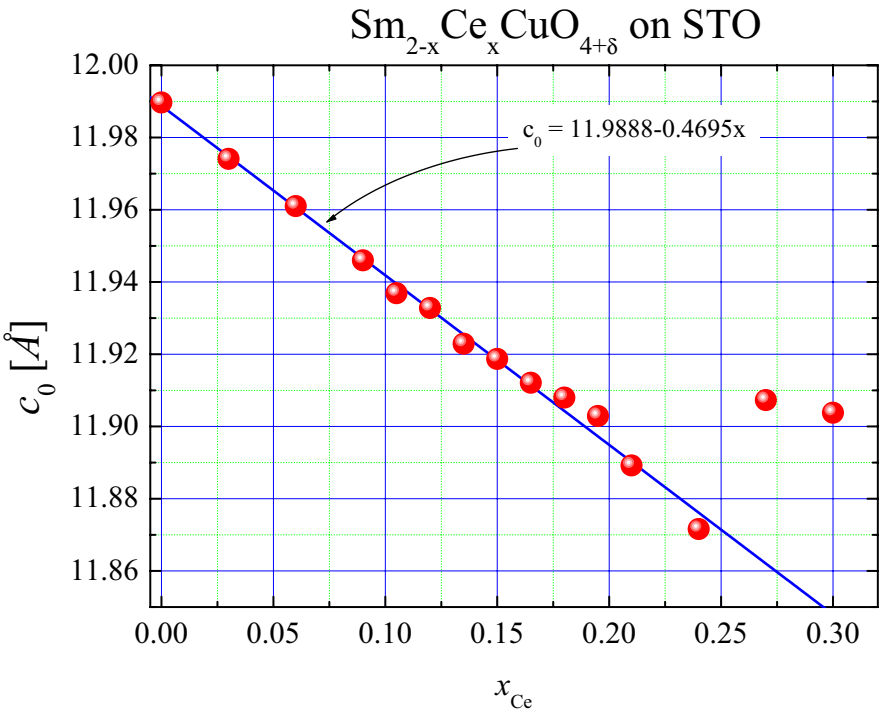

Fig. 5.9: c-axis length of thin films of $Sm_{2-x}Ce_xCuO_4$ vs. doping. Data points have been obtained from optimally reduced samples. The solubility limit of cerium is as high as $x \approx 0.23$. The blue line is a linear least square fit to the obtained data points.

$Pr_{2-x}Ce_xCuO_4$, same behavior of the c-axis length is found. Upon doping,

the c-axis length shrinks. In Fig. 5.9 the blue line is a linear least square fit to the data points. Compared to $Pr_{2-x}Ce_xCuO_4$ the slope became smaller which can be attributed to the fact that the ionic radius of Sm^{3+} is smaller compared to Pr^{3+} while the ionic radius of Ce^{4+} is still smaller (0.97 Å). In contrast to

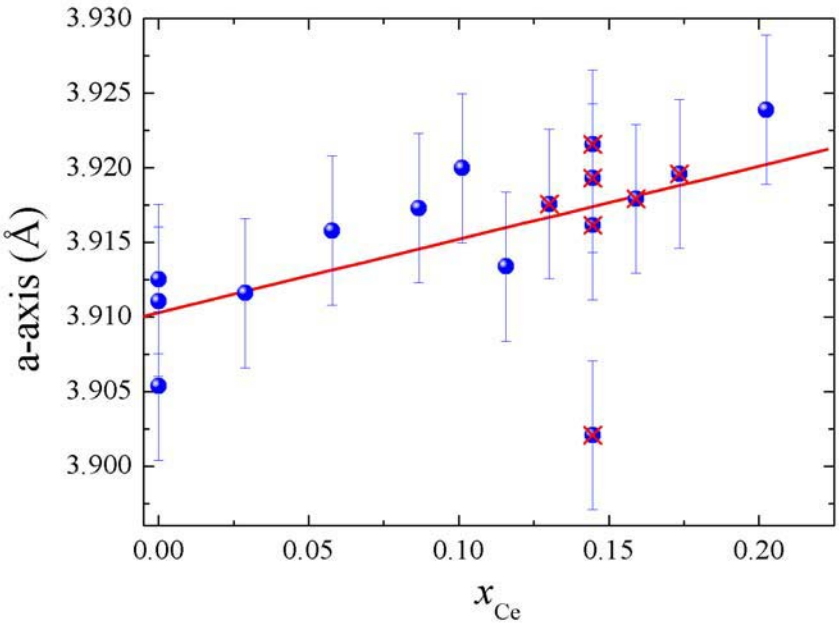

Fig. 5.10: a-axis length of single phase c-axis oriented thin films of $Sm_{2-x}Ce_xCuO_4$ vs. doping. a-axis lengths have been calculated from (103), (206) and (309) peaks and c-axis length. Upon doping the in-plane lattice (the Cu-O bond) increases. Superconducting samples are marked by a cross.

the doping-independent in-plane lattice constant a of $Pr_{2-x}Ce_xCuO_4$, lattice constant a of $Sm_{2-x}Ce_xCuO_4$ shows a positive slope with increasing x, as it is shown in Fig. 5.10. The linear least square fit

$$a(x) = 3.91 + 0.049 \cdot x \tag{5.2}$$

shows a positive slope upon doping. A positive slope indicates, that the Cu-O bond distance increases.

The superconducting phase diagram for $Sm_{2-x}Ce_xCuO_4$ thin films is plotted in Fig. 5.12. Here, the highest superconducting transition temperature was

found for $x \approx 0.150$ with $T_c \approx 19\,K$. This transition temperature is almost identical compared to the data reported by Nagata *et al.* [280]. However, in the case of Sm, superconductivity starts appearing for $x \approx 0.13$ which has not been reported so far [281, 259, 282, 283, 254, 284, 285, 286, 287, 183, 288, 289, 290]. On the higher doping side, superconductivity disappears for $x = 0.21$. The resistivity range at room temperature for $Sm_{2-x}Ce_xCuO_4$ thin

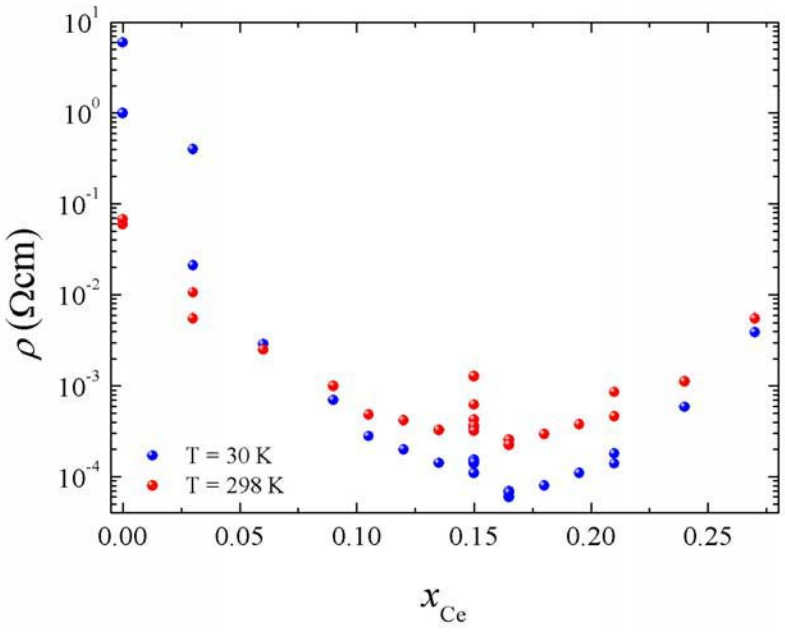

Fig. 5.11: Resistivity behavior at 30 K (blue points) and room temperature (red points) of thin films of $Sm_{2-x}Ce_xCuO_4$ vs. doping. Note, data points are obtained from optimally reduced samples.

films lies between 0.2 mΩcm and 100 mΩcm for optimally doped and undoped samples, respectively. At low temperature, the resistivity trend changes by less than one order of magnitude. Therefore, the residual resistivity ratio has a maximum around the optimally doped case, where $r = \frac{\rho_{298K}}{\rho_{30K}} \approx 4$. This value is by far smaller compared to r values of $Pr_{2-x}Ce_xCuO_4$. Since we can not consider crystallinity properties responsible, we may speculate that this drop of r-value is correlated to the crystallographic issues. The appearance of metallic behavior [291] sets in for $x \approx 0.09$, which is also larger when

compared to $Pr_{2-x}Ce_xCuO_4$. However, metallic behavior persists up to the solubility limit of Ce.

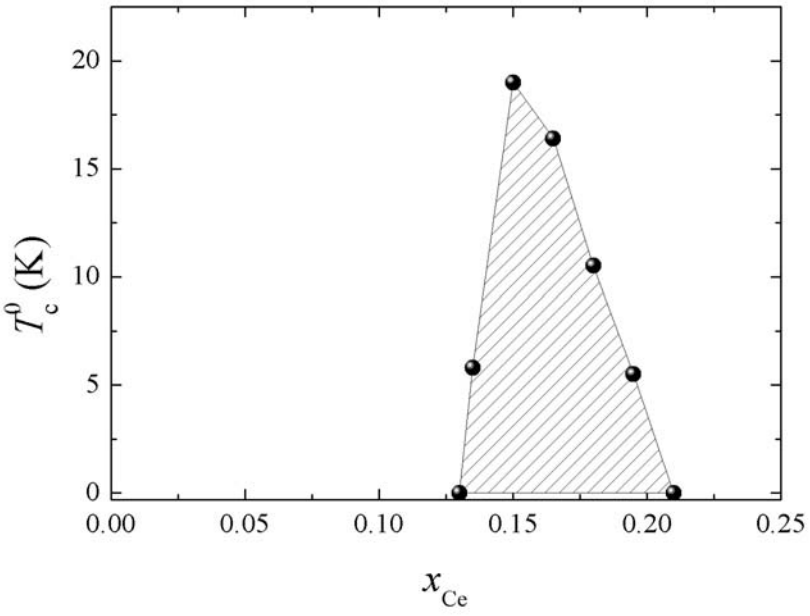

Fig. 5.12: Superconducting phase diagram obtained from resistivity measurements of $Sm_{2-x}Ce_xCuO_4$ thin films vs. doping. Maximum transition temperature is found at $x = 0.155$, where $T_c \approx 19.5\,K$. Superconductivity sets in for $x \approx 0.12$ and end for $x \approx 0.21$.

5.1.3 Thin films of $Eu_{2-x}Ce_xCuO_4$

The right hand side neighbor in the periodic table of Sm is Eu. However, there were also no reports on the synthesis of $Eu_{2-x}Ce_xCuO_4$ thin films in the literature so far. Shortly after electron doped cuprates have been found, Markert *et al.* [292] reported on superconductivity in $Eu_{2-x}Ce_xCuO_4$. The in-plane lattice parameter a in Fig. 5.14 almost shows no dependency upon doping. Although the a-axis of $Eu_{2-x}Ce_xCuO_4$ is smallest among all T′-structured cuprate superconductors, doping does not influence the Cu-O(1) binding length. The red line in Fig. 5.14 is a linear least-square fit giving

$$a \approx 3.90654 + 7.07447 \cdot 10^{-4} \cdot x_{Ce}. \tag{5.3}$$

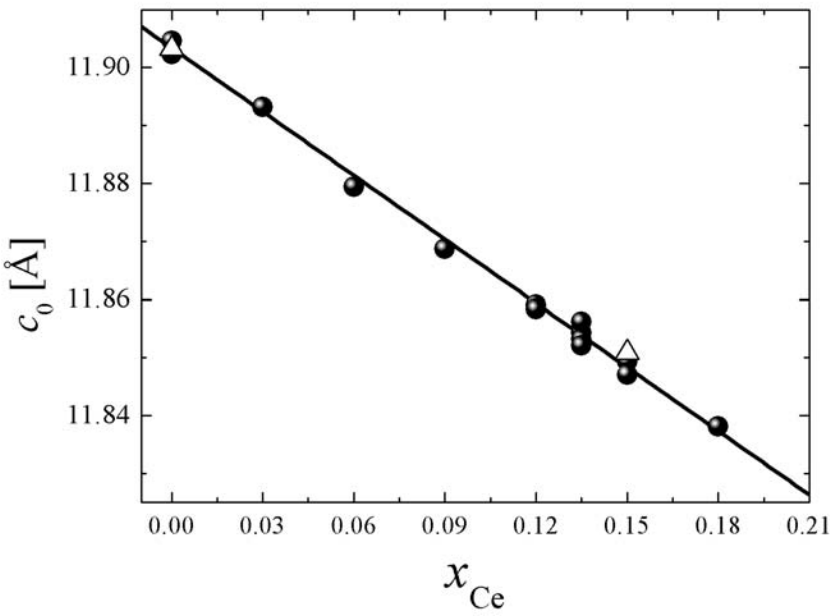

Fig. 5.13: c-axis lattice parameter $Eu_{2-x}Ce_xCuO_4$ vs. cerium content. The line is a linear least square fit to the data points (spheres). For comparison data points obtained by Uzumaki are included (triangle).

This observation slightly deviates from the results reported by Uzumaki *et al.* [253] where $a(x) \approx 3.9012 + 0.04333 \cdot x_{Ce}$. However, from this report it is not clear whether the undoped samples have been treated by a reduction treatment. Resistivity values vs. cerium content are plotted in Fig. 5.15 for room temperature (red points) and 30 K (blue points). Transport measurements of $Eu_{2-x}Ce_xCuO_4$ have not been reported so far [292, 293, 294]. There, the absolute value decreases by about two orders of magnitude from the undoped compound towards $x \approx 0.15$. Since Eu^{3+} is again smaller than Sm^{3+}, also the superconducting region became more limited. In the case of $Eu_{2-x}Ce_xCuO_4$ thin films, metallic behavior starts for as high cerium concentrations as $x \approx 0.1$ and remains up to the solubility limit of cerium. Hence, also the maximum achieved superconducting transition temperature now is $T_c \approx 12$ K which is significantly higher compared to results obtained by Markert *et al.* [292]. For cerium contents lower than $x \approx 0.16$ no super-

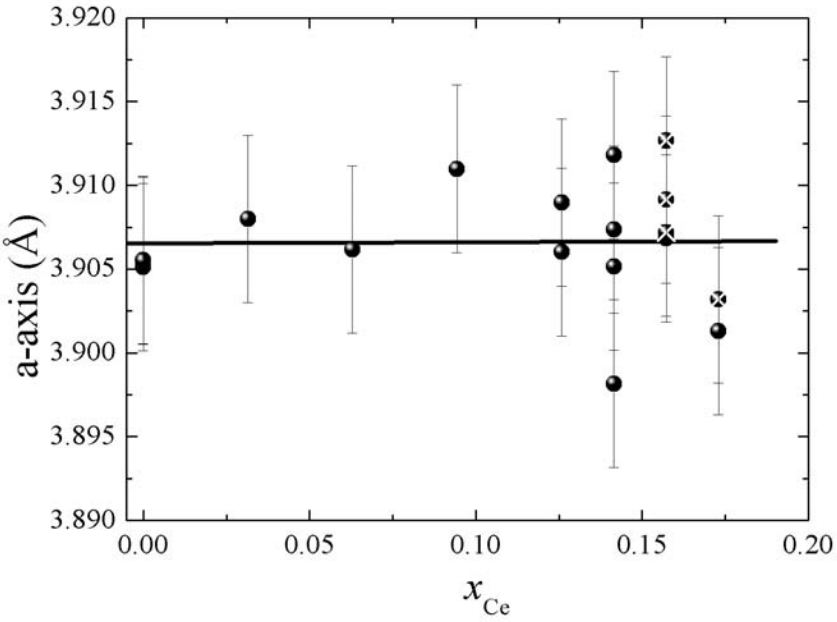

Fig. 5.14: *a*-axis length of single phase *c*-axis oriented thin films of $Eu_{2-x}Ce_xCuO_4$ vs. doping. *a*-axis lengths have been calculated from (103), (206) and (309) peaks and *c*-axis length. Upon doping the in-plane lattice (the Cu-O bond) increases. Superconducting samples are marked by a cross. The straight line is a least square linear fit to data points.

conductivity has been found. On higher doping side the limit for obtaining a superconducting thin film was found to be at $x = 0.19$.

5.1.4 Thin films of $La_{2-x}Ce_xCuO_4$

As discussed before, (see also Fig. 3.19), growth temperatures as low as 350 °C are required to stabilize $La_{2-x}Ce_xCuO_4$ in the Nd_2CuO_4-structure as powder or crystal material. Such low synthesis temperatures can be easily realized when thin films are grown in a UHV chamber. $La_{2-x}Ce_xCuO_4$ has been grown on (001)$SrTiO_3$ substrates. For the present investigation, a constant film thickness of 1000 Å was chosen. The ionic radius of eight-fold coordinated La^{3+} is 1.16 Å. This is significantly smaller compared to the T-structured analogues where La occupies a nine-fold coordinated site and

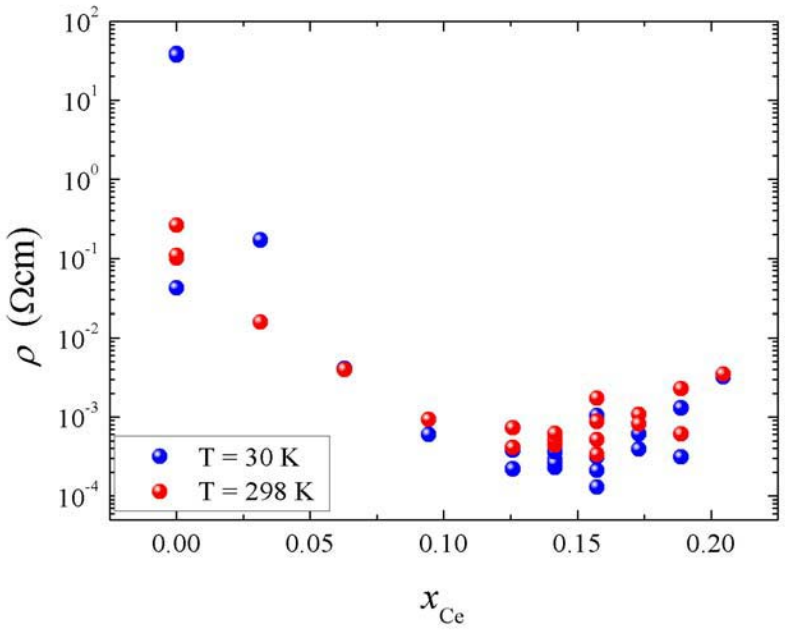

Fig. 5.15: Resistivity behavior at 30 K (blue points) and room temperature (red points) of thin films of $Eu_{2-x}Ce_xCuO_4$ grown on (001)$SrTiO_3$ vs. cerium content.

therefore the ionic radius becomes 1.216 Å(Table 3.1). Here it is necessary to bear in mind that the physics of thin film growth is far off the thermodynamical limit and therefore one can not easily adopt growth parameters like temperature directly from bulk synthesize methods. Typical growth temperatures for the synthesis of $La_{2-x}Ce_xCuO_4$ thin films are around 700 °C at ozone pressures of approx. $2 \cdot 10^{-6}$ Torr. Since Ce^{4+} has ionic radius of 0.97 Å and La^{3+} about 1.16 Å the *c*-axis shrinks upon doping. This is shown in Fig. 5.18, where points are included irrespective of growth- and annealing conditions.

In contrast to other Nd_2CuO_4-structured compounds the crystallinity for $La_{2-x}Ce_xCuO_4$ plays a crucial role. For $La_{2-x}Ce_xCuO_4$ the undoped compound ($x = 0$) shows poor crystallinity. Since film thicknesses deviate only approx. ±50 Å we use the intensity criteria of the (006) peak. As it was shown already by Naito *et al.* [295] for doping independent growth temperatures a phase jump occurs around $x_{Ce} \approx 0.06$ from T′-$La_{1.94}Ce_{0.06}CuO_4$ to T-

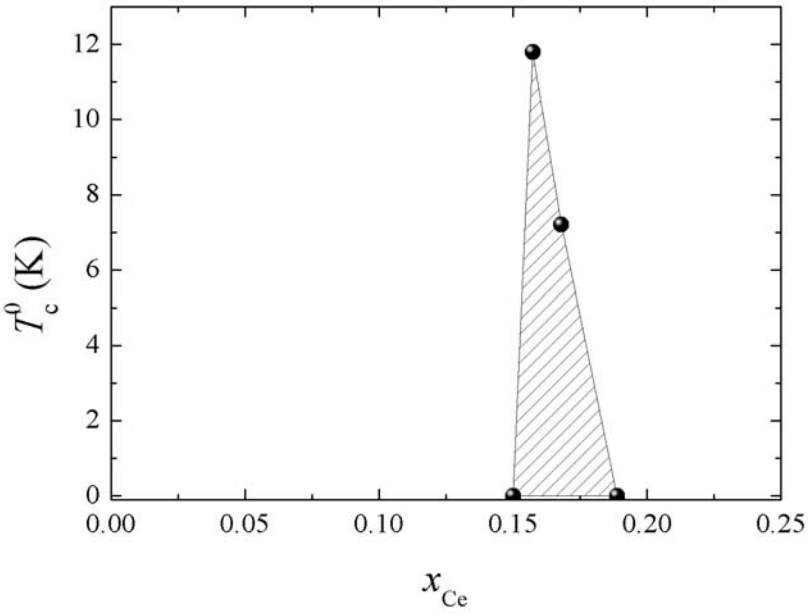

Fig. 5.16: Superconducting phase diagram obtained from $Eu_{2-x}Ce_xCuO_4$ thin films vs. cerium content. For $x \approx 0.15$ the highest superconducting transition temperature was found to be $T_c \approx 12.0\,K$.

$La_{1.94}Ce_{0.06}CuO_4$. Here, by reducing the growth temperature roughly 100 °C, the T′-phase could subsist down to $x = 0$. Reducing the growth temperature costs crystalline quality of the thin films as can be seen from (006)-peak intensities in Fig. 5.19. Since the growth temperature has to be lowered in order to preserve the T′-structure, the crystallinity deteriorates. Such behavior is quite opposite to that observed for $Pr_{2-x}Ce_xCuO_4$ or $Sm_{2-x}Ce_xCuO_4$. There, the crystallinity is highest for the undoped compound and deteriorates upon reaching the solubility limit of cerium. In Fig. 5.20 the resistivity behavior of undoped T′-structured thin film of La_2CuO_4 is plotted. The apparent insulating behavior in the end-member T′-compounds is not intrinsic but arises from the localization of carriers due to residual apical oxygen atoms. Therefore, the $\rho - T$ behavior depends strongly on the concentration of residual apical oxygen atoms. With the same compound, the $\rho - T$ becomes more metallic with more complete removal of apical oxygen. With the

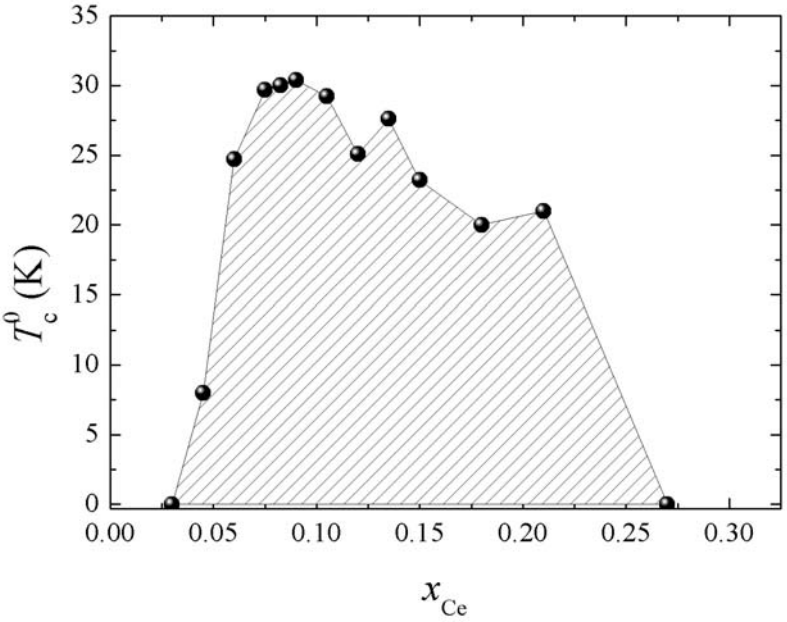

Fig. 5.17: Superconducting phase diagram of thin films of $La_{2-x}Ce_xCuO_4$ grown on (001)$SrTiO_3$, irrespective of growth- and annealing conditions. The maximum superconducting transition temperature is $T_c \approx 32\,K$ for $x \approx 0.9$.

same reduction recipe, the resistivity of T′-RE_2CuO_4 becomes more metallic with larger RE ions (see Fig. 5.27). In the case of RE = La, the room temperature resistivity is around 2 mΩcm.

Concerning the in-plane lattice length a substitution of large La^{3+}-ions by smaller Ce^{4+} should lead to a decreasing in-plane lattice parameter a_0, while electron doping results in an increase of a_0. The two effects appear to cancel each other out, since $a_0 = 4.01 \pm 0.006$ Å is independently on the cerium content x [296, 297]. It appears to indicate, that substrates with $a_{sub} \approx 4.0$ Å stabilize the T′-formation. But this turned out not to be true, since the use of $YAlO_3$ ($a_{sub} = 3.715$ Å) also supports the formation of the T′-phase.

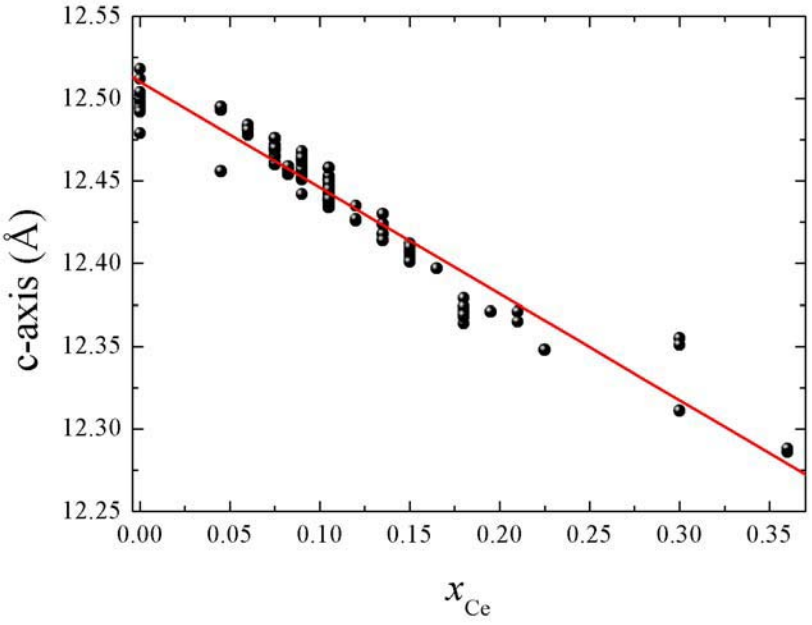

Fig. 5.18: *c*-axis dependency of thin films of $La_{2-x}Ce_xCuO_4$ grown on (001)$SrTiO_3$, irrespective of growth- and annealing conditions. The red line is a linear fit function $c(x) \approx 12.51024 - 0.64292 \cdot x_{Ce}$ (Å).

5.1.5 Thin films of $Gd_{2-x}Ce_xCuO_4$

Many attempts have been made so far to induce superconductivity in $Gd_{2-x}Ce_xCuO_4$. In all other cases when RE = La, Pr, Nd, Sm or Eu, as mentioned above, the in-plane antiferromagnetic ordering of copper breaks down before superconductivity appears. It has been found by Butera *et al.* [298] that magnetic ordering survives even up to the solubility limit of Ce or Th in $Gd_{2-x}Ce_xCuO_4$. $Gd_{2-x}Ce_xCuO_4$ has the smallest in-plane lattice constant a among the electron doped cuprates and hence the smallest c-axis length. Here, we report for the first time the growth of thin films of $Gd_{2-x}Ce_xCuO_4$ and transport properties thereof.
Since undoped $Gd_{2-x}Ce_xCuO_4$ resides at the border-line (tolerance factor is smallest, see. Fig. 3.18) it has the tendency to change crystal-symmetry from Nd_2CuO_4-structure to $\mathcal{O}'$-phase with reduced orthorhombic symmetry.

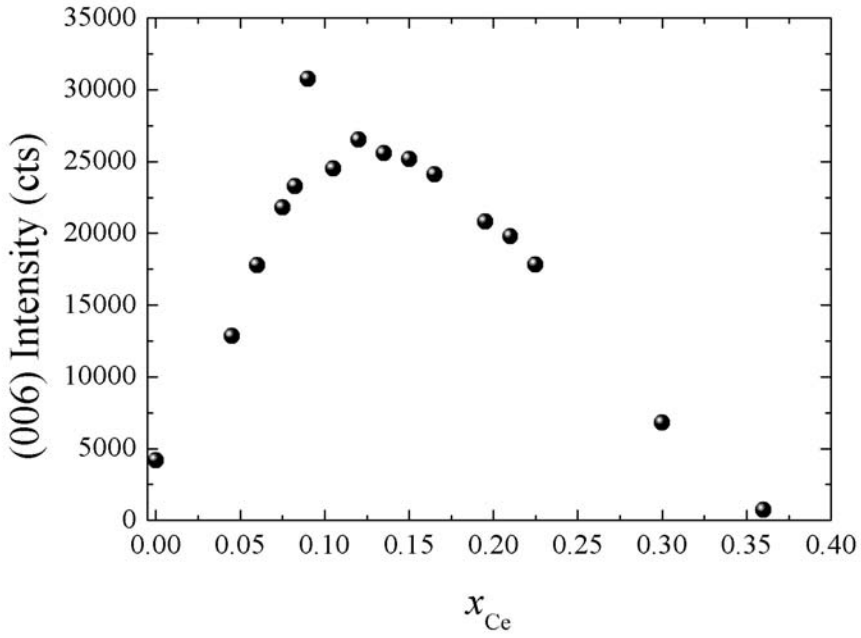

Fig. 5.19: Intensity of (006) peak of thin films of $La_{2-x}Ce_xCuO_4$ grown on (001)$SrTiO_3$, irrespective to growth- and annealing conditions. For low doping values the crystallinity drops down since the T-phase becomes more favorable towards zero doping.

There, the oxygens squares surrounding the copper ion are found to rotate along the *c*-axis ($\sim 5°$) [299]. This deviation leads to a pseudo-tetragonal in-plane lattice constant of $a = 5.5082\,\text{Å}$. In Fig. 5.21 the temperature dependency of resistivity is plotted for various cerium contents. If the cerium content increases the resistivity drops and the sample behaves more metallic. For $x \approx 0.165$ metallic behavior is found down to T$\approx 90\,$K. For lower doping levels insulating behavior ($\frac{d\rho}{dT} > 0$) is found even at room temperature. Although there is also a drastic change in the absolute value of resistivity upon oxygen reduction no superconductivity has been found.
Early attempts of doping Th^{4+} to Gd_2CuO_4 by Kenjo *et al.* [300, 301] have shown, that conductivity increases upon doping. Lowest resistivity behavior was obtained for $x_{Ce} = 0.157$ after the thin film has been reduced for 70 min at $\vartheta_{reduction} = 620\,°$C. This reduction temperature just lies 20 °C be-

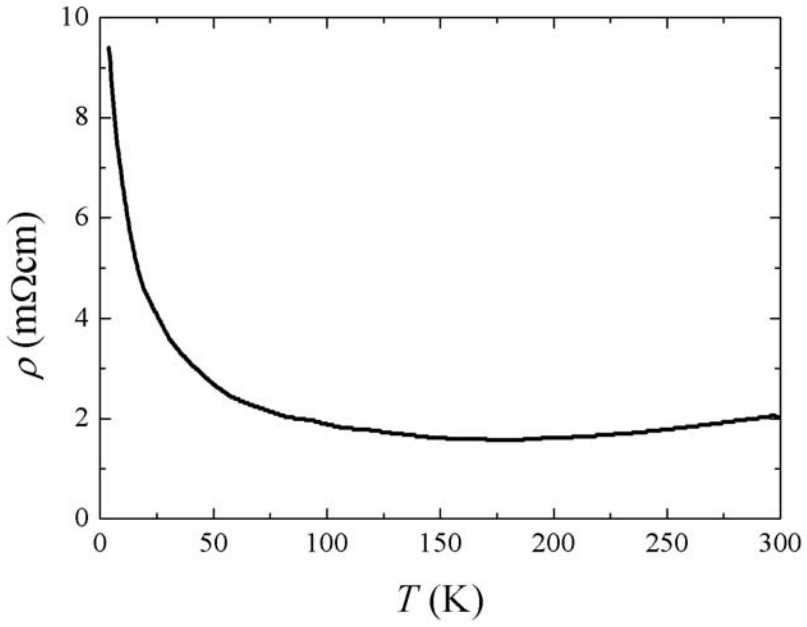

Fig. 5.20: Resistivity behavior of an undoped T′-structured sample of La_2CuO_4 grown on (001)$SrTiO_3$.

low the growth temperature. The ionic radius of eight-fold coordinated Gd^{3+} is 1.053 Å(Table 3.1). Upon doping the *c*-axis shrinks as

$$c(x) \approx 11.8714 - 0.2757 \cdot x_{\mathrm{Ce}}. \tag{5.4}$$

Now, the slope is -0.2757 and therefore again smaller compared to $Eu_{2-x}Ce_xCuO_4$. This finding is in close agreement to bulk samples prepared by Butera *et al.* [298] where $c(x) \approx 11.89575 - 0.33179 \cdot x_{Ce}$ has been reported. Since the authors do not mention, that their samples had been reduced, this somewhat larger *c*-axis indicates a higher occupation of the apical site with oxygen. Hence, this is also associated to the doping dependence of the in-plane lattice constant. While Butera *et al.* [298] report $a(x) \approx 3.89815 + 0.03855 \cdot x_{\mathrm{Ce}}$ the slope is equal to zero in the case of thin films used for this investigation. This means that even for the undoped sample the in-plane lattice constant is smaller compared to the substrate. Therefore, a tensile strain is not inconceivable. The absence of superconductivity in this

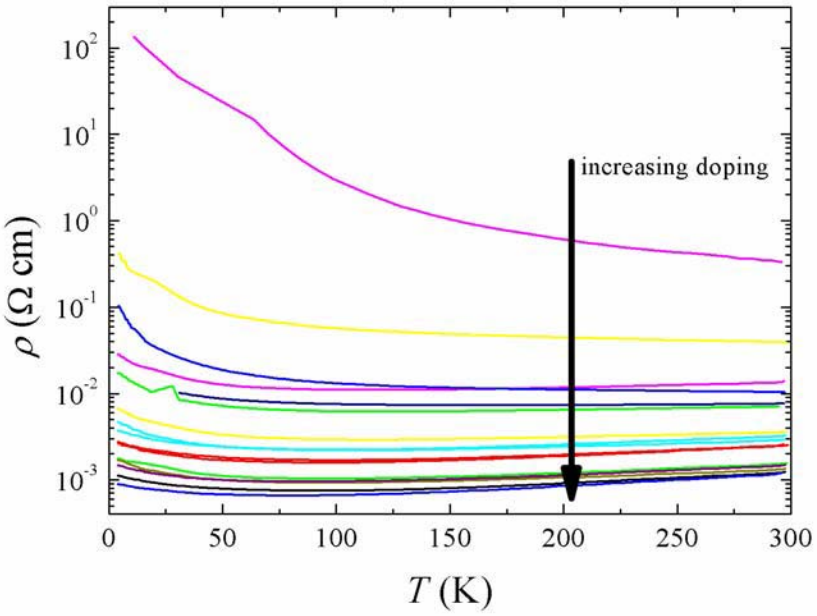

Fig. 5.21: Resistivity vs. temperature of $Gd_{2-x}Ce_xCuO_4$ thin films grown on (001)$SrTiO_3$.

compound forms a natural threshold in the series of T′-structured cuprates due to the lanthanide contraction [298, 303, 304, 305].

Optimally oxidized samples

For the samples used above, the reduction treatment has been optimized according to thermodynamic conditions. It was possible to anneal thin films in a way that no decomposition products are formed. Here, we now walk the opposite way and try to feed as much oxygen as possible to the cuprate. We speculate, that an enhanced occupation of apical sites of copper induces insulating behavior. More copper will become six-fold coordinated and therefore the ionic radius of copper grows.

At first we focus on samples were no tolerance-factor driven phase-change occurs, e.g., RE_2CuO_4 with RE = Pr, Sm, Eu and Gd. For this experiment, a custom designed quartz reactor (see Picture 8.10) was used. Ozone was

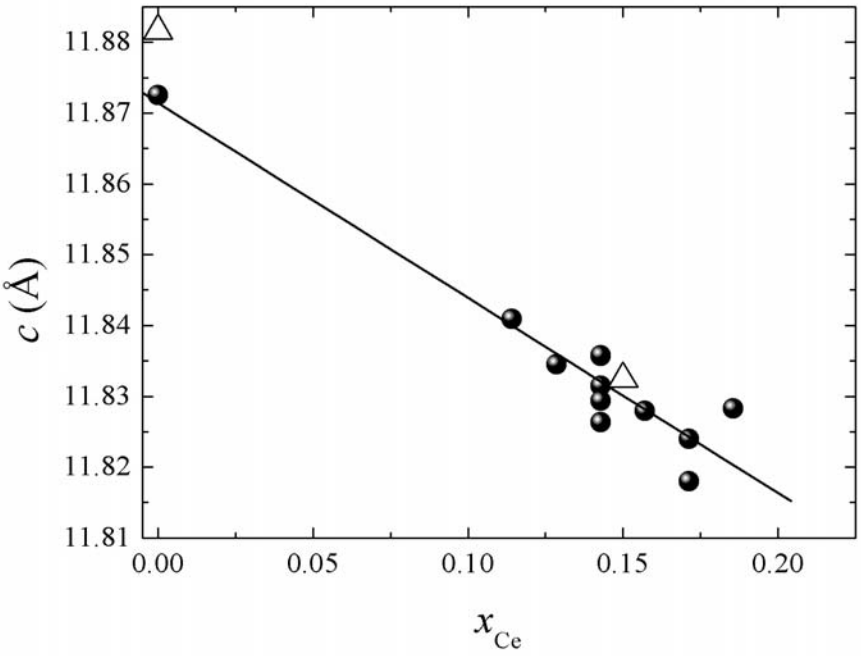

Fig. 5.22: *c*-axis dependency of thin films of Gd_2CuO_4 for different cerium concentration. The straight line is a least square fit to the data points (sphere). For comparison, data points obtained by Uzumaki *et al.* [253] and Ganguly *et al.* [302] are also included (triangles).

produced by a silent discharge generator with typical ozone concentration of approx. 28 %. Samples were mounted on a sapphire plate heated by a custom designed Pt-Rh heater. After 24 h at 400 °C samples were cooled to room-temperature at 2 K/min. The temperature dependent resistivity behaviors of Pr_2CuO_4, Sm_2CuO_4, Eu_2CuO_4 and Gd_2CuO_4 are shown in Fig. 5.23. First, all samples show insulating behavior. It is interesting to note, that the $\rho(T)$ curves in Fig. 5.23 show identical trend and to a much higher extend, the absolute resistivity values became indistinguishable.
Compared to Fig. 5.27, the absolute resistivity value drastically increased. Even for the RE = Gd case, the absolute resistivity value increased by a factor of ten. Moreover, the growth of *c*-axis length after the oxidizing treatment is significant (Fig. 5.26). On the other hand, within the resolution limits, no change of the in-plane lattice length was found after the oxidizing

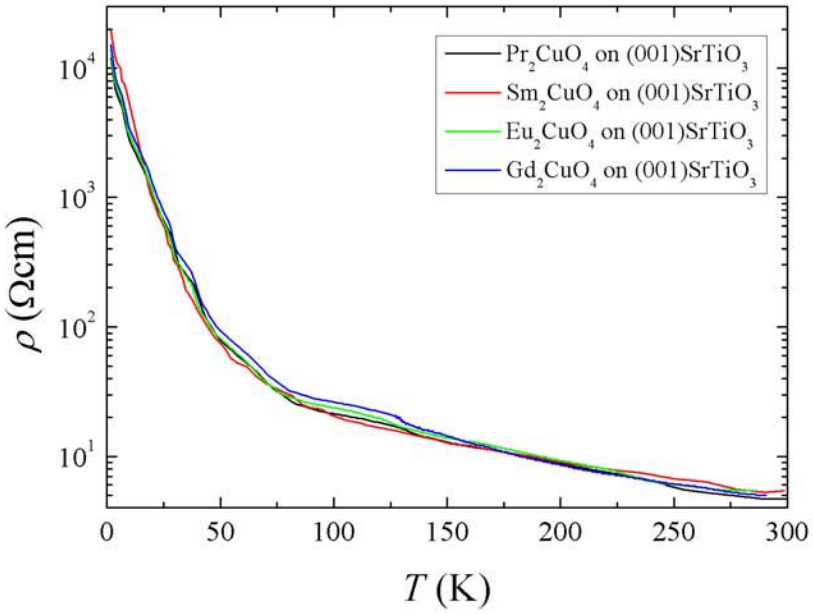

Fig. 5.23: Resistivity vs. temperature of thin films of RE_2CuO_4, with RE = Pr, Sm, Eu and Gd after an extensive oxidizing treatment.

treatment. This is racily indicating, that the apical oxygen does not act as a dopant. Such behavior is in strong contrast to the hole doped analogues and T-structured $La_{2-x}Sr_xCuO_{4+\delta}$, where oxygen also acts as a dopant [306].

5.1.6 Discussion

As it is shown in Fig. 5.24 the phase diagram of the electron doped cuprates strongly depends on the rare earth element which is used. In the case of Eu the superconducting region covers a small part of electron doping. If the rare earth ionic radii increases, the superconducting region becomes broader and the maximum superconducting transition temperature increases. Such behavior is quite different from the 123 phase, where irrespective of the rare earth element the maximum transition temperature is more or less around 90 K (except Pr and Tb)[307]. In Fig. 5.25 the *c*-axis length for all $RE_{2-x}Ce_xCuO_4$ thin films is plotted as a function of Ce concentration. Since

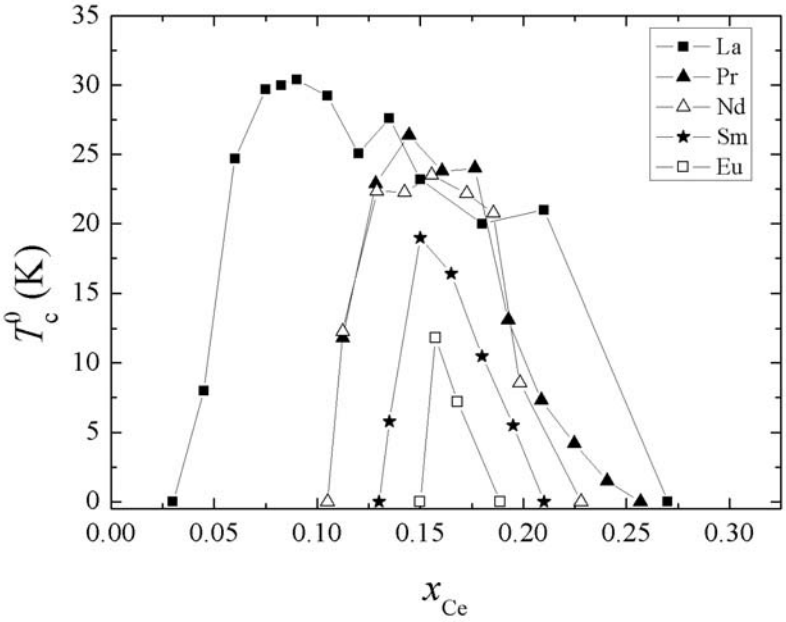

Fig. 5.24: Superconducting phase diagram of all thin films of RE_2CuO_4 vs. doping.

Ce^{4+} is smaller than any RE^{3+} the c-axis length shrinks monotonically upon doping and hence due to the reduced repulsion of the CuO_2-planes. Since La^{3+} is the largest cation, also the c-axis length is the largest. From Fig. 5.25 one might expect that all lines match in one point for $x = 2$ where the hypothetical $Ce_2^{4+}CuO_4$ compound is placed. Of course, such compound can not exist since the formal valency of copper becomes equal to zero. A comparison for undoped Nd_2CuO_4-structured thin films is given in Fig. 5.27 by resistivity data. Data have been taken from samples grown on (001)$SrTiO_3$. In case of La, Pr and Nd, metallic behavior is found down to 170 K, 130 K and 190 K, respectively. In the case of Sm, Eu, Gd and Tb, the resistivity value increases and the temperature dependent behavior becomes more and more insulating. From Fig. 5.27 we conclude that the c-axis and a-axis lengths play a crucial role on superconductivity in the case of T′-structured compounds although none of these compounds contain cerium. Let us now have a look to Fig. 5.26 and keep in mind, that the samples used in Fig. 5.27 have been

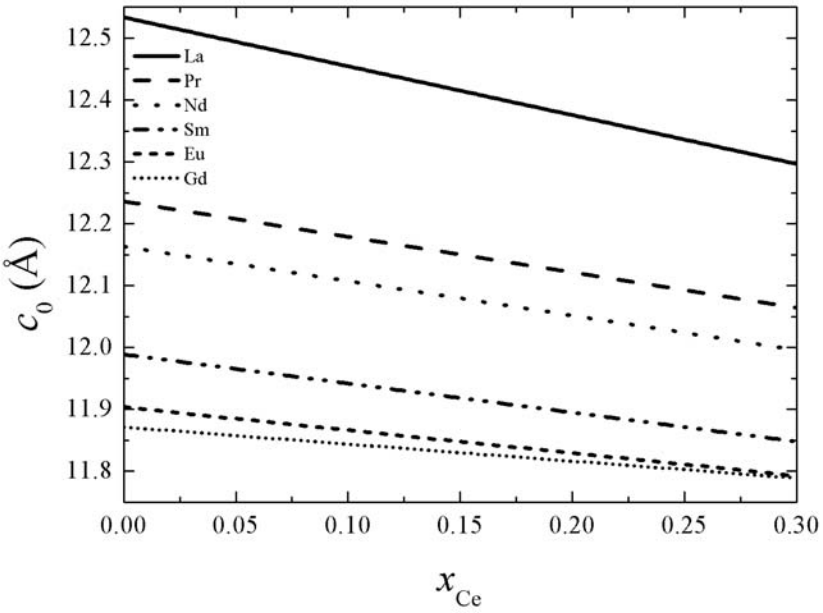

Fig. 5.25: c-axis parameter of all thin films of $RE_{2-x}Ce_xCuO_4$ vs. doping.

treated by an optimized reduction treatment. The c-axis lengths are plotted for optimally reduced samples as well as optimally oxidized samples. From the x-ray diffraction pattern no phase change or other products could be determined; but the c-axis increased significantly after the oxidizing treatment in ozone. In the case of La, the increase of the c-axis is smallest ($\approx 0.05\,\text{Å}$), but for RE = Pr-Gd it remains almost constant ($\approx 0.12\,\text{Å}$). In Fig. 5.23, resistivity data vs. temperature are plotted for the same samples - but now annealed at $400\,°C$ and 1 atm ozone. At first, one can easily recognize that the room-temperature resistivity does almost not vary compared to Fig. 5.27 where more than six orders of magnitude of resistivity are shown. It has been empirically known that the hole-type carriers cannot be introduced to the squaric sheets and the electron-type carriers neither to octahedral nor pyramidal sheets mostly due to the crystallographical instability or carrier-compensating oxygen non-stoichiometry.

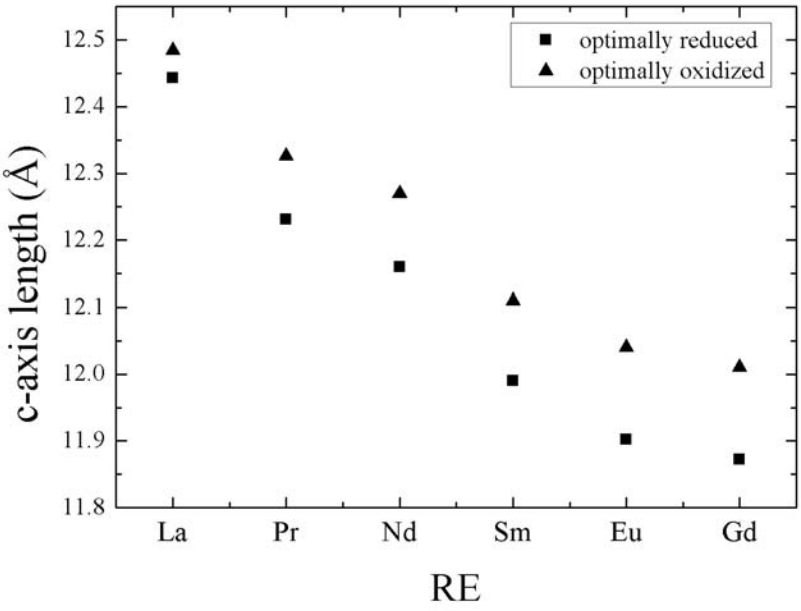

Fig. 5.26: *c*-axis lengths of RE_2CuO_4. Square points are obtained from samples treated by optimized reduction conditions. Triangular points are obtained after the sample was optimally oxidized.

5.2 Low energy muon spectroscopy

5.2.1 Introduction

Highly polarized positive muons (μ^+), implanted with about 4 MeV kinetic energy in matter (so-called surface muons) are widely used as microscopic magnetic probes or spin labels (Muon Spin Rotation or Relaxation (μSR)). However, because of the high energy, mean and variance of the implantation depth are of the order of fraction of mm, thus limiting the application of the μSR technique to the study of bulk matter properties without any depth resolution. On the other hand, thin films, multilayers and near surface regions are of increasing importance in contemporary condensed matter science, with the reduced dimensionality providing a new approach into fundamental and emergent physical behavior and novel technological applications. The muon, as a local sensitive probe with complementary observational time window to

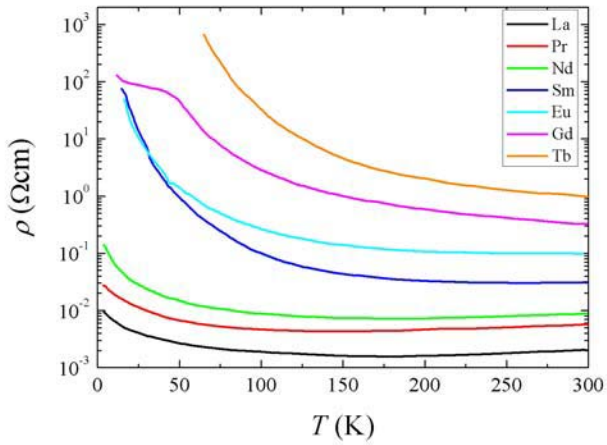

Fig. 5.27: Resistivity vs. temperature of optimally reduced T′-RE_2CuO_4.

other probes or techniques, offers new insights into these objects of investigation. To be used for thin film studies and to be able to perform depth dependent scanning of a probe, the energy of the particle must be tunable in the interval between a few tens of keV down to a few eV for surface investigations. At these energies, implantation depths in matter typically extend from 200 to 300 nm down to the subnanometer region. Such a low energy (LE) beam with μSR spectrometer has been developed over recent years at the Paul Scherrer Institute thus setting the basis of the LE-μSR method and opening new fields of μSR investigations [310]. Basically, LE-μSR allows depth dependent scanning of samples and the study of samples, which are too thin to be investigated with standard μSR techniques.

5.2.2 Generation of epithermal muons

At present, in analogy with the similar case in positron physics, the moderation technique is the most simple and efficient method [311, 312] to create a sufficient amount of very slow particles starting from particles that are intrinsically of energetic nature (the muon energy from the pion decay is about 4 MeV). Briefly, an intense beam of readily available surface μ^+ is slowed down to epithermal energies ($\sim$ 15 eV) in an appropriate moderator consisting in a thin film (few hundreds nm) of a van der Waals bound solid deposited

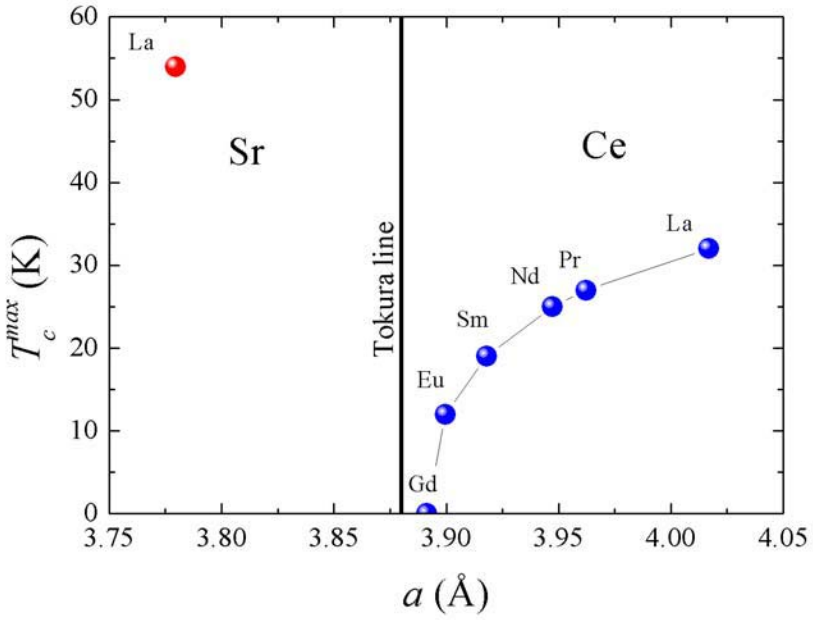

Fig. 5.28: Maximum transition temperature obtained for T′-$RE_2Ce_xCuO_4$ vs. in-plane lattice constant. The point for $La_{2-x}Sr_xCuO_4$ was taken from [308]. After Tokura [309].

on a metal substrate. The generation of epithermal muons relies on the specific behavior of charged particle in wide band gap cryosolids, particularly in the regime preceding thermalization. The general picture that emerges from various investigations is as follows. In these weakly bound solids, in the final stage before thermalization, slowing down and scattering are dominated by soft μ^+-atom elastic collisions. In this energy regime, electronic slowing down processes such as ionization, excitation or electron capture are strongly suppressed or even energetically not allowed because of positive threshold energies. Therefore, muons, which by the statistical nature of the energy loss process in matter fall within the appropriate energy range in the condensed layer are likely to avoid neutralization (muonium formation) and thermalization and escape from the frozen gas at epithermal energies. The reduced energy-loss rate in these perfect insulators leads to a large escape depth of the order of 50 nm and to efficiencies of the order of 10^{-5} - 10^{-4} to convert an energetic fast muon into a very slow one [313]. The moderation mechanism

is also reflected by the correlation between efficiency and band-gap energy and by the energy distribution of the emitted epithermal muons peaking at $\sim 15\,\mathrm{eV}$. The initial longitudinal polarization (almost 100%) of the incoming surface muons is conserved, because of the fastness of the moderation process ($\sim 10\,\mathrm{ps}$)[312]. The moderation efficiency can be optimized by choosing appropriate growth conditions of the solid gas layer. The long-term stability of the moderator is ensured by ultrahigh vacuum (UHV) conditions.

5.2.3 Experimental setup

Experiments are performed with the apparatus schematically shown in Fig. 5.29. The UHV apparatus consists of the source of epithermal muons, the low energy beam and the μSR spectrometer. Surface muons of energy $\sim$4 MeV are incident at a rate of $\sim 2 \cdot 10^7$/s onto a cryogenic moderator consisting of $\sim 300\,\mathrm{nm}$ of solid argon condensed onto a microstructured silver substrate held at $< 10\,\mathrm{K}$ and at a positive potential of 15 or 20 kV [314]. Epithermal muons emerging from the moderator are accelerated in its potential and transported by electrostatic "einzel" lenses[4] and a mirror to the sample, where they are focused to a beam spot with typical diameter 10-15 mm (FWHM) and arrive at a rate of about 300/s. The electrostatic mirror separates low energy muons from any other particles such as beam positrons or fast muons exiting the moderator. The low energy muons are detected where they pass through a 10 nm thin carbon foil placed at an intermediate focus of the beam transport system ("trigger detector" in Fig. 5.29). At the foil, the muons release a few electrons, which give the required muon implantation signal for time differential μSR experiments in a microchannel plate. On passing through the foil, the muons lose 1.6 keV and acquire an rms energy spread of 0.5 keV. The trigger signal is also used to measure the time-of-flight (TOF) of each low energy muon after it was detected at

[4] The name Einzel (equipotential) lens means that the electrodes 1 and 3 are grounded while the central electrode-2, which is equidistant from 1 and 3, is held at a voltage V_2. Thus the incident muon beam is focused by this lens system without imparting any net acceleration to it. If $V_2 > 0$, the muon is first accelerated and then decelerated. This lens lets all muons through. If $V_2 < 0$, it first decelerates the muon and then accelerates it; thus acting as a high-pass muon energy filter by reflecting the low energy muons and letting only the high energy muons pass through. However, it should be ensured that $V_2 > V_{cathode}$ to ensure all muons are not mirrored.

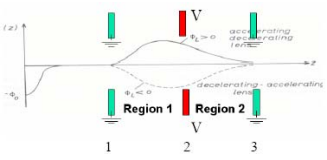

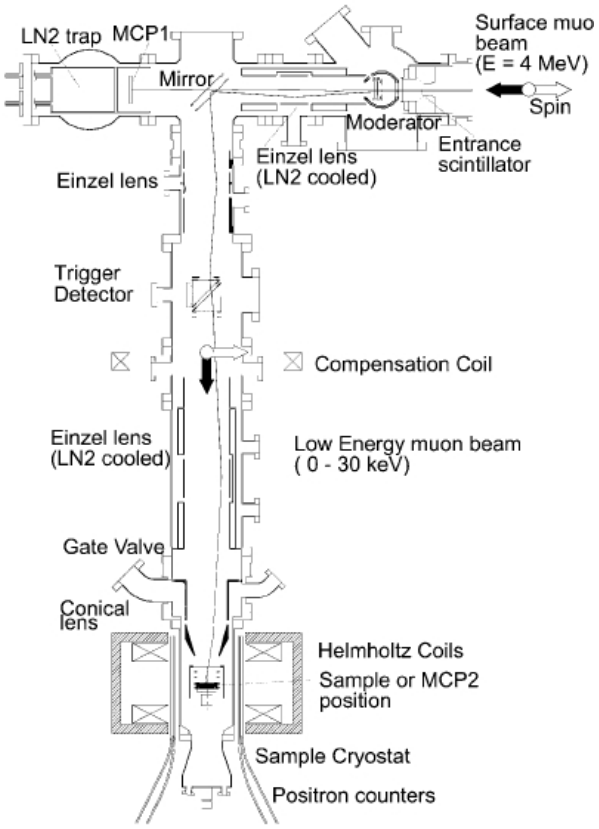

Fig. 5.29: Layout of the apparatus used to generate the polarized low energy muon beam and to perform muon spin rotation and relaxation experiments. From [315].

a scintillator on entering the apparatus. By selecting on the TOF, muons with energies outside the epithermal region coming from the moderator are discarded, while allowing only muons with low enough energy to be reflected by the mirror. The final kinetic energy of the muons arriving at the sample may be varied over the range of $\sim 0.30\,\mathrm{keV}$ by applying an accelerating or decelerating potential of up to $12.5\,\mathrm{kV}$ to the sample, which is mounted via a sapphire plate on a continuous-flow helium cryostat or another sample holder. Due to the 90° deflection at the electrostatic mirror, the muons are horizontally polarized, transverse to their direction of motion, when they arrive at the sample. Hence, the muon spins will precess in the horizontal plane if a vertical magnetic field is applied, or alternatively in a vertical plane about a horizontal field parallel to their direction of motion. Both geometries have been used in experiments on this apparatus. The decay positrons from

the muons implanted in the sample are normally detected by a set of four scintillator "telescopes" placed left, right, above and below the beam axis.

5.2.4 Microscopic magnetic field distributions near the surface of $La_{2-x}Ce_xCuO_4$ thin films

Over the past 20 years, the μSR technique has been applied to measure various aspects of the magnetic behavior of high-temperature superconductors whose superconducting properties are intimately related to their magnetic properties. Already the first phase diagram of electron and hole doped cuprates was obtained by μSR technique. On the electron doped side, additional coupling of the rare earth elemental moment to the copper moment has been reported from muon spectroscopy. Since the magnetic moment of La^{3+}

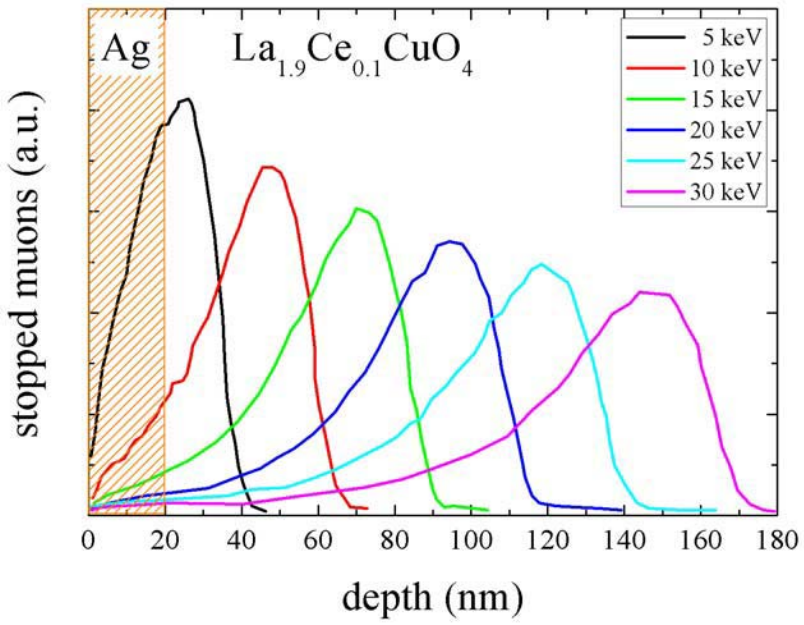

Fig. 5.30: Depth distributions of implanted muons for various energies, calculated using the Monte Carlo code TRIM.SP. These distributions have been convoluted with a Gaussian of width 5 nm to represent the depth straggling due to surface roughness of the film.

is zero, no admixture of La-Cu coupling effects take place at low tempera-

ture[5]. Therefore, $La_{2-x}Ce_xCuO_4$ is of high interest since one only observes the copper-copper relations. The μ^+ can measure the microscopic field distribution in the vortex state of a type II superconductor, which is characterized by a large internal spatial inhomogeneity due to the penetration (for $B_{c_1} < B_{ext} < B_{c_2}$) of quantized flux lines and the formation of a flux line lattice (FLL). Since the muons are randomly distributed over the flux line lattice,

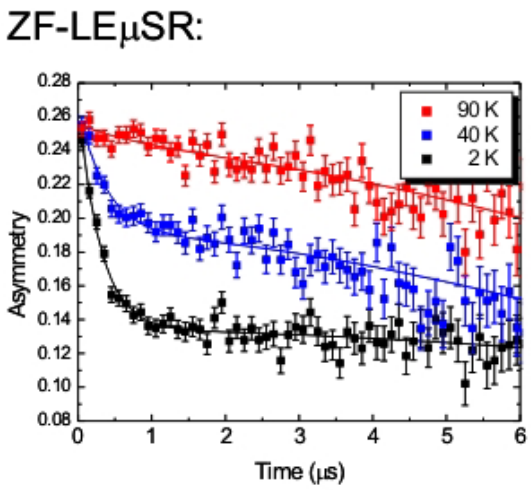

Fig. 5.31: Asymmetry plot for temperatures 90 K, 40 K and 2 K. An increase of damping rate at lower temperatures indicates an enhancement of static magnetic order.

the internal field has a simple relationship with $P(t)$, the time evolution of the muon spin polarization. The microscopic field distribution is obtained by Fourier transforming $P(t)$. Muon spin relaxation is one of the most comprehensive bulk methods available for the absolute determination of λ, the London magnetic penetration depth, a fundamental property of the superconductor, since its value reflects the number density n_s and effective mass $m_s^\star$ of the superconducting carriers: $\mu_0\lambda^2 = m_s^\star/4e^2n_s$. The determination of λ from the moments of the magnetic field distribution in the vortex state by muon relaxation gave the first broadly accepted value for this fundamental quantity. However, this method is not free from limitations. The second and (higher) moments of the magnetic field distribution depend on all sources of magnetic field inhomogeneities. Furthermore, one has to rely on the use of

[5] In the case of Pr, Nd, Sm, Eu and Gd, the magnetic moment is not zero and therefore coupling to the copper spins takes place.

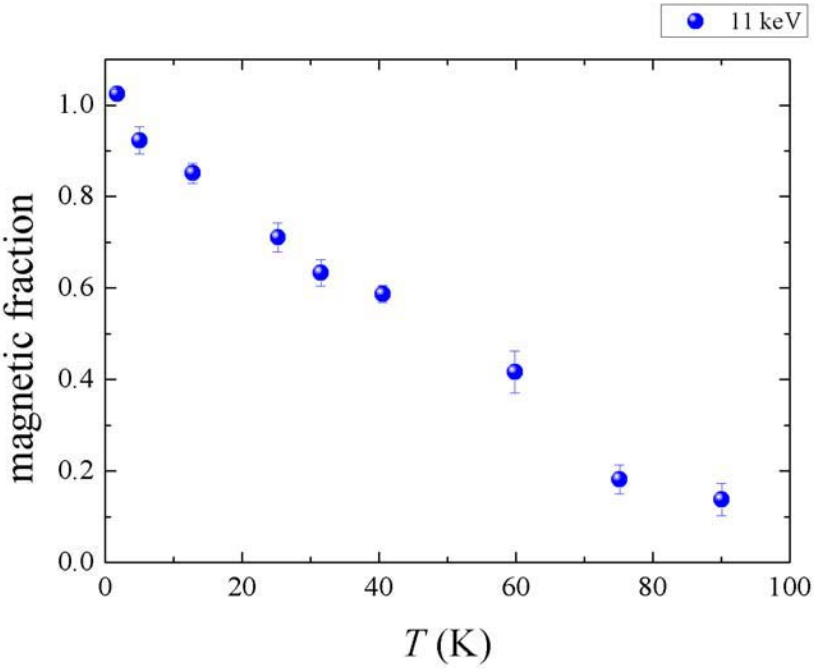

Fig. 5.32: Magnetic volume fraction of the $La_{1.9}Ce_{0.1}CuO_4$ thin film vs. temperature.

the modified London model, where λ describes how the magnetic field decays away from the vortex core, and know the vortex lattice symmetry and structure. Flux line core effects, deviations of the flux line lattice from its ideal configuration, and other effects such as finite time range and ringing suppression have to be included in the data analysis. The depth sensitivity in the nm range of LE μ^+ penetrating into the surface region allows to directly measure values of magnetic fields as a function of depth, thus avoiding the difficulties mentioned in [316]. For this experiment a magnetic field of 8.5 mT was applied parallel to the surface of the $La_{1.91}Ce_{0.09}CuO_4$ film (i.e., perpendicular to the c-axis) after zero field cooling to 4 K. The value of B_{c_1} at low T has been estimated from magnetization and gives approx. 200 Oe. Additionally, surface barriers and flux pinning prevent flux line entry, so in these measurements we are measuring Meissner screening. It is well known that superconductors in the Meissner state do not completely exclude a magnetic field applied parallel to the surface, but that the field penetrates a short

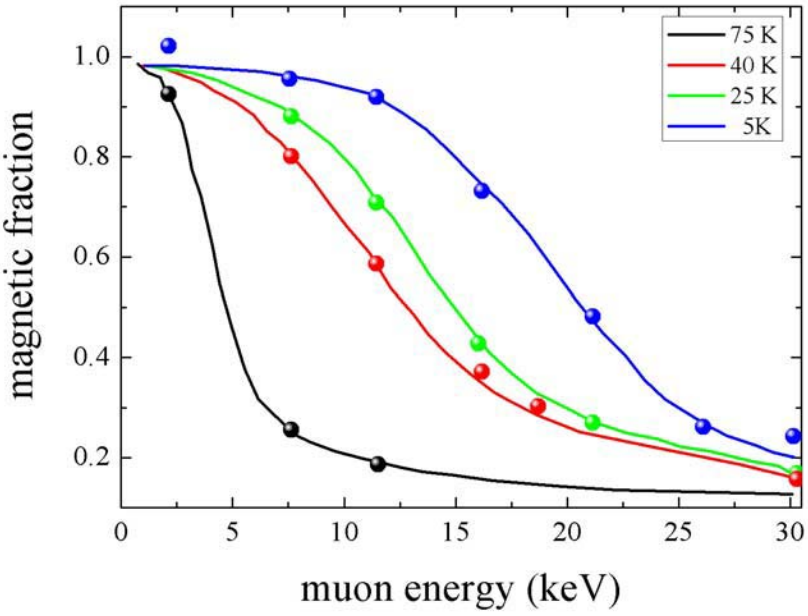

Fig. 5.33: Magnetic volume fraction vs. muon energy (penetration depth (see Fig. 5.30)) for different temperatures. The magnetism is concentrated at the $Ag/La_{1.9}Ce_{0.1}CuO_4$ interface. The thickness of the magnetic layer decreases with increasing temperature.

distance into the superconductor. In the simplest case, it is expected that an external field B_{ext}, applied parallel to the surface, penetrates according the equation

$$B = B_{\text{ext}} \cdot e^{-\frac{z}{\lambda}} \tag{5.5}$$

where z is the depth perpendicular to the surface, and λ is the London magnetic penetration depth, describing here the magnetic field decay from the superconductor surface. LE-μ^+ can provide an experimental proof of Equation (5.5), which is expected to apply in those superconductors (such as high-T_c materials including LCCO) which have a large value of the ratio $\kappa = \lambda/\xi$, where ξ is the coherence length. Equation (5.5) was first predicted in 1935, but never experimentally tested at microscopic level. This is of relevance, if we consider that microwave techniques used to measure with high precision the temperature dependence of the change in the London penetration depth, $\Delta\lambda(T)$, implicitly assume Equation (5.5). It should be stressed

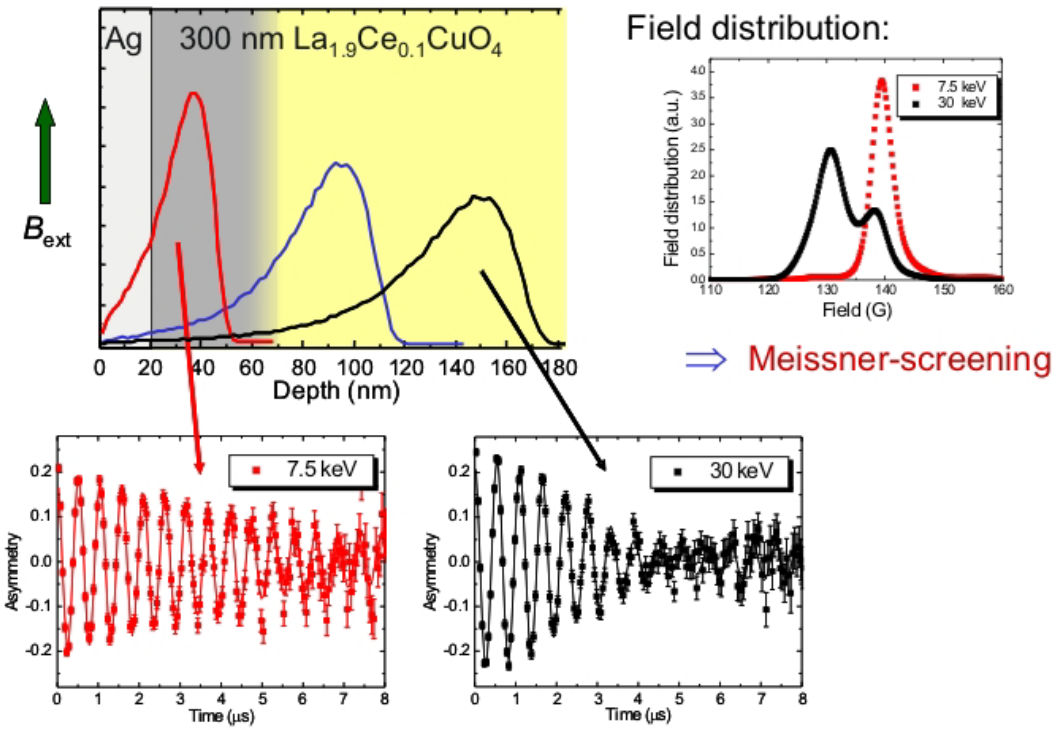

Fig. 5.34: Transverse field measurements. The major result is the right-up figure, where the field distribution is plotted as a function of the applied external magnetic field. The red curve represents muon with implantation energy of 7.5 keV while the black one represents the 30 keV case. In the latter one, where the muons penetrate almost half of the thin film, a clear splitting is observed since the observed signal is a superposition of the internal and external field. This effect can be also seen in the two asymmetry plots, where for the 30 keV case clearly a superposition of two frequencies is observed.

that low energy muons provide a direct measure of the spatial variation of the magnetic field beneath the surface. This technique differ in principle and not just in methodology from the various methods used to deduce the London penetration length in that no assumptions have to be made about the functional form of the field penetration law. By tuning the energy from 3 to 30 keV, the depth of implantation was varied between $\sim$ 20 and $\sim$ 150 nm. The muon implantation depth distribution $p(z)$ corresponding to each of the implantation energies was calculated using the Monte-Carlo code TRIM.SP (Fig. 5.30) [317]. Figure 5.35 shows the corresponding magnetic field distributions obtained at 5 K from various implantation energies. The higher the

incident muon energy, the lower the average field they experience. It can also be seen that muons of a given energy stop over a certain range of depths, giving a small range of fields in $P(B)$. To an excellent first approximation, to plot the field B as a function of depth z, we simply read off the peak values in Fig. 5.35 and plot them versus the peak values in Fig. 5.34. This plot allows one to iterate rapidly to the correct relationship between $P(B)$ and $p(z)$:

$$P(B) = \frac{p(z(B))}{|dB/dz|}. \tag{5.6}$$

The values of B_{peak} versus z_{peak} obtained from the iteration are plotted in Fig. 5.31 for several sample temperatures. The theoretical lines are plots of the function:

$$B(z) = B_{ext}\frac{\cosh((t-z)/\lambda)}{\cosh(t/\lambda)} \tag{5.7}$$

which is the form taken by Equation (5.5) for a thin film of thickness $2t$, with the flux penetrating from both surfaces. The data clearly shows, that there

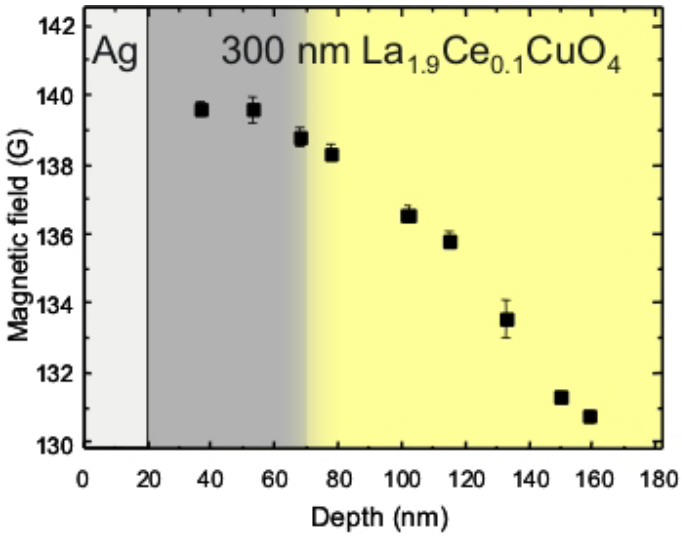

Fig. 5.35: Internal magnetic field strength vs. muon implantation depth at 5 K.

is coexistence or competition between magnetic order and superconductivity in the same sample. The magnetic interaction persists up to 90 K and is mainly concentrated at the surface of the sample. Moreover, the magnetic layer thickness decreases with temperature. The relatively weak magnetic

relaxation rate of the zero-field (ZF)-μSR signal therefore may indicate the presence of a diluted spin system on a nm-scale. Hence, the magnetic moment of copper was found to be approx. $0.1\,\mu_B$, whereas usually $\approx 0.45\,\mu_B$ is reported (see Fig. 2.16).
There remain some open questions which are currently under investigation. The parameter, stabilizing the magnetic phase, has not yet unambiguously been elucidated. One may think in a way that towards the surface, higher oxygen concentration is located. Ideas like strain relaxation can be ruled out since the rocking curve FWHM does not change by varying the thickness of the deposited thin films. Moreover, it can not be ruled out that the magnetic layer is also superconducting since the magnetic and superconducting lengths scales are at least of the same order.

5.2.5 Determination of the penetration depth λ

It was mentioned already above, that the LE-μSR provides a direct measurement tool for the penetration depth λ. However, since this measurement method provides resolution as high as 10 Å, the absolute value of the thin film thickness has to be determined with at least similar resolution. Neutron-reflectometry is the method of choice which provides the desired resolution [318]. Neutron reflectivity measurements on $La_{1.9}Ce_{0.1}CuO_4$ thin films on (001)$SrTiO_3$ substrates have been done at the `AMOR`-spectrometer at the Paul Scherrer Institute (Swiss). For unpolarized neutrons the refractive index is defined in an analogous fashion as for x-rays:

$$n = 1 - \frac{2\pi}{k_0^2} N b_{coth} = 1 - \frac{2\pi}{\hbar} V_n \tag{5.8}$$

where b_{coth} is the coherent scattering length and V_n is the neutron-nucleus pseudo potential. Usually for neutron scattering the dispersion correction can be neglected since for most nuclei and neutron wave lengths used there is no resonance absorption close by. Furthermore, the penetration depth is much bigger for neutrons than for X-rays. The true advantage of neutrons lies in the fact that neutrons carry a magnetic moment which may interact with the magnetic moments in the sample. The obtained reflection function at room temperature of the $La_{1.9}Ce_{0.1}CuO_4$ thin film is plotted in Fig. 5.36. For the fitting process, the software `Parratt 32` is used for the determination of the sample thickness ($d = 247$ nm). However, data taken at 10 K do not show any Laue-fringes. This is probably related to the occurrence of a

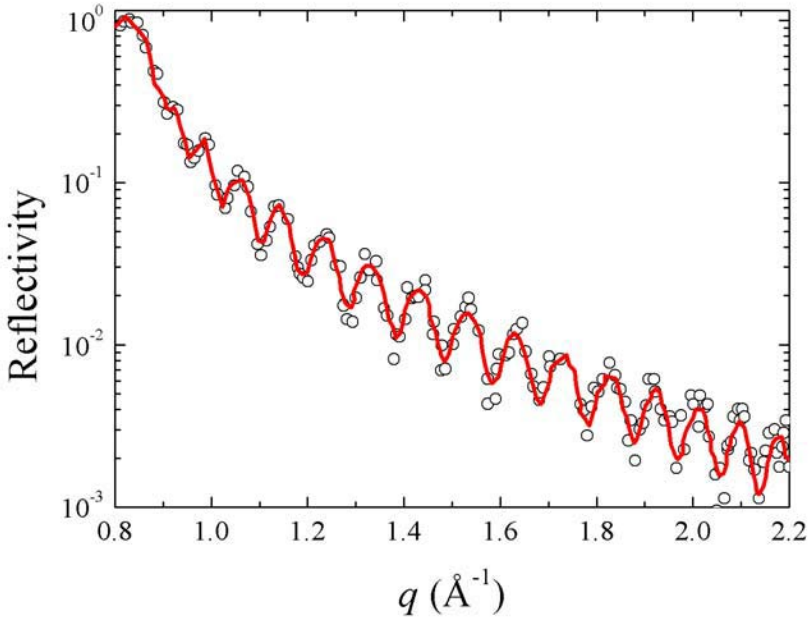

Fig. 5.36: Reflectivity vs. reciprocal spacing q. Due to the homogeneity of the $La_{1.9}Ce_{0.1}CuO_4$ thin film on (001)$SrTiO_3$, Laue-fringes are visible. The data have been fitted using the reflectivity tool PARRATT32. The calculated thickness is $d = 2470$ Å, and the surface-roughness is about 10 Å. Data points were taken at room temperature.

magnetic phase, as discussed in Section 5.2.4.
Since we have now precisely determined the sample thickness, penetration-depth measurements using LE-μSR can be continued. In Fig. 5.37, the principle of the penetration depth measurement is illustrated. Magnetic field penetrates into a superconductor following a `cosh`-function. With increasing temperature, the strength of the Meissner-screening weakens and therefore the modulation of the `cosh`-function is reduced. Exactly such behavior is observed in the present experiment. The external magnetic field is kept constant while the temperature is increased. At each temperature, muons are implanted with an energy of approx. 20 keV. According to Fig. 5.30, muons with an energy of 20 keV correspond to an implantation depth of 122 nm, which is the center of the $La_{1.9}Ce_{0.1}CuO_4$ thin film. From the asymmetry plot at each temperature, a Fourier-analysis provides the strength of the in-

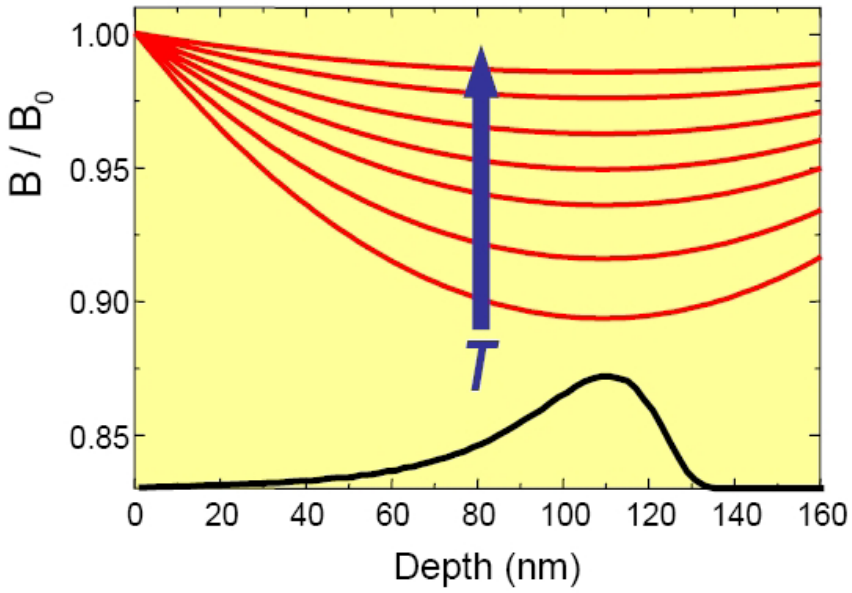

Fig. 5.37: Principle for the determination of the penetration depth λ using LE-muons. The penetrated field follows a `cosh`-function. With increasing temperature (marked by the arrow), the shielding potential of the superconductor weakens.

ternal and external magnetic field simultaneously. Therefore, the penetration depth λ can be calculated by

$$\lambda = \frac{1}{2} \frac{d}{arccosh\left(\frac{B_{ext}}{B_{int}}\right)} \tag{5.9}$$

$\lambda^{-2}(T)$ at low temperatures in hole-doped cuprates is consistently linear [264] or quadratic in temperature. Theory has not found a scenario in which behavior flatter than T^2 is predicted for $d_{x^2-y^2}$ superconductors. On the other hand, $\lambda^{-2}(T)$ in gapped e.g., s-wave superconductors is exponentially flat at low temperatures. As it is shown in Fig. 5.38, the lowest possible temperature in our setup is 5 K. However, this is not low enough in order to provide a conclusive fitting to the obtained data. At least, the obtained value of the penetration depth is comparable to other electron-doped superconductors [264], where s-wave behavior has been concluded from conventional low frequency two-coil mutual inductance technique. On the other hand, the data obtained here clearly demonstrate, that there is not only superconductivity but also a hereto unknown magnetic order or disorder. It was shown,

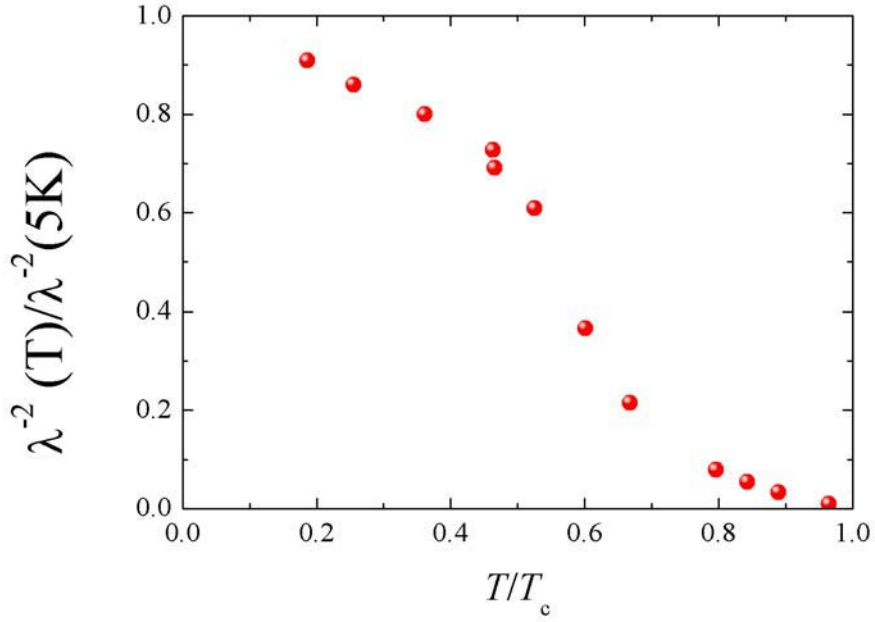

Fig. 5.38: The reduced penetration depth $\frac{\lambda^{-2}}{\lambda_{5K}^{-2}}$ is plotted as a function of the reduced temperature $\frac{T}{T_c}$.

that this magnetic layer is not homogeneous in depth although chemical inhomogeneities can be ruled out in agreement to Rutherford-backscattering measurements performed at ETH-Zurich (Swiss); in other words, the magnetic strength decreases with increasing depth. Moreover, there is a clear temperature dependency found (Fig. 5.32), where the magnetic volume fraction at a given depth increases with decreasing temperature. Up to now, no clear picture can be concluded from the above described measurements concerning the occurrence of such an unexpected magnetic phase. Certainly, possible oxygen inhomogeneities, as there are apical oxygens diffusing into the thin film by time, are of primary interest. In this context, preliminary LE-μSR data of an oxygenated $La_{1.9}Ce_{0.1}CuO_4$ thin film in ozone, clearly support the idea, that the apical oxygen induces antiferromagnetic order (the oxygenated sample did not show a superconducting transition). Coex-

istence of superconductivity and antiferromagnetism in the electron doped $Nd_{2-x}Ce_xCuO_4$ system has been suggested by Uefuji *et al.* [319].

6

New superconducting cuprates

The general accepted phase diagram of cuprate superconductors uses $Nd_{2-x}Ce_xCuO_4$ as representative for electron doped cuprates (Fig. 2.12). According to the investigations carried out in this thesis, the superconducting region seriously depends on the choice of the rare earth element used in $RE_{2-x}Ce_xCuO_4$ (Fig. 5.24). It was found that the superconducting region is largest in the case of RE = La and moreover, the highest superconducting transition temperature is also found in this case. As the ionic radii of the rare earth element decreases, also the maximum achieved superconducting transition as well as the superconducting region decreases. The threshold for superconductivity is located between Eu and Gd. So far, there has been no reports of superconductivity in $Gd_{2-x}Ce_xCuO_4$ in the literature.
In the case of $La_{2-x}Ce_xCuO_4$ thin films, it was found that one has to have always an eye to the temperature dependency of the tolerance factor in order to avoid the formation of the T-structured phase. As it is known from bulk samples, the 214 phase of La crystallizes in the T-structured phase. Although it was possible stabilizing La_2CuO_4 in the T′ structure utilizing the low growth temperatures in reactive MBE growth, the crystallinity is worse compared to cases were RE = Pr, Nd, Sm, Eu and Gd. On the other hand the crystallinity is excellent when the cerium concentration is equal to or above $x = 0.06$. This implies, that substitution of the large La by the smaller cerium (see Table 3.1) shifts the tolerance factor away from the copper-six-fold-coordinated threshold line (see Fig. 3.18). At the same time, cerium is in the tetravalent state and therefore simultaneously acts as a dopant. In order to avoid doping and protecting high crystalline T′-phase, another element should be chosen. As a starting point Terbium was chosen as a proper candi-

date. Since the valency of Tb can be both, Tb^{3+} and Tb^{4+}, there is still the possibility, that Terbium may act in a similar way like Cerium. So, the goal is clear: Stabilization of high quality T′-structured $La_{2-y}RE_yCuO_4$. In the following, character x refers to the doping and y represents the substitution. Thin films of $La_{2-y}Tb_yCuO_4$ have been grown by using the reactive MBE as described in Chapter 3. Again, (001)$SrTiO_3$ substrates were used for carrying out these experiments. To start with, the growth conditions of $La_{1.91}Ce_{0.09}CuO_4$ were used. The flux rate of the e-guns were adjusted in order to achieve a thin film with approximate composition of $La_{1.67}Tb_{0.33}CuO_4$. Generally speaking, the whole growth process was kept with identical values as for $La_{1.91}Ce_{0.09}CuO_4$, including the annealing procedure. The RHEED pattern observed during the deposition indicated that the T′-phase is stabilized (see Fig. 6.1). Fig. 6.2 shows the x-ray diffraction pattern of a

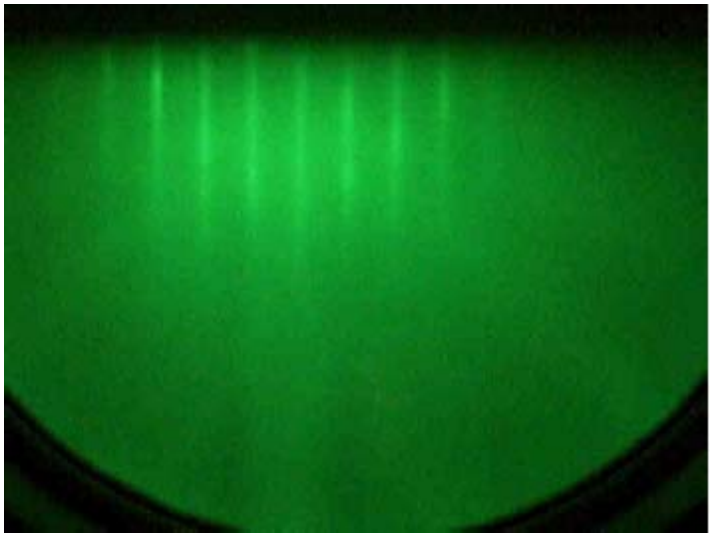

Fig. 6.1: RHEED pattern along (100) azimuth of $La_{2-y}Tb_yCuO_4$ thin film with $y \approx 0.33$ grown on (001)$SrTiO_3$.

$La_{1.67}Tb_{0.33}CuO_4$ thin film grown on a (001)$SrTiO_3$ substrate. The films were single phase with respect to the detection limit. According to the c-axis length of $c = 12.39\,\text{Å}$ one can clearly see, that $La_{1.66}Tb_{0.33}CuO_4$ is stabilized in the T′-structure. Since the FWHM value of the rocking curve of (006)-peak is approx. $0.07\,^\circ$, the crystallinity is comparable to thin films of $Pr_{2-x}Ce_xCuO_4$. For comparison, c-axis length of cerium doped and terbium substituted samples are plotted in Fig. 6.3. It is known (see Table 3.1), that

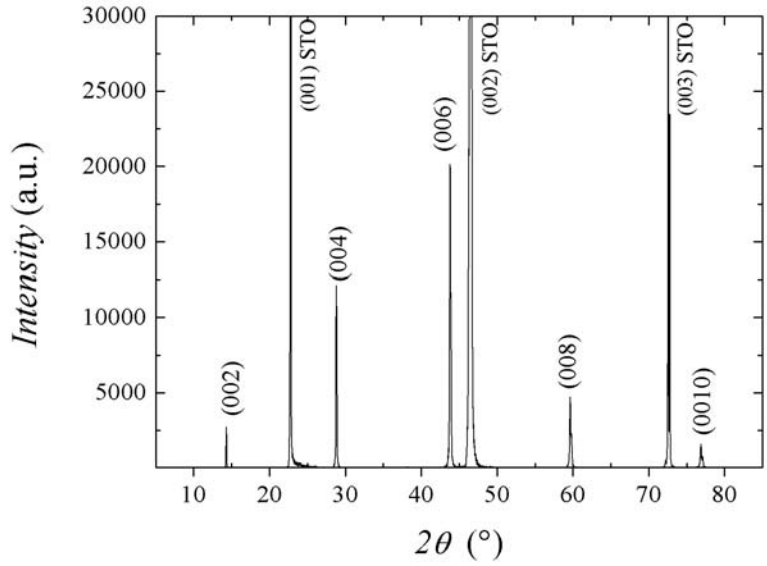

Fig. 6.2: X-Ray diffraction pattern of $La_{2-y}Tb_yCuO_4$ thin film with $y \approx 0.33$ grown on (001)$SrTiO_3$.

the ionic radius of tetravalent terbium is 0.88 Å and therefore much smaller compared to tetravalent cerium (0.97 Å). Let us assume, that terbium stays in the 4+ state and substitutes trivalent La with $r_{ion} = 1.16$ Å. Using oversimplified geometrical arguments, the slope should be $\frac{1.16}{0.88}$ and therefore steeper than for the cerium case $\frac{1.16}{0.97}$. Obviously, it is not the case as the slope for the cerium doped samples is steeper. These indications have been confirmed by *in situ* XPS measurements. For comparison Tb_2O_3 and Tb_4O_7 are also shown in Fig. 6.4. The spectra of the $La_{1.7}Tb_{0.3}CuO_4$ thin film shows similar behavior as Tb_2O_3 where the absence of the peak around 157 eV clearly demonstrates the trivalent state of terbium. Figure 6.5 shows the resistivity behavior of $La_{1.7}Tb_{0.3}CuO_4$ thin films grown on (001)$SrTiO_3$. First, $La_{1.7}Tb_{0.3}CuO_4$ clearly shows metallic behavior like the cerium analogues. The absolute resistivity value is in the same range as for e.g., $Sm_{2-x}Ce_xCuO_4$ thin films. *But the most striking point is that* $La_{1.66}Tb_{0.33}CuO_4$ *shows superconductivity with* $T_c \approx 17\,K$. The appearance of superconductivity has been proofed by a magnetization measurement using a Quantum Design SQUID

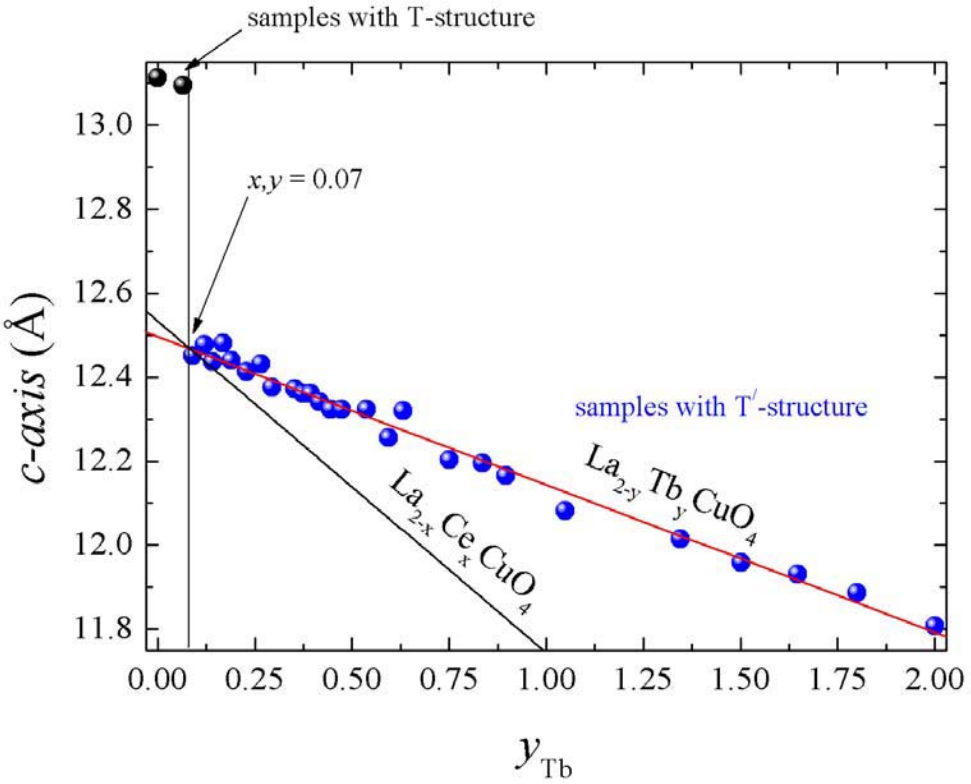

Fig. 6.3: c-axis lengths of $La_{2-y}Tb_yCuO_4$ and $La_{2-x}Ce_xCuO_4$ thin films grown on (001)$SrTiO_3$ substrates. The critical point, where the crystal structure changes between the T-phase and the T′-phase is found to be $x, y = 0.07$ irrespective of cerium doping or terbium substitution. For $La_{2-y}Tb_yCuO_4$ thin films, no solubility limit is found. For $y = 2$ pure Tb_2CuO_4 thin films have been synthesized.

MPMS (Fig. 6.5). The applied external magnetic field of $B = 50\,\mathrm{Oe}$ is parallel to the thin film surface generating a clean Meissner-Ochsenfeld signal. The appearance of superconductivity in a nominally undoped cuprate stimulated further experiments. Thin films of $La_{2-y}RE_yCuO_4$, with RE = Lu, Tb, Y, Eu and Sm have been grown with various RE concentrations. However, within a certain range of y, superconductivity was found for all, and the phase diagram is plotted in Fig. 6.6. There, the superconducting transition temperature T_c is plotted as a function of the amount y of substituted triva-

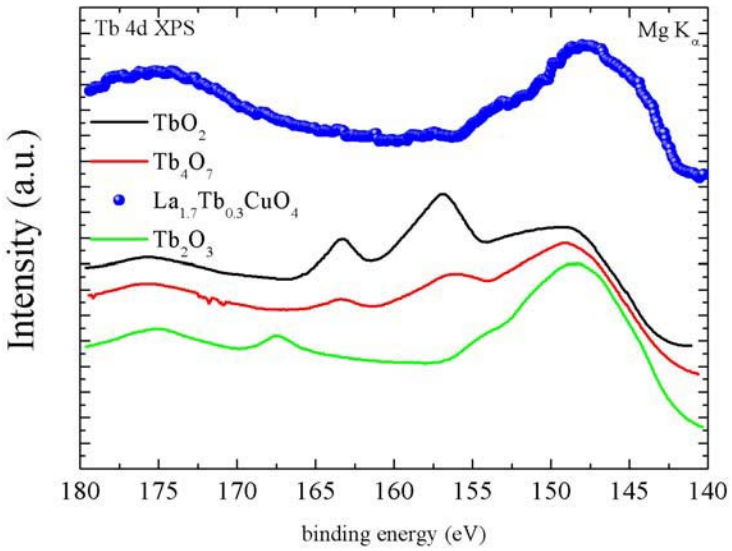

Fig. 6.4: *In-situ* Tb-4d XPS spectrum of $La_{1.7}Tb_{0.3}CuO_4$ thin film. The XPS spectra for TbO_2, Tb_4O_7 and Tb_2O_3 are given for comparison.

lent rare earth elements which is in contrast to conventional phase diagrams, where the x-axis corresponds to the doping level. *However, in the present case, there is no doping - at least not nominally.* Taking into account the data from Fig. 3.19, where low synthesize temperatures favor the formation of the T′-structure, and also the fact, that the crystallinity is comparable to conventional electron-doped cuprate thin films, one can conclude, that the substitution of the large La^{3+}-ion by smaller RE^{3+}-ions result in high crystallinity. As it is known from Fig. 2.16, T′-structured Sm_2CuO_4 is an antiferromagnet with $T_N \approx 250\,\mathrm{K}$ (although the annealing treatment for this sample remains unknown). Sm_2CuO_4 is the end member of $La_{2-y}Sm_yCuO_4$ with $y = 2$. At least, one can conclude, that Sm_2CuO_4 does not show metallic behavior. From Fig. 6.6 one can see, that superconductivity sets in for $y < 0.75$. With decreasing y, the superconducting transition temperature continuously increases, until a critical value y_{crit} is reached. This critical value separates the T′- from the T-phase and depends on the rare earth ionic radii. The reason for the superconductivity seems to be that the large

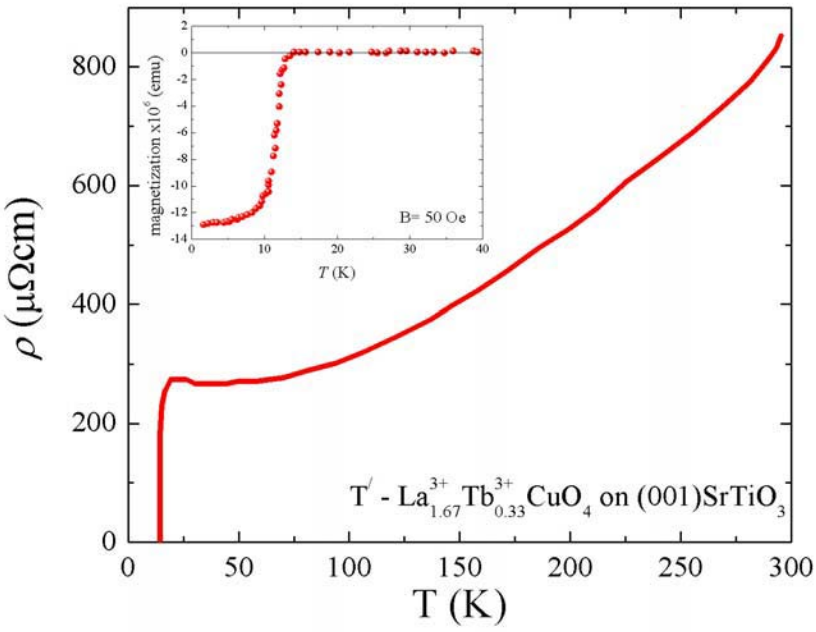

Fig. 6.5: Resistivity vs. temperature of $La_{1.7}Tb_{0.3}CuO_4$ thin film grown on (001)$SrTiO_3$. The film-thickness was 2000 Å. The inset shows magnetization vs. temperature, where the external magnetic field (50 Oe) is applied parallel to the surface of the thin film. The superconducting volume fraction is 94%.

in-plane lattice constant a_0 of T′-$La^{3+}_{2-x}RE^{3+}_xCuO_4$ enables more thorough removal of impurity oxygen at the apical site with the aid of large surface-to-volume ratio of thin films. This result contradicts the paradigm of high-T_c superconductors, stating that, the undoped copper-oxygen plane is considered as an antiferromagnetically ordered Mott-insulator. Although there is no ostensible doping, since the substitution ion is apparently also trivalent (e.g., Y), discussions on the doping possibilities of oxygen off-stoichiometries obnubilate the physical consequences of this result. As it is well known, oxygen content determinations are tricky and sometimes experiments lead to no conclusive value. However, if the amount of sample material reaches the weight-range of grams, neutron-scattering is the method of choice for the determination of the oxygen content, since this method allows a site-specific analysis. However, for thin film the present situation does not allow a precise

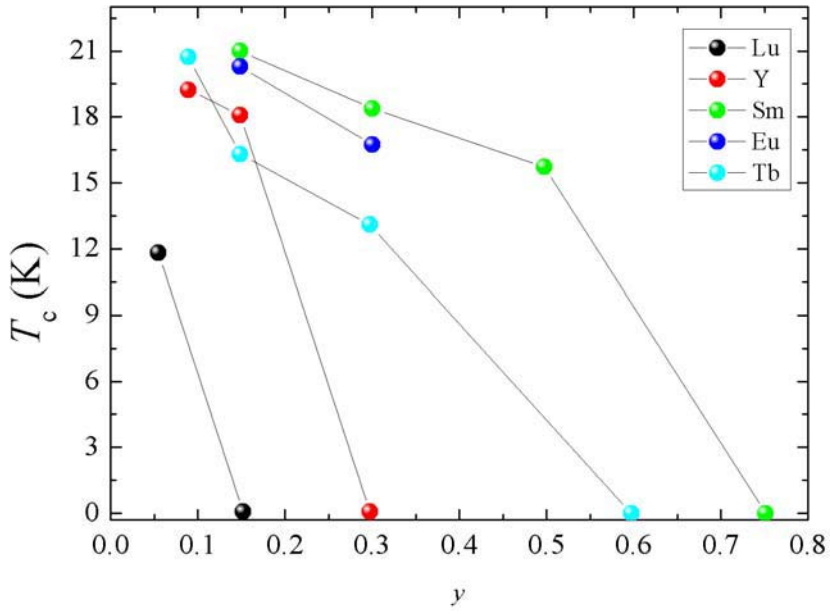

Fig. 6.6: Superconducting transition temperature vs. trivalent rare earth concentration y for $La_{2-y}RE_yCuO_4$ thin film grown on (001)$SrTiO_3$.

oxygen-content determination.

The larger a_0 of T′-$La_{2-y}RE_yCuO_4$ than that of other T′-RE_2CuO_4 enables more thorough removal of „impurity oxygen„ at the apical site, which leads to the superconductivity. *Our results suggest that the end member compounds of* T′-RE_2CuO_4 *are not Mott insulators.* However, this statement has to be verified. So far, neutron scattering experiments focused on either the occupation of interstitial oxygen in the T′ structure or to determine the antiferromagnetic Néel temperature of copper. Investigations on the relation between both, the apical oxygen occupation and the antiferromagnetic ordering, would drastically enhance the understanding of the underlying physics. In order to establish the above mentioned issues, neutron scattering experiments on bulk material of nominally undoped T′-structured cuprate superconductors are indispensable. The results of such experiments may have far

reaching implications on the mechanisms of high-T_c cuprates[1].

[1] Massidda *et al.* [320] mentioned, that the underlying physics of electron doped cuprates superconductors seems to be not in agreement with the Mott-Hubbard insulator.